UNIVERSITY OF OKLAHOMA

GRADUATE COLLEGE

GEOCHEMISTRY OF THE MISSISSIPPIAN VOLCANICLASTICS IN THE STANLEY GROUP, OUACHITA MOUNTAINS, OKLAHOMA AND ARKANSAS: IMPLICATIONS FOR TECTONIC ENVIRONMENT

A THESIS

SUBMITTED TO THE GRADUATE FACULTY

in partial fulfillment of the requirements for the degree of

MASTER OF SCIENCE

By

JENNIFER LEE LOOMIS

Norman, Oklahoma

1992

GEOCHEMISTRY OF THE MISSISSIPPIAN VOLCANICLASTICS IN THE STANLEY GROUP, OUACHITA MOUNTAINS, OKLAHOMA AND ARKANSAS: IMPLICATIONS FOR TECTONIC ENVIRONMENT

A THESIS

APPROVED FOR THE SCHOOL OF GEOLOGY AND GEOPHYSICS

BY

[redacted]

ACKNOWLEDGEMENTS

I would like to express my extreme gratitude to Harvey Blatt for his overall guidance and for my initiation into the adventures of sedimentary geochemistry/petrology! I also want to thank Barry Weaver for his assistance and insights into various aspects of my Masters research. Thanks also goes to Robert Fay, who was always keeping me on my toes by pointing out the many enigmas associated with the formation of the Ouachita Mountains, Doug Elmore for his input while serving on my committee, Neil Suneson for assistance in locating tuff exposures, Charlie Mankin for use of an Oklahoma Geological Survey field vehicle, and Richard Nicholas (Shell Oil Company) for giving me access to the Temple and Jones cores. I would also like to express my appreciation to AAPG for their grant-in-aid.

Special thanks also goes to Matt Totten (PhD ABD) for being there for me to bounce ideas off of and for helping me during the final crunch of completing my thesis!

ABSTRACT

A total of 46 tuff samples from the Mississippian Stanley Group in outcrop and 8 rhyolite samples collected from cores near the Sabine Uplift in Sabine County, Texas, have been analyzed for major element, trace element and rare earth element abundances. The effects of differential settling of crystals during deposition, diagenesis and weathering on tuff geochemistry have been characterized. Despite post-eruptive alteration and modification of the Stanley tuffs, enough of the igneous geochemical signature remains so that tuff geochemistry can be used to determine what type of tectonic setting was present along the Paleozoic southern North American plate margin.

A study of young rhyolites and tuffs from known, present-day tectonic settings provides the framework by which to determine which geochemical characteristics can be used as tectonic discriminants. The presence of a Ta-Nb trough (and whether or not it is persistent throughout the samples of a volcanic suite), the variability and extent of Ba and Sr depletion, and the extent of mobile-element enrichment relative to mid-ocean ridge basalts are the geochemical features which can be collectively used to determine the tectonic setting of high-silica volcanics.

Use of these geochemical features suggests that the Stanley tuffs and the Sabine rhyolite are associated with a continental island-arc system. In addition, plotting the tuffs and rhyolite samples on the granite tectonic discrimination diagrams developed by Pearce et al. (1984) implies that the Ouachita volcanics may have a back-arc basin component.

TABLE OF CONTENTS

LIST OF ILLUSTRATIONS

LIST OF TABLES

GEOCHEMISTRY OF THE MISSISSIPPIAN VOLCANICLASTICS IN THE STANLEY GROUP, OUACHITA MOUNTAINS, OKLAHOMA AND ARKANSAS: IMPLICATIONS FOR TECTONIC ENVIRONMENT

INTRODUCTION

The Ouachita Mountains are one of two exposed sections of a late Paleozic uplifted compressional zone located along the southern boundary of the North American craton (Figure 1). Since 1897 (Branner, 1897), geologists have been aware of the structural continuity between the Marathon uplift, the Ouachitas and the Appalachians. Before the theory of plate tectonics was developed, it was believed that a now-absent landmass (called Llanoria) collided with the southern North American margin, thrusting the geosynclinal basin sediments of the Ouachitas and Marathon area up and over the inner continental craton (Willis, 1907; Schuchert, 1910; Ulrich, 1911; Dumble, 1920; Powers, 1920; Miser, 1921; Morgan, 1952). With the later development and application of plate tectonic theory, the rather simple idea of a landmass colliding with the southern North American plate has taken on added

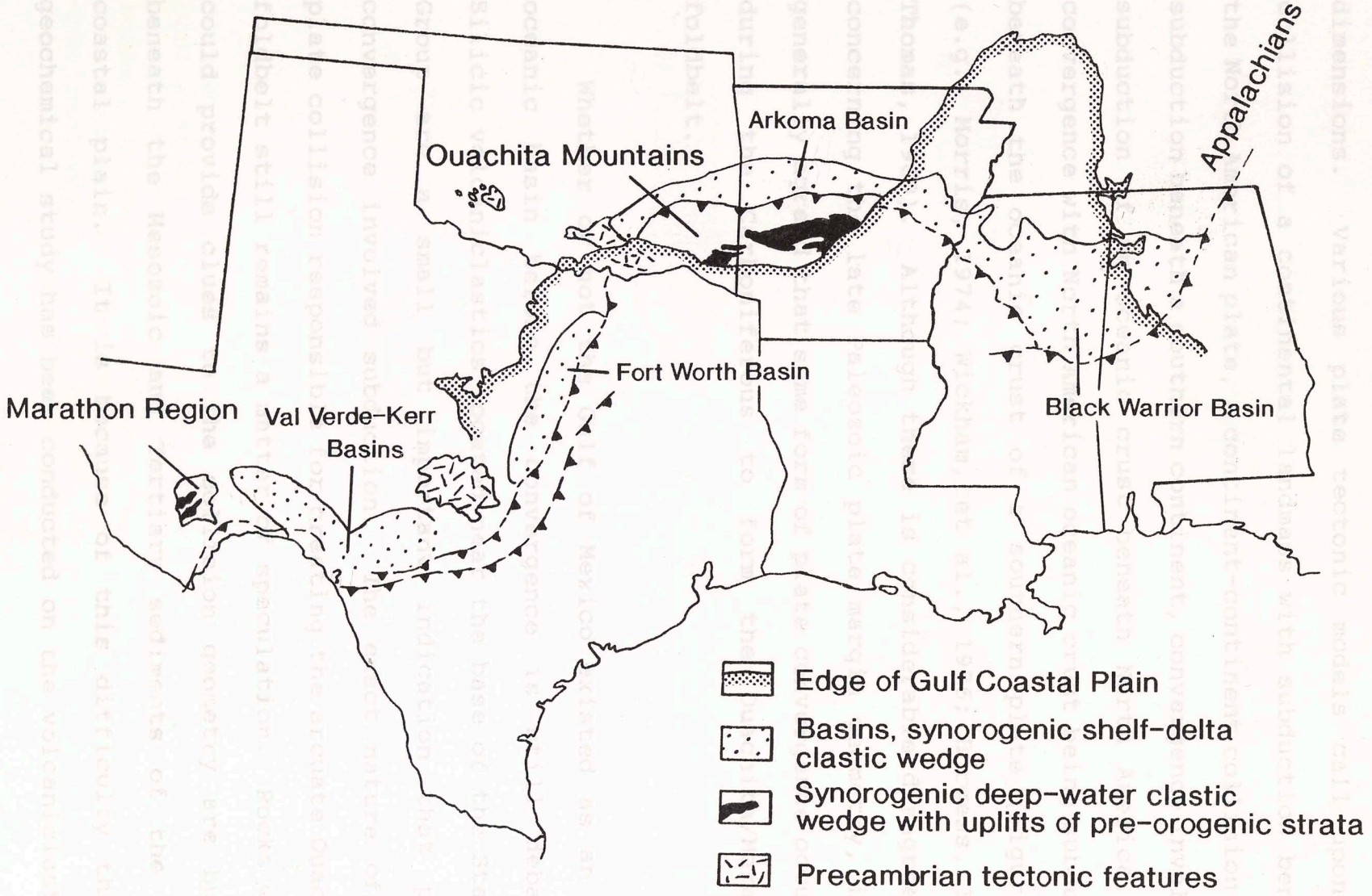

Figure 1. The Ouachita foldbelt (modified from Viele & Thomas, 1989).

dimensions. Various plate tectonic models call upon the collision of a continental landmass with subduction beneath the North American plate, a continent-continent collision with subduction beneath a southern continent, convergence involving subduction of an oceanic crust beneath North America, and convergence with North American oceanic crust being subducted beneath the oceanic crust of a southern plate (Figure 2) (e.g., Morris, 1974; Wickham, et al., 1976; Burgess, 1976; Thomas, 1989). Although there is considerable disagreement concerning the late Paleozoic plate margin geometry, it is generally agreed that some form of plate convergence occurred during the Carboniferous to form the Ouachita/Marathon foldbelt.

Whether or not the Gulf of Mexico existed as an open oceanic basin before the convergence is still debated. Silicic volcaniclastics located near the base of the Stanley Group are a small but important indication that plate convergence involved subduction. The exact nature of the plate collision responsible for creating the arcuate Ouachita foldbelt still remains a matter of speculation. Rocks which could provide clues to the collision geometry are buried beneath the Mesozoic and Tertiary sediments of the Gulf coastal plain. It is because of this difficulty that a geochemical study has been conducted on the volcaniclastics

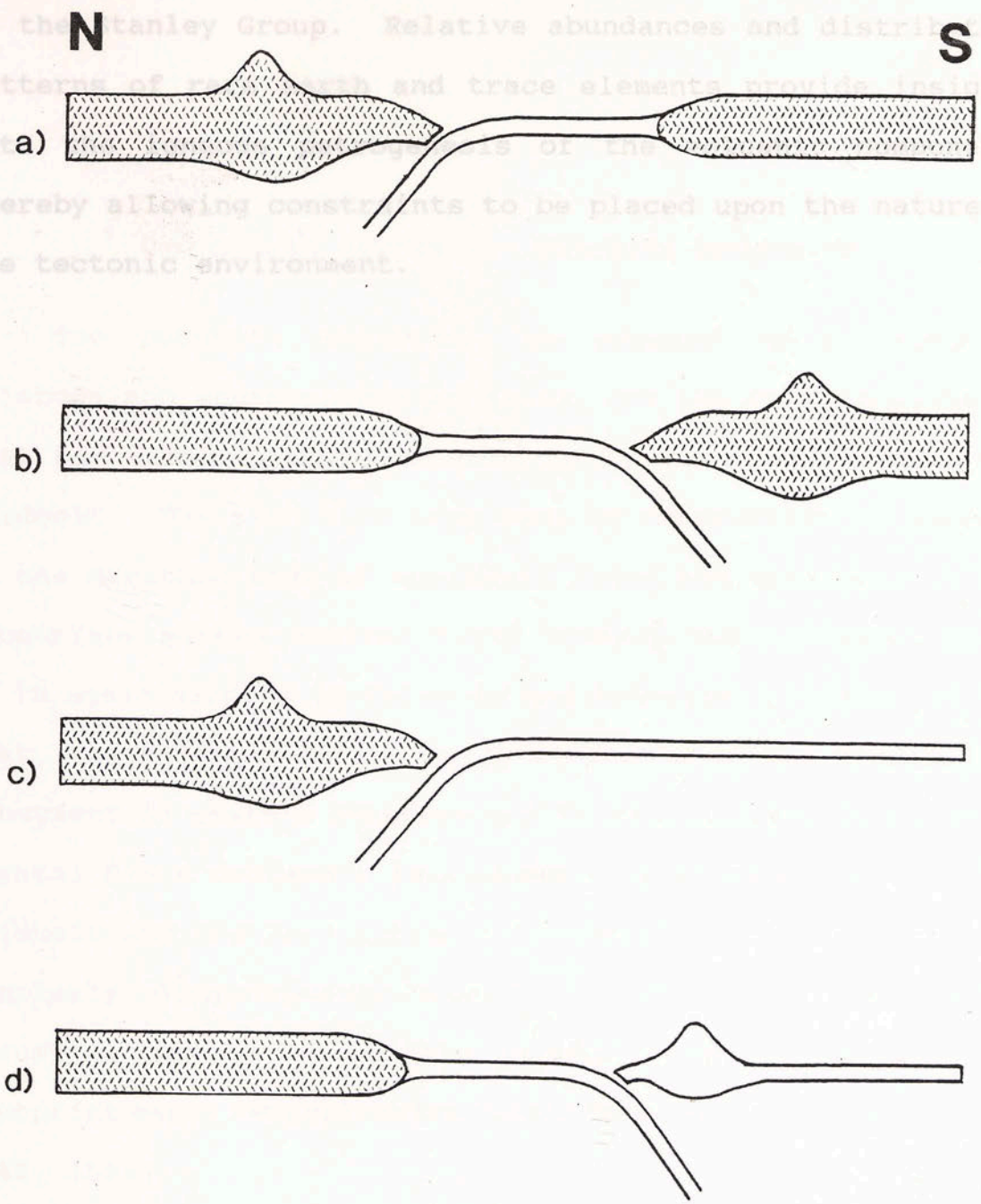

Figure 2. Possible subduction geometries: a) continent-continent collision with subduction beneath the North American plate, b) continent-continent collision with subduction beneath a southern continent, c) continent-ocean collision with subduction beneath the North American plate, and d) continent-ocean collision with an oceanic island-arc on the overriding southern plate.

of the Stanley Group. Relative abundances and distribution patterns of rare earth and trace elements provide insights into the igneous petrogenesis of the volcanic component, thereby allowing constraints to be placed upon the nature of the tectonic environment.

GEOLOGICAL SETTING -- OUACHITA MOUNTAINS

The Ouachita Mountains, as exposed in southeastern Oklahoma and southwestern Arkansas, are the type locality of what has commonly been referred to as the Ouachita/Marathon foldbelt. The 1300 mile long zone of compression is exposed in the Marathon area of southwest Texas and continues in the subsurface across central Texas towards the northeast where it is again exposed in Oklahoma and Arkansas. Farther to the east, the foldbelt is buried by sediments in the Mississippi embayment in eastern Arkansas and Mississippi and by Atlantic Coastal Plain sediments in Alabama. In Alabama the Ouachita foldbelt and the Appalachian fold-thrust belt intersect in a complexly discontinuous manner (Figure 3). Appalachian thrusting during the middle Pennsylvanian is believed to overprint early Pennsylvanian Ouachita-type thrusting (Thomas, 1985, 1989).

Stratigraphy

The "Ouachita facies" is the suite of rocks which comprise the Ouachita/Marathon foldbelt. The stratigraphic character and degree of metamorphism of these rocks is

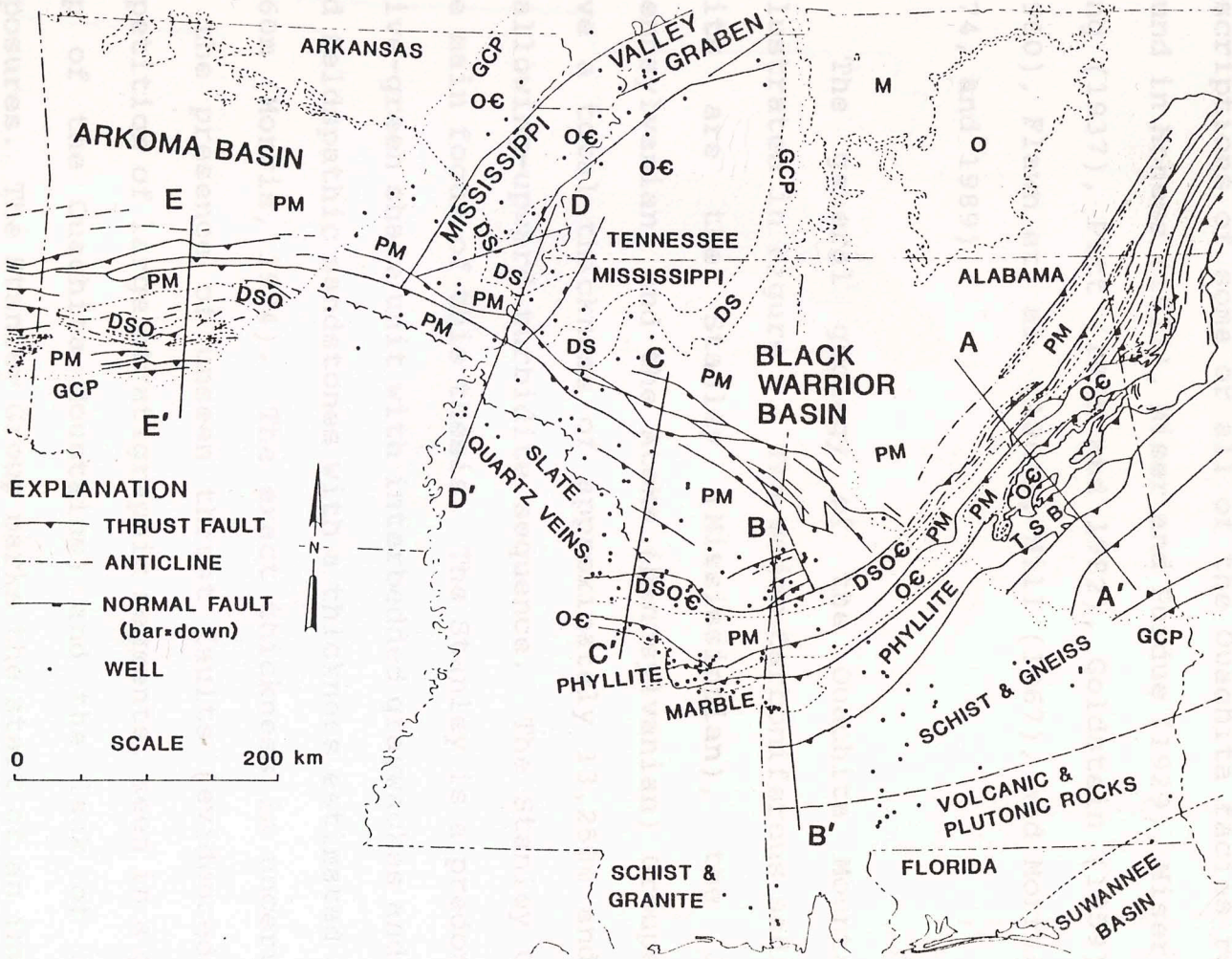

Figure 3. The Appalachian-Ouachita connection beneath the Gulf Coastal Plain (from Thomas, 1985).

variable; yet the overall lithology remains fairly consistent (see Figure 4). Detailed stratigraphic and petrographic descriptions of some or all of the Ouachita facies rocks are found in Honess (1923), Miser and Purdue (1929), Miser (1934), King (1937), Pitt (1955 and 1982), Goldstein (1959), Cline (1960), Flawn et. al. (1961), Hill (1967), and Morris (1971, 1974, and 1989).

The general geology of the Ouachita Mountains is illustrated in Figure 5. The major Carboniferous sedimentary units are the Stanley (Mississippian), the Jackfork (Pennsylvanian) and the Atoka (Pennsylvanian) Groups, which have a total thickness of approximately 13,250m and form a shallowing-upward turbidite sequence. The Stanley Group is the main focus of this thesis. The Stanley is a predominantly olive-green shale unit with interbedded graywackes and silicic and feldspathic sandstones with a thickness estimated at 2440-3660m (Morris, 1974). The exact thickness is uncertain due to the presence of unseen thrust faults (evidenced by the repetition of large stratigraphic segments, seen in a geologic map of the Ouachita Mountains) and the lack of complete exposures. The Stanley Group marks the start of an inundation of clastic material upon a deep-marine radiolarian chert, the Devonian Arkansas Novaculite. Initial sedimentation rates have been estimated at 170m/Ma with increasing rates of

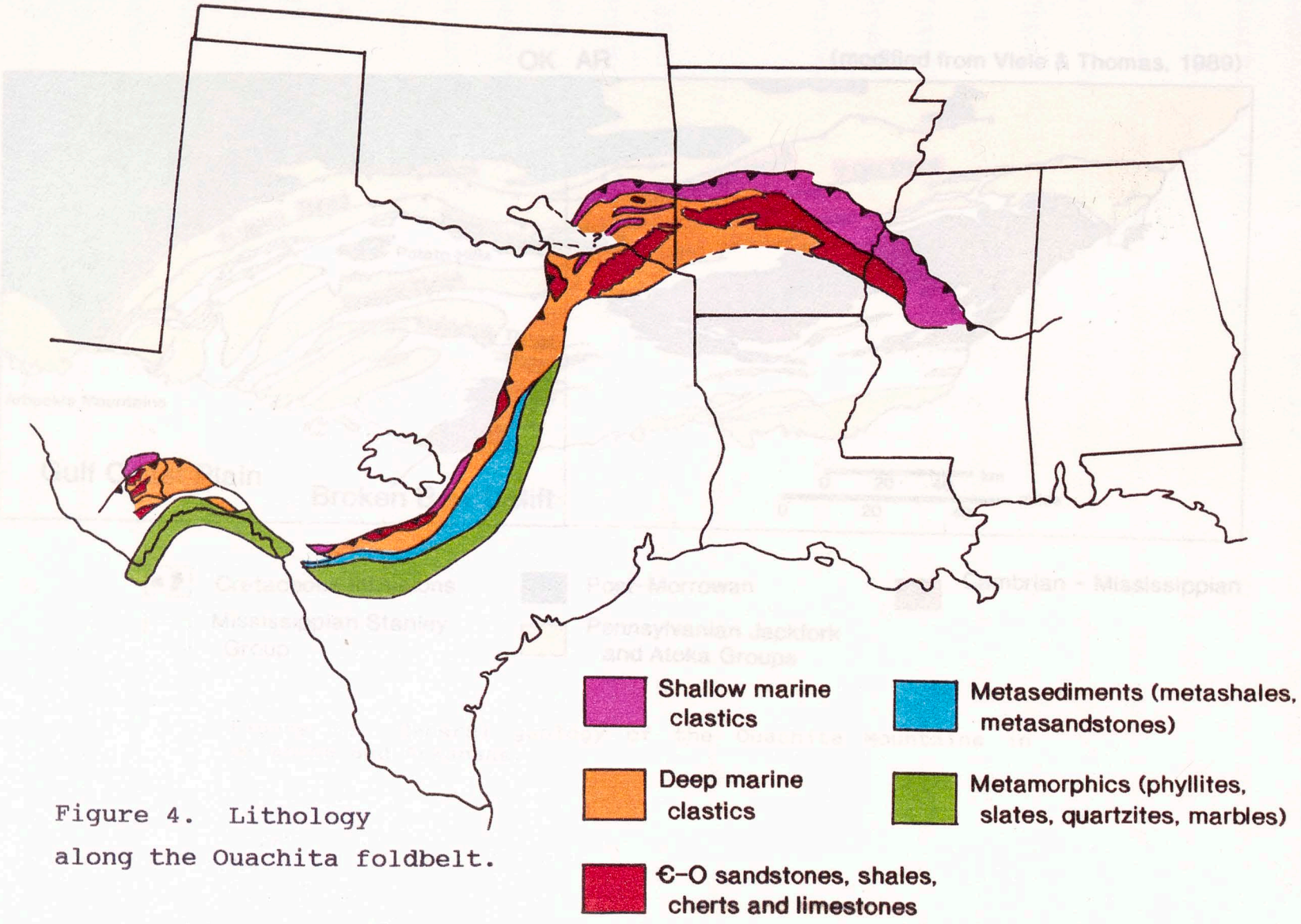

Figure 4. Lithology along the Ouachita foldbelt.

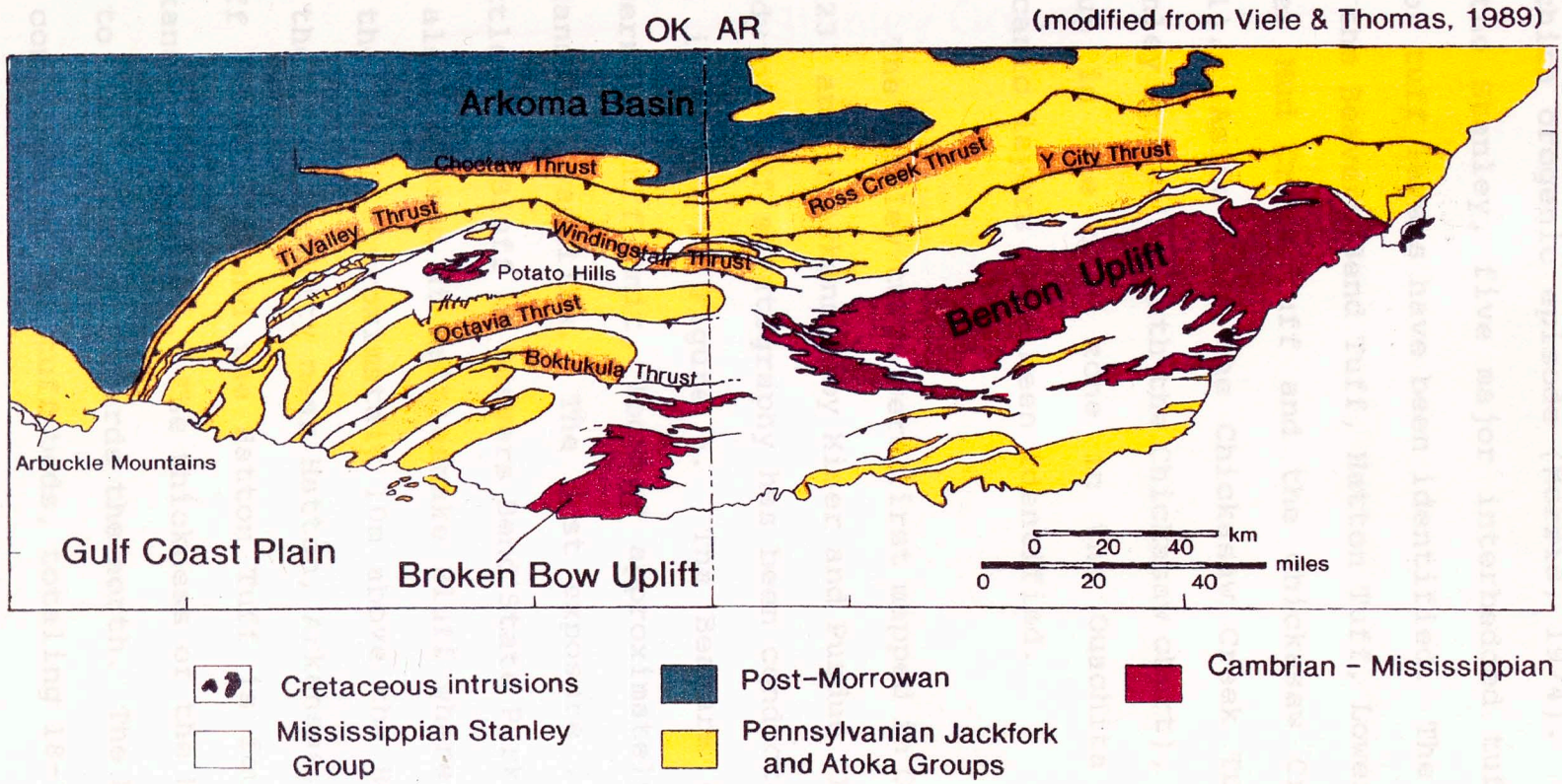

Figure 5. General geology of the Ouachita Mountains in Oklahoma and Arkansas.

deposition (up to 900m/Ma for the Atoka Formation) during the Ouachita orogenic episode (Morris, 1974). Towards the base of the Stanley, five major interbedded tuff units and two minor tuff layers have been identified. The major tuff units are the Beavers Bend Tuff, Hatton Tuff, Lower Mud Creek Tuff, Upper Mud Creek Tuff and the Chickasaw Creek Tuff (Niem, 1971). Aside from the Chickasaw Creek Tuff in the upper Stanley Group (beneath the Chickasaw chert), the lower Stanley Group is the only zone in the Ouachita Mountains where volcanic layers have been identified.

The Stanley tuffs were first mapped in Oklahoma by Honess (1923) and in Arkansas by Miser and Purdue (1929). A detailed study of tuff stratigraphy has been conducted by Niem (1971) and is shown in Figure 6. The Beavers Bend Tuff is the lowermost tuff unit, located approximately 285m above the Arkansas Novaculite. The best exposure is a 20m cliff on Rattlesnake Bluff at Beavers Bend State Park. The Hatton Tuff is also exposed at Rattlesnake Bluff where it occurs on top of the bluff approximately 10m above the Beavers Bend Tuff. At the type locality near Hatton, Arkansas, the Beavers Bend Tuff is absent and the Hatton Tuff is found 27m above the Arkansas Novaculite. The thickness of the Hatton ranges from 10 to 36m, thinning towards the north. The Mud Creek sequence is comprised of two tuff beds, totaling 18-36m in thickness,

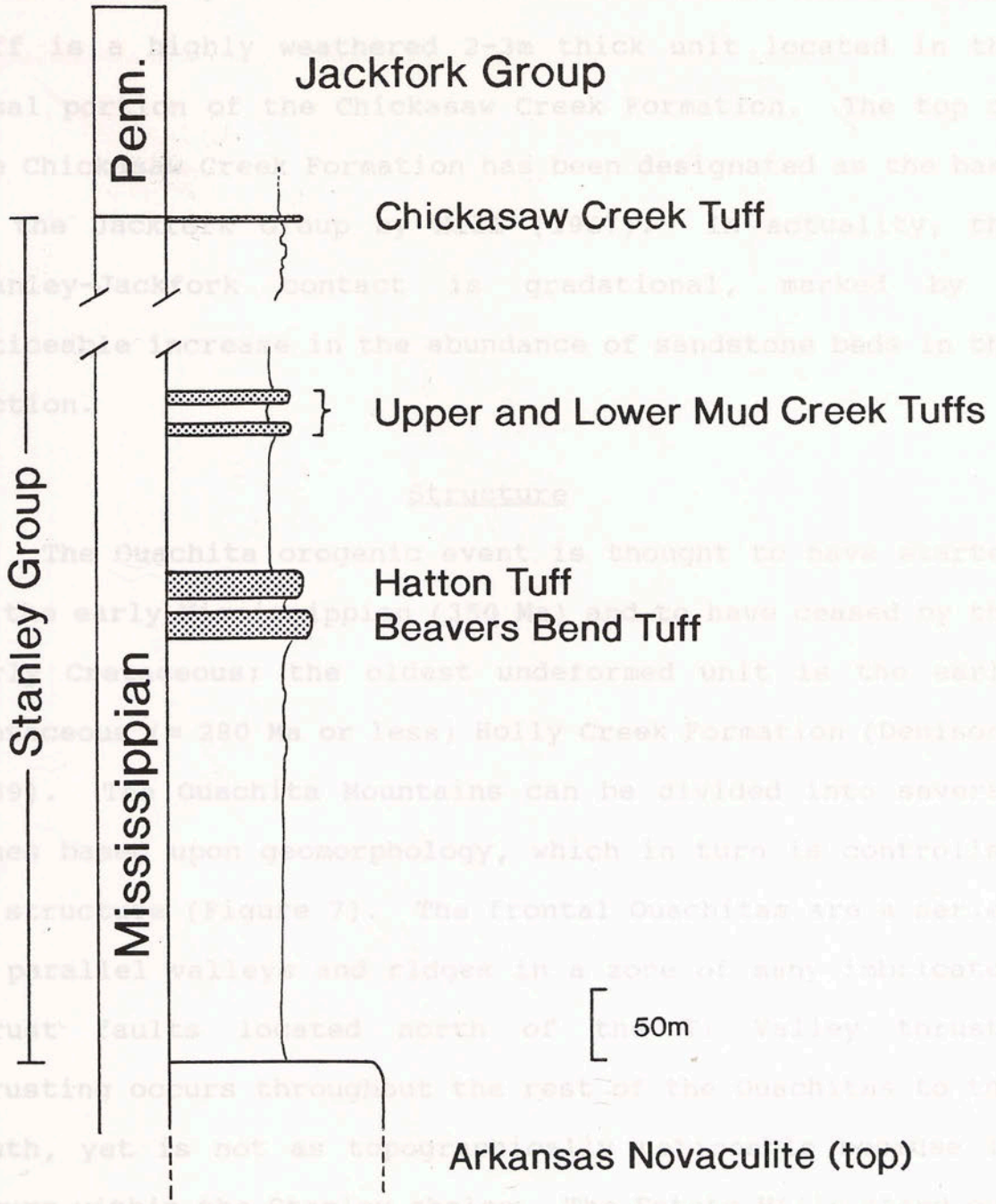

Figure 6. Stratigraphic positions of the major tuff units within the Stanley Group.

located roughly 90-120m above the Hatton Tuff. The Chickasaw tuff is a highly weathered 2-3m thick unit located in the basal portion of the Chickasaw Creek Formation. The top of the Chickasaw Creek Formation has been designated as the base of the Jackfork Group by Hill (1967). In actuality, the Stanley-Jackfork contact is gradational, marked by a noticeable increase in the abundance of sandstone beds in the section.

Structure

The Ouachita orogenic event is thought to have started in the early Mississippian (350 Ma) and to have ceased by the early Cretaceous; the oldest undeformed unit is the early Cretaceous (≈ 280 Ma or less) Holly Creek Formation (Denison, 1989). The Ouachita Mountains can be divided into several zones based upon geomorphology, which in turn is controlled by structure (Figure 7). The frontal Ouachitas are a series of parallel valleys and ridges in a zone of many imbricated thrust faults located north of the Ti Valley thrust. Thrusting occurs throughout the rest of the Ouachitas to the south, yet is not as topographically noticeable because it occurs within the Stanley shales. The Potato Hills stand out as a structural anomaly in the northern central Ouachitas. These hills are topographic highs of exposed Arkansas Novaculite and Ordovician clastics. A recent study indicates

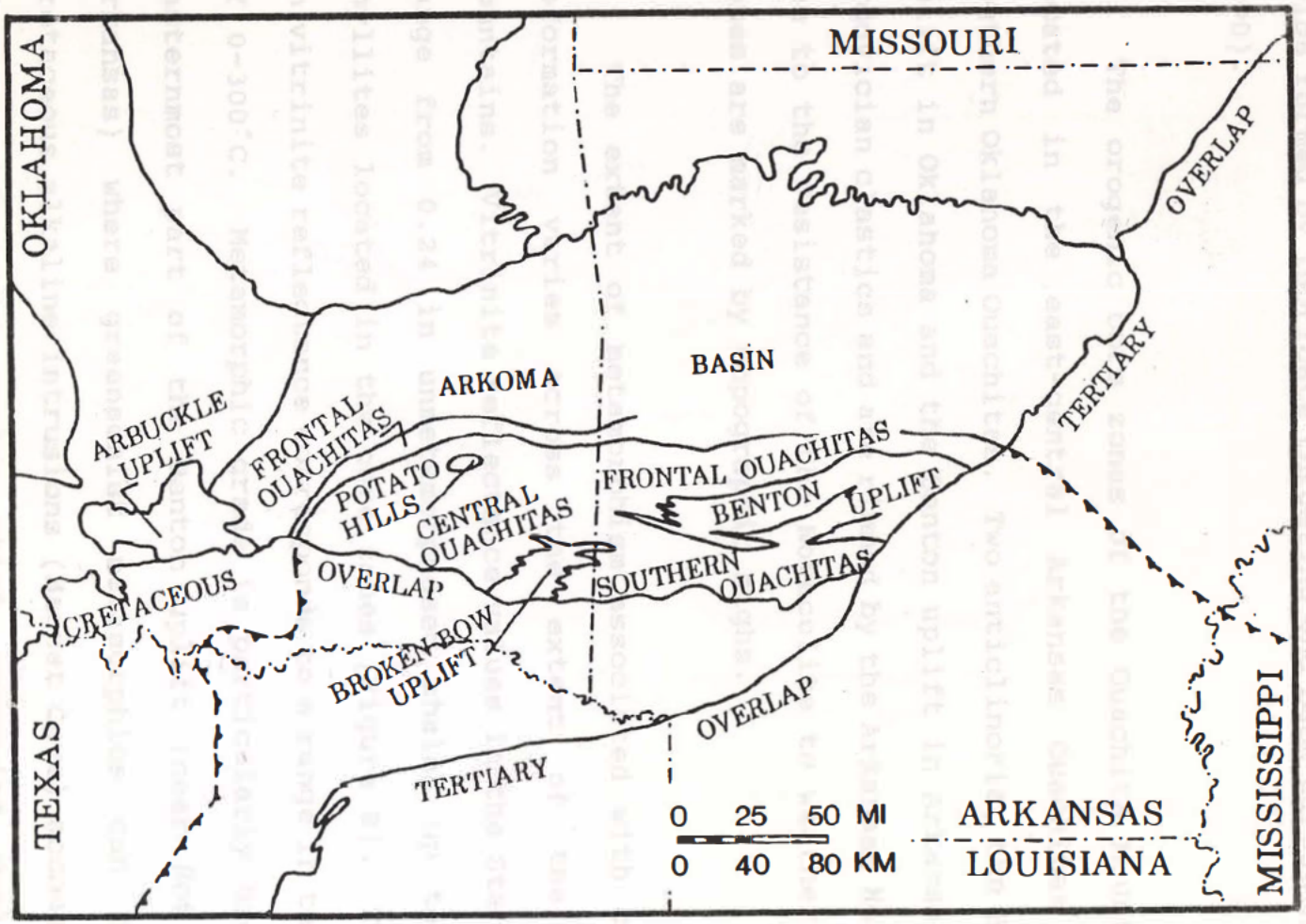

Figure 7. Tectonic provinces of the Ouachita Mountains (from Morris, 1974).

that the Potato Hills represent a collection of fault-drag folds formed by imbricate thrusting and back thrusting (Allen, 1990).

The orogenic core zones of the Ouachita Mountains are located in the east-central Arkansas Ouachitas and the southern Oklahoma Ouachitas. Two anticlinoria, the Broken Bow uplift in Oklahoma and the Benton uplift in Arkansas, expose Ordovician clastics and are rimmed by the Arkansas Novaculite. Due to the resistance of the Novaculite to weathering, both zones are marked by topographic highs.

The extent of metamorphism associated with convergent deformation varies across the extent of the Ouachita Mountains. Vitrinite reflectance values in the Stanley Group range from 0.24 in unmetamorphosed shales up to 4.28 in phyllites located in the core zones (Figure 8). This range in vitrinite reflectance corresponds to a range in temperature of 0-300°C. Metamorphic grade is particularly high in the easternmost part of the Benton uplift (near Hot Springs, Arkansas) where greenschist metamorphics can be found. Cretaceous alkaline intrusions (Magnet Cove) account for the higher metamorphic grades which overprint Carboniferous metamorphism.

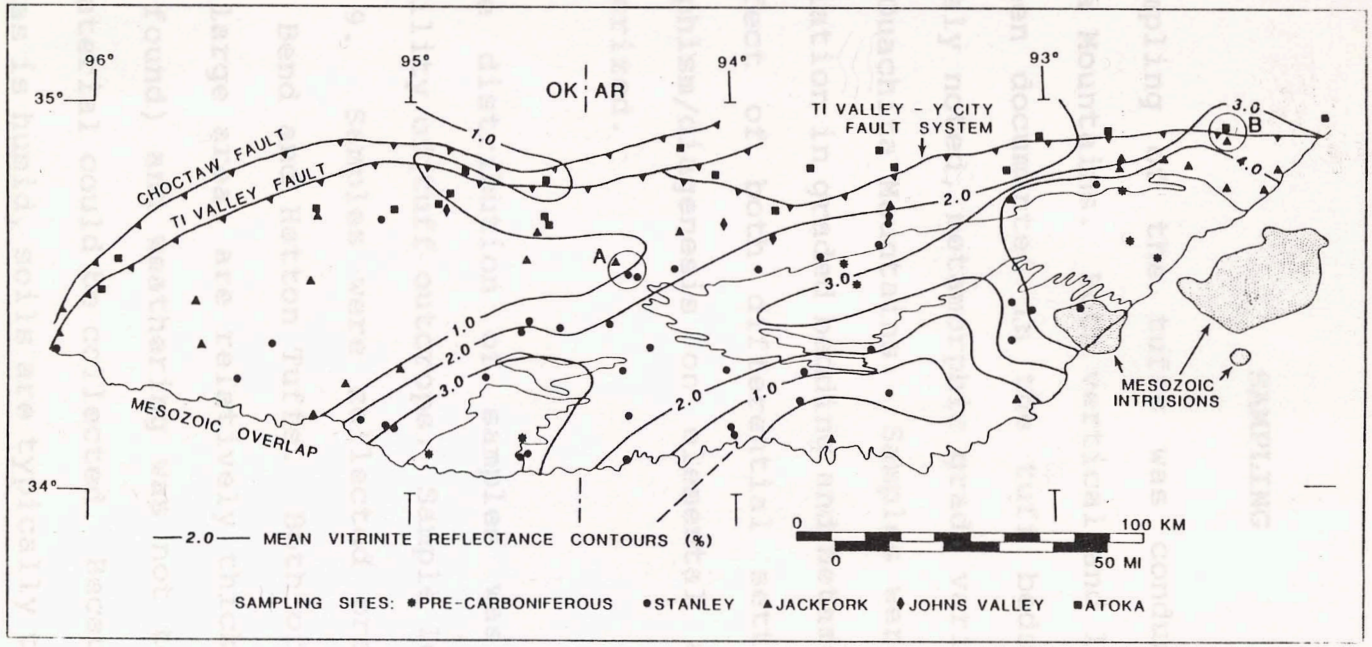

Figure 8. Map of vitrinite reflectance values across the Ouachita Mountains (from Houseknecht & Matthews, 1985).

SAMPLING

Sampling of the tuffs was conducted throughout the Ouachita Mountains. Both vertical and lateral grain sorting have been documented in the tuff beds (Niem, 1971). As previously noted, metamorphic grade varies across the extent of the Ouachita Mountains. Samples were collected to cover the variation in graded bedding and metamorphic grade, so that the effect of both differential settling of grains and metamorphism/diagenesis on elemental abundances could be characterized.

The distribution of samples was controlled by the availability of tuff outcrops. Sample locations are shown in Figure 9. Samples were collected predominantly from the Beavers Bend and Hatton Tuffs. Both of these tuffs persist over a large area, are relatively thick (and therefore more easily found) and weathering was not too extensive so that fresh material could be collected. Because the climate in the Ouachitas is humid, soils are typically thick, especially over the Stanley Group. Accordingly, there are very few naturally exposed tuff outcrops, even though the tuffs are more

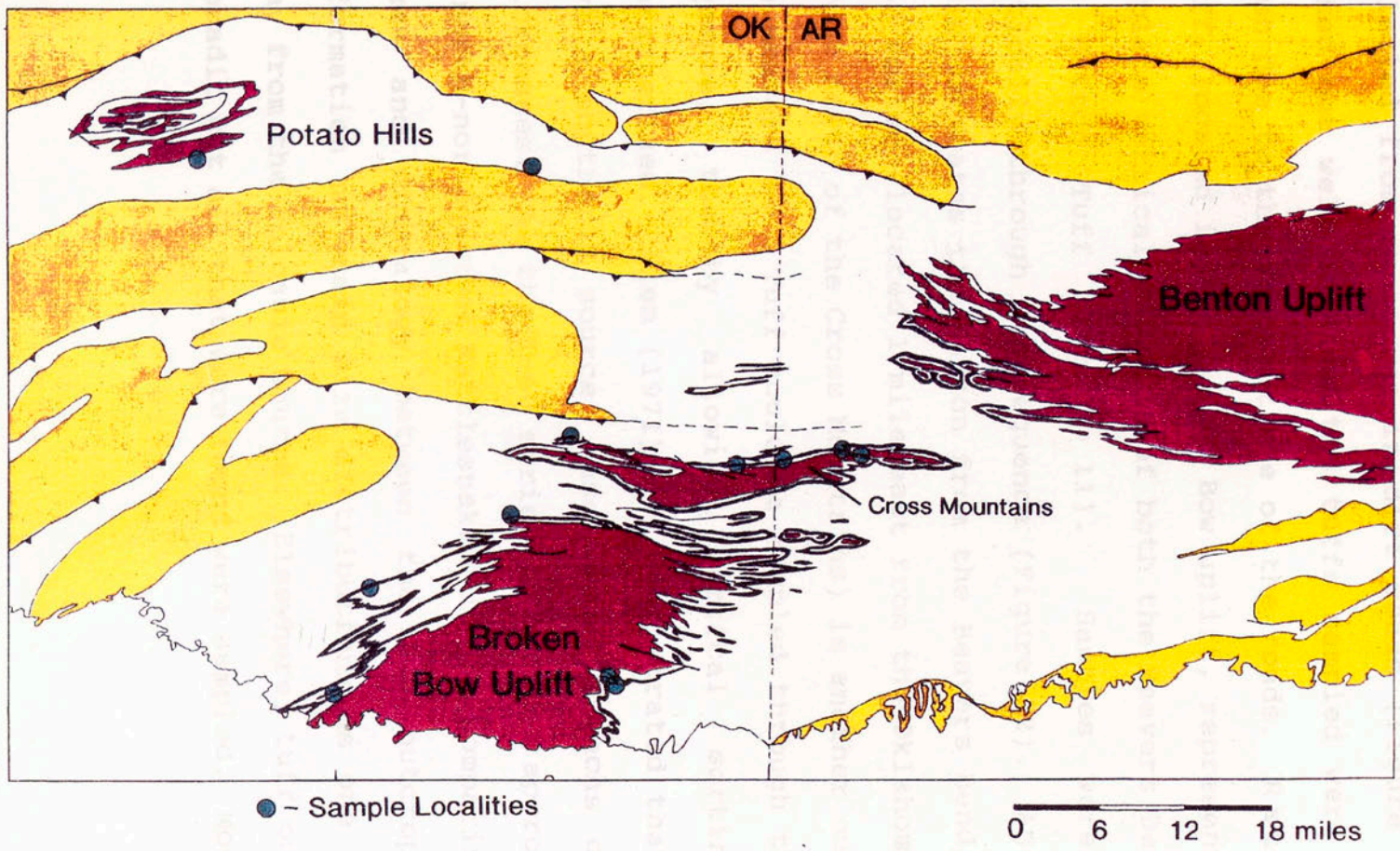

Figure 9. Tuff sample localities.

competent than the shales. Indeed, most of the samples were collected from exposures in dirt roads (Figure 10). This worked out well in that the tuffs sampled were relatively fresh due to the frequent use of the roads. Rattlesnake Bluff, located in the Broken Bow uplift, represents the most complete vertical exposure of both the Beavers Bend Tuff and the Hatton Tuff (Figure 11). Samples were collected vertically through the sequence (Figure 12). An outcrop of shale separates the Hatton from the Beavers Bend Tuff. The T-60 series (located 1 mile east from the Oklahoma/ Arkansas border north of the Cross Mountains) is another outcrop where the Beavers Bend Tuff could be sampled through the vertical sequence, thereby allowing vertical sorting to be characterized. Niem (1971) has demonstrated that the tuffs have a southerly source, based upon isopachs of tuff bed thicknesses. As the T-60 series is located approximately 32 km north-northeast of Rattlesnake Bluff, a comparison of grain sizes and mineralogy between the two outcrops provides information on grain size distributions as one moves north away from the volcanic source. Elsewhere, tuff outcrops were sporadic but all that were found were sampled. Most of these

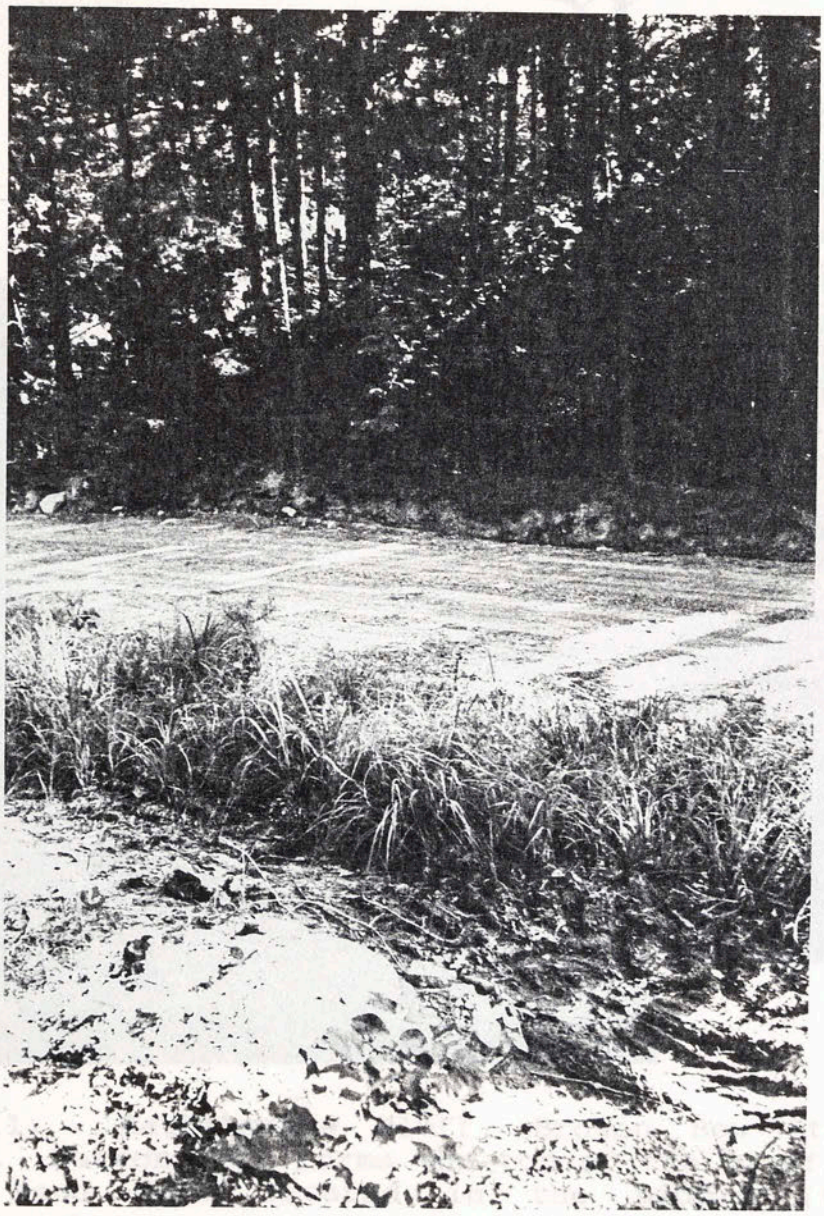

Figure 10. Photo of a typical sample site (this is the site of sample T-59).

Figure 11. Rattlesnake Bluff, Broken Bow State Park, Oklahoma. Hatton Tuff forms the top of the bluff, with the Beavers Bend Tuff located in the middle (the cliff exposure).outcrops are not extensive exposures. Moreover, deformation is known to be complex (and is only mapped on a large scale) so that it was difficult to identify a tuff based upon its stratigraphic position within the Stanley. They can be identified petrographically and, to a limited extent, geochemically.

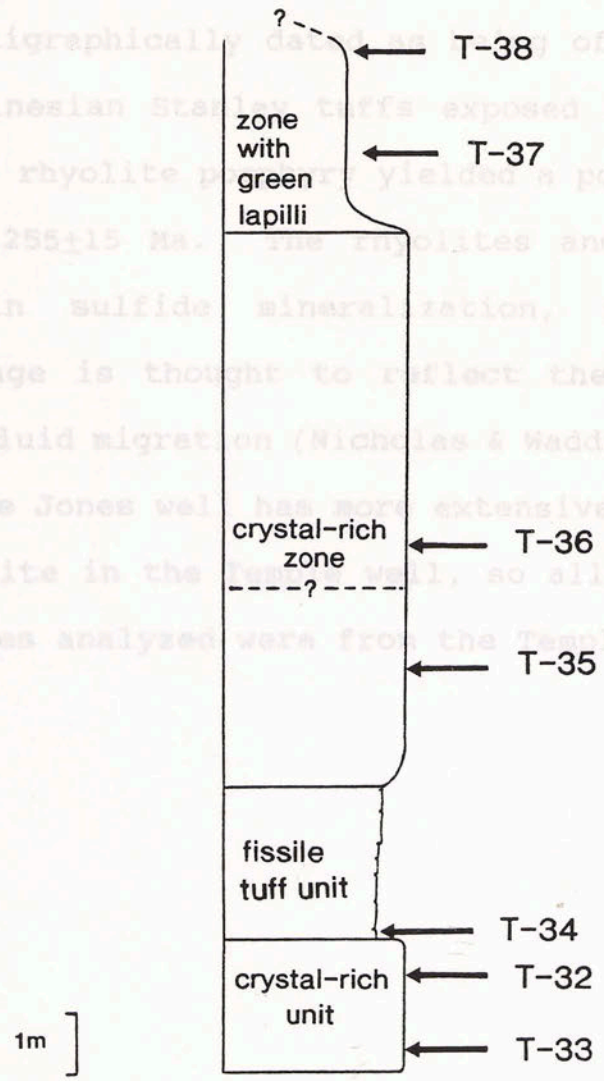

Figure 12. Stratigraphic section of the Beavers Bend section at Rattlesnake Bluff with sample sites.

Rhyolite samples were obtained from cores located in Sabine County, Texas (Figure 13). The Shell wells, Jones #1 and Temple #1 (well numbers 13 and 14 in Figure 13), penetrated a rhyolite porphyry lying uncomformably upon Carboniferous flysch at depths of 4270-4575m (Figure 14). Although stratigraphically dated as being of similar age to the pre-Desmoinesian Stanley tuffs exposed in the Ouachita Mountains, the rhyolite porphyry yielded a post-Desmoinesian Rb-Sr age of 255±15 Ma. The rhyolites and the overlying strata contain sulfide mineralization, and the post-Desmoinesian age is thought to reflect the date of post-depositional fluid migration (Nicholas & Waddell, 1989). The rhyolite in the Jones well has more extensive mineralization than the rhyolite in the Temple well, so all but 1 of the 6 rhyolite samples analyzed were from the Temple well.

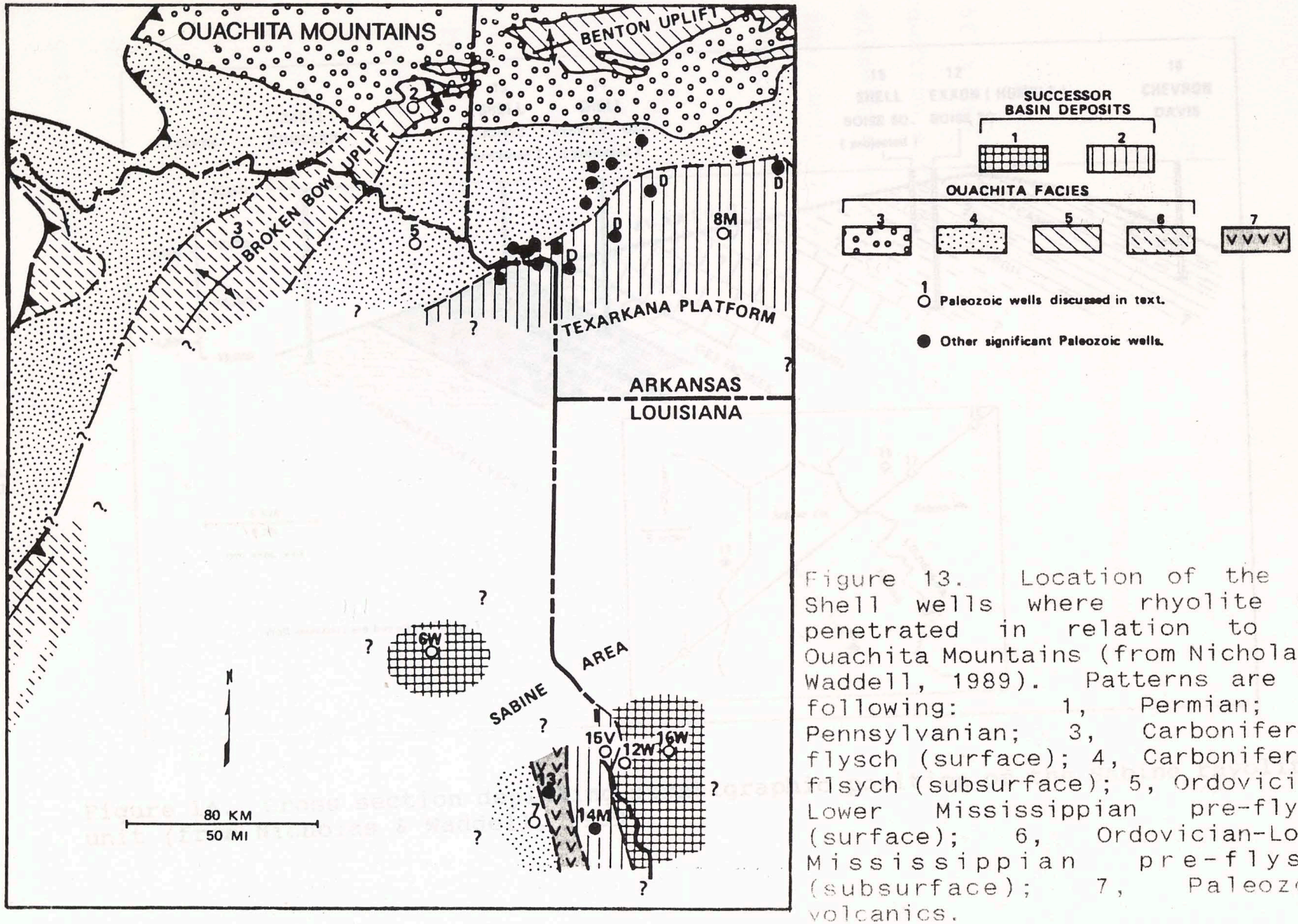

Figure 13. Location of the two Shell wells where rhyolite was penetrated in relation to the Ouachita Mountains (from Nicholas & Waddell, 1989). Patterns are the following: 1, Permian; 2, Pennsylvanian; 3, Carboniferous flysch (surface); 4, Carboniferous flsych (subsurface); 5, Ordovician-Lower Mississippian pre-flysch (surface); 6, Ordovician-Lower Mississippian pre-flysch (subsurface); 7, Paleozoic volcanics.

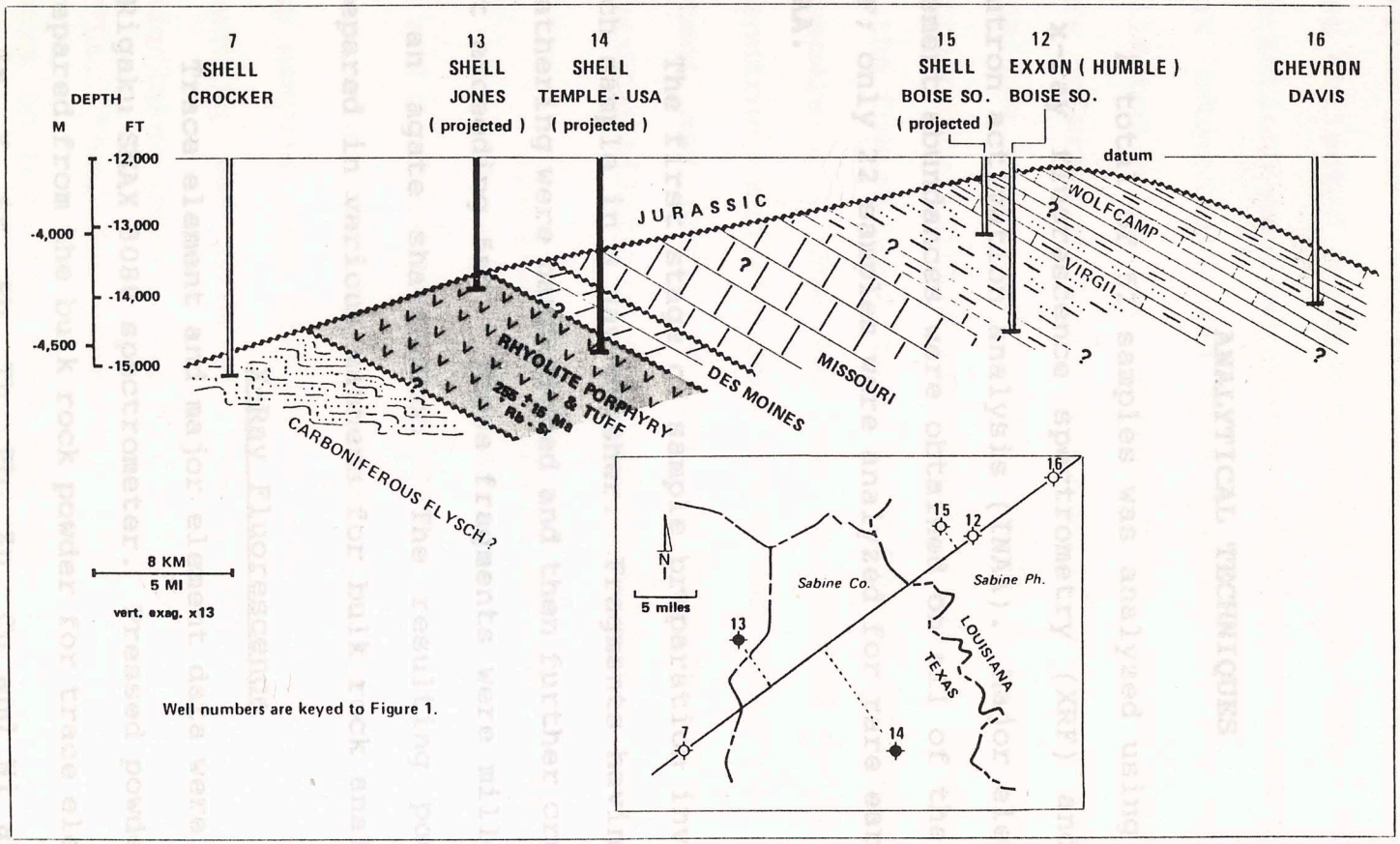

Figure 14. Cross section depicting stratigraphic position of the Sabine rhyolite unit (from Nicholas & Waddell, 1989).

ANALYTICAL TECHNIQUES

A total of 52 samples was analyzed using a combination of x-ray fluorescence spectrometry (XRF) and instrumental neutron activation analysis (INAA). Major element and trace element abundances were obtained on all of the samples using XRF; only 22 samples were analyzed for rare earth elements by INAA.

The first stage of sample preparation involved crushing each sample in a jaw-crusher. Fragments having little or no weathering were hand-picked and then further crushed to a size not exceeding 5mm. These fragments were milled to a powder in an agate shatterbox. The resulting powder was then prepared in various manners for bulk rock analysis.

X-Ray Fluorescence

Trace element and major element data were obtained using a Rigaku SMAX 3080 spectrometer. Pressed powder pellets were prepared from the bulk rock powder for trace element analysis. Nb, Zr, Y, Sr, Rb, Th, Pb, Zn, Cu and Ni abundances were gathered using a rhodium X-ray tube and mass adsorption

corrections were applied internally using the rhodium Kα Compton peak. Ce, Nd, V, Mn, Cr, La, Sc, and Ba abundances were collected using a tungsten X-ray tube. Mass adsorption corrections were calculated using major element and Rh compton peak intensities and then applied to the various elements collected using the tungsten tube. Major element abundances were determined from glass fusion beads, which were prepared from the bulk rock powder using a lanthanum-doped lithium tetraborate/lithium carbonate flux. A complete description of the fusion bead preparation technique employed is given in Appendix I. The XRF was calibrated using international standards, and standard NIM-G was run every other cycle to detect any drift in the calibration over time. Sample reproducibility is reported in Appendix II.

Instrumental Neutron Activation Analysis

La, Nd, Sm, Lu, Ce, Eu, Gd, Tb, Tm, Yb, Ta, Sc, Co, Cr, Hf and Cs abundances were obtained by INAA. Bulk rock powders were irradiated in a neutron flux for approximately 1 week, the samples were allowed to cool for approximately one week. Counting was done in two phases. The first phase was undertaken immediately to count isotopes with short half-lives (^{140}La, ^{153}Sm, for example). The samples were counted for 3 hours on both the LEPS and coaxial detectors. The coaxial detector is optimal for detecting high-energy gamma radiation (200KeV-2MeV), and LEPS detector (low-energy photon

spectrometers; detectors which have planar crystals) measures low-energy gamma radiation (50-200KeV). After the short counts, the samples were cooled for another two weeks to allow for sufficient decay to reduce background levels. Long counts were then conducted for a period of 12 hours on each detector.

For the initial irradiation, 18 unknown rock powders and 6 standards were sealed in polyvinyl vials. The 24 vials were in turn sealed into 3 polyvinyl tubes, with two standards NIM-G (granite) and JB-1a (basalt), positioned at either end of each tube. Variations in flux intensity along the length of each tube was then corrected for by comparing the measured La concentration with the known concentration of La in the JB-1a standard. Ce was used as a check against the La-derived flux factor. All of the elements were calibrated against NIM-G, with the exception of Sc, Co, Cr, Ta and Eu, which were calibrated against JB-1A.

PETROGRAPHY

Tuffs

Detailed descriptions of both the lithology and petrography of the Beavers Bend Tuff and the Hatton Tuff can be found in the Ph.D. dissertation by Niem (1971). Of the 46 samples of Stanley tuffs collected, 25 were chosen for thin section work with the purpose of characterizing modal mineralogy and diagenesis throughout the Beavers Bend Tuff, Hatton Tuff and Mud Creek Tuff sequences. The 25 samples are representative of the variety found in the Ouachita Mountains. A summary of their petrography is in Table 1. The effect of sedimentary processes (vertical sorting and sorting with distance) and diagenesis on the relative distribution of trace elements and REEs was documented, so that geochemical information pertaining to tuff petrogenesis can be discerned.

The tuffs are principally comprised of plagioclase, alkali feldspar, quartz, zircon, sphene and miscellaneous volcanic alteration products. Most of the tuffs are porphyritic, with the matrix material consisting of fine-grained quartz, chert, fine-grained muscovite/clay mineral

TABLE 1. Summary of Tuff Petrography

Sample	% phenocrysts	phenocrysts Qtz	Plag.	K-fsp	phenocryst sizes (mm)	matrix	comments
T-1	80	60	15	25	0.05-1.5	clays	crystal-rich, fresh feldspar, calcite cement
T-4	70	30	50	20	0.05-1.5	clays + chert	crystal rich, highly altered plag., calcite cement
T-5 XL	60	40		60	0.05-2.5	clays + chert	crystal-rich, all feldspar is highly altered
T-5 NXL	50	50		50	0.05-1.75	chert + qtz + clays	crystal-rich, all feldspar is highly altered, calcite cement
T-33	30	40	50	10	0.05-2	chert + qtz + clays	crystal-rich vitric tuff, plag. is completely altered, calcite cement
T-32	25	20	45	35	0.05-1.25	chert + qtz + clays	crystal-rich vitric tuff with some pseudomorphic glass shards, plag. completely altered
T-34	15	40	30	30	0.05-2.5	chert + qtz + clays + plag	crystalline-vitric tuff, feldspars partially altered, calcite cement
T-35	30	40	40	30	0.05-2	qtz + chert + clays + plag	crystalline-vitric tuff, plag. mostly altered, calcite cement
T-36	20	60	15	25	0.05-1	chert + clays + qtz	crystal-rich vitric tuff, plag. is completely altered, some K-spar alteration
T-37	25	10	60	30	0.05-2.5	chert + clays + qtz + plag	crystalline-vitric tuff, plag. is completely altered, some K-spar alteration, clay clasts (lapilli?)
T-38	10	80	10	10	0.05-0.2	qtz + chert + clays + plag	crystalline tuff, plag. is completely altered, some K spar alteration
T-39	30	20	45	35	0.05-2.25	qtz + chert + clays + plag	crystal-rich vitric tuff, plag. highly altered
T-40	15	90	10	0	0.05-0.25	qtz + chert + clays + plag	vitric tuff, plag. fairly fresh
T-41	40	25	40	35	0.05-3.5	qtz + chert + clays + plag	crystal-rich vitric tuff, plag. highly altered, clay clasts (lapilli?)
T-42	20	30	35	35	0.05-2	qtz + chert + clays + plag	crystal-rich vitric tuff, plag. highly altered, clay clasts (lapilli?), some calcite cement
T-57	15	90		10	0.05-0.75	chert + qtz + clays + plag	crystalline-vitric tuff, altered plag.
T-58	10	100	0	0	0.05-0.5	chert + clays + qtz	vitric, not as much of an angular shard-like texture
T-59A	15	40	35	25	0.05-1	chert + qtz + clays + plag	crystalline-vitric tuff, plag. highly altered, green clay clasts,
T-60A	40	30	60	10	0.05-3	chert + qtz + clays + plag	crystalline-vitric tuff, plag. highly altered, green clay clasts,
T-60B	40	35	45	20	0.05-1.5	chert + qtz + clays + plag	crystal-rich vitric tuff, plag. highly altered, some clay clasts
T-60C	35	35	45	20	0.05-1	chert + qtz + clays + plag	crystal-rich vitric tuff, plag. highly altered
T-60D	20	40		60	0.05-0.5	chert + qtz + clays + plag	crystal-rich vitric tuff, all feldspar is highly altered
T-60V	10	70	30	0	0.05-0.5	chert + qtz + clays	crystalline-vitric tuff
T-73	70	60		40	0.05-3.25	clays + chert	crystal rich, all feldspar is highly altered, green clasts (lapilli; now chlorite), calcite cement
T-77	20	50	20	30	0.05-1.25	chert + qtz + clays + plag	crystalline-vitric tuff, feldspar slightly altered,

(collectively referred to as clays) and authigenic feldspar. Quartz phenocrysts are typically embayed, with chert filling the pockets within the quartz crystals (Figure 15). Alkali feldspar and plagioclase make up the other phenocrysts. The plagioclase phenocrysts have undergone varying degrees of alteration to fine-grained muscovite/illite, with alteration ranging between fresh crystals having albite twinning and entirely altered crystals in which little of the original feldspar remains (Figure 16). Alteration is not as extensive in the alkali feldspar phenocrysts. Most of the alkali feldspars can be easily identified by their patchy, perthitic texture. An occassional Baveno twin (the only feldspar twin which is not parallel to crystal faces) can also be seen in the alkali feldspars (Figure 17).

Although the mineralogical composition of the matrix material remains fairly consistent between the tuffs, the texture of the matrix varies significantly. In some tuffs, angular pseudomorphs of glass shards can be readily identified (Figure 18). These glass pseudomorphs (both cuspate and platy-type glass shards) are filled with intergrown authigenic feldspar and quartz. Some or all of the authigenic feldspar is plagioclase, identifiable by its albite twinning. Unlike the plagioclase phenocrysts, the authigenic plagioclase is almost always fresh. The matrix surrounding the glass shards

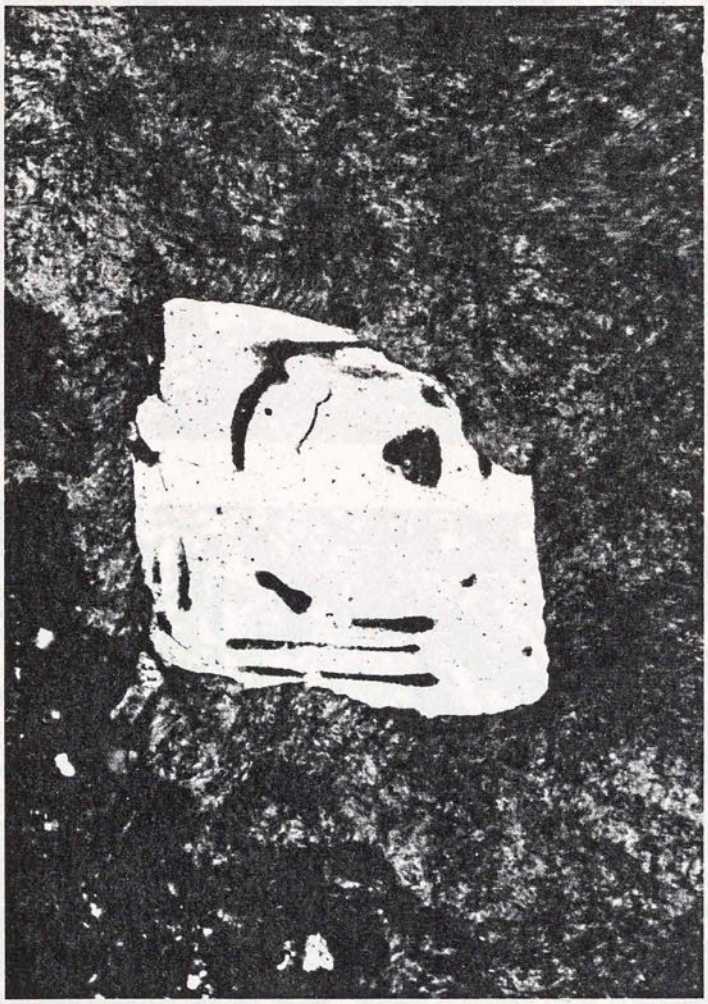

Figure 15. Embayed quartz crystal with chert filling the pockets; quartz grains is within a green lapilli clast.

a)

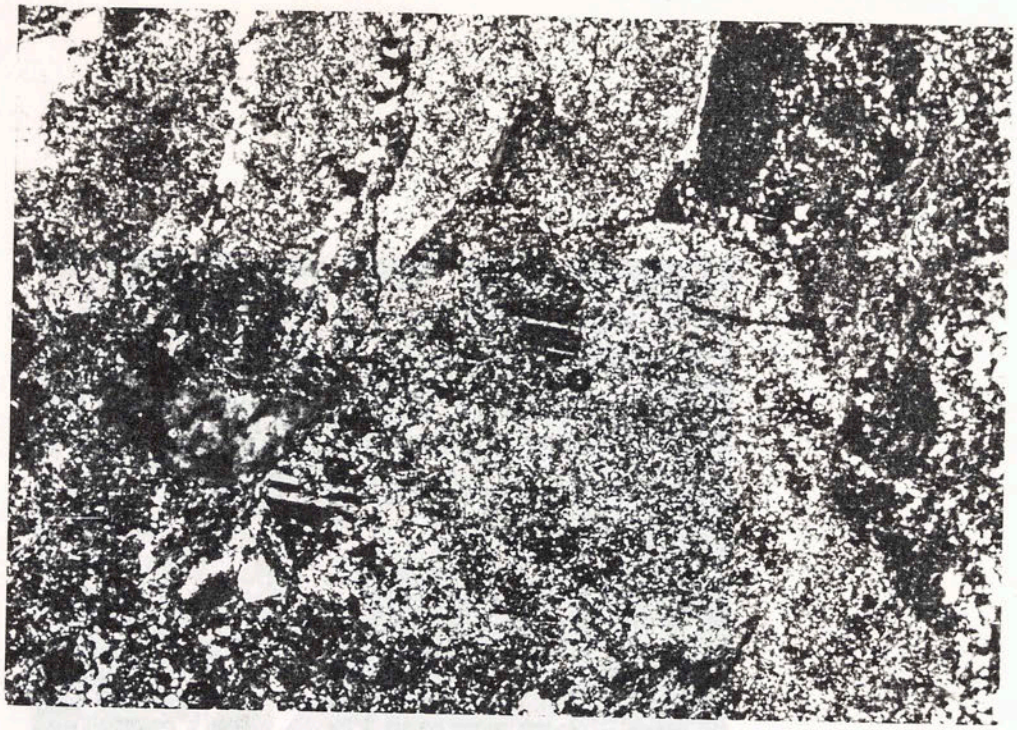

b)

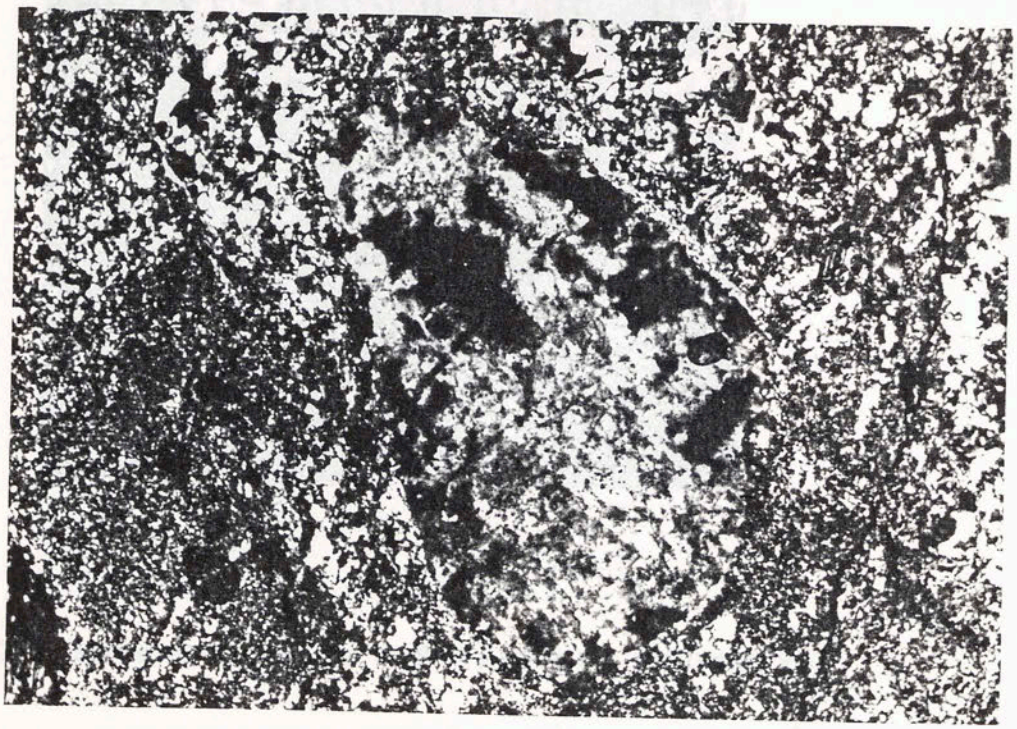

Figure 16. Feldspar alteration: a) severely altered plagioclase with some twinning evident, b) a relatively fresh K-feldspar phenocryst with patchy perthitic texture.

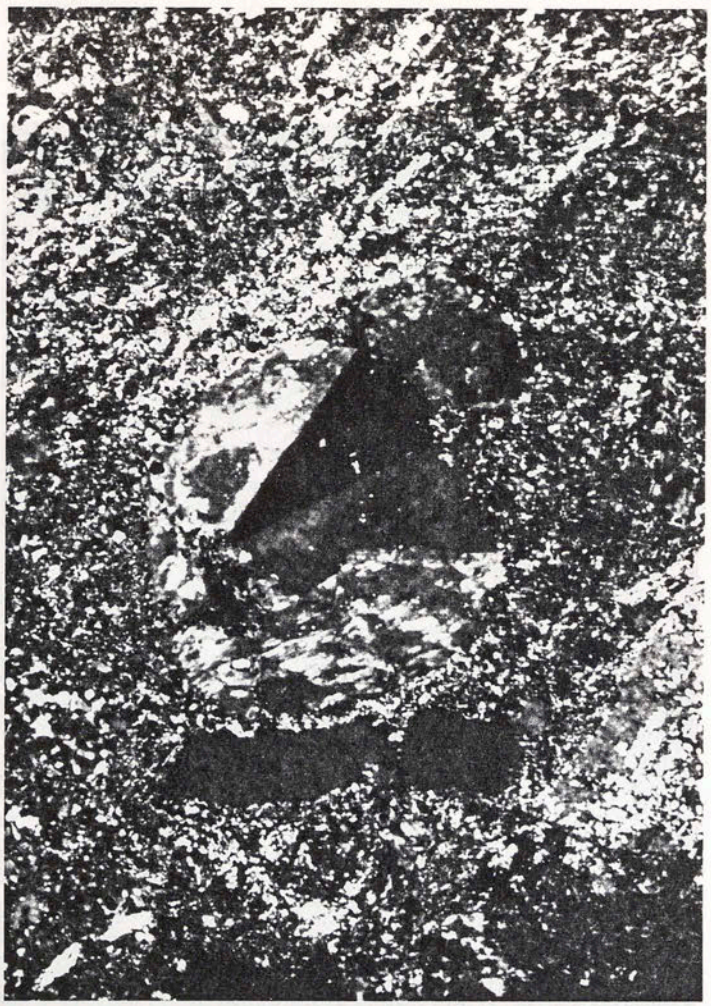

Figure 17. Baveno twin in a K-feldspar phenocryst.

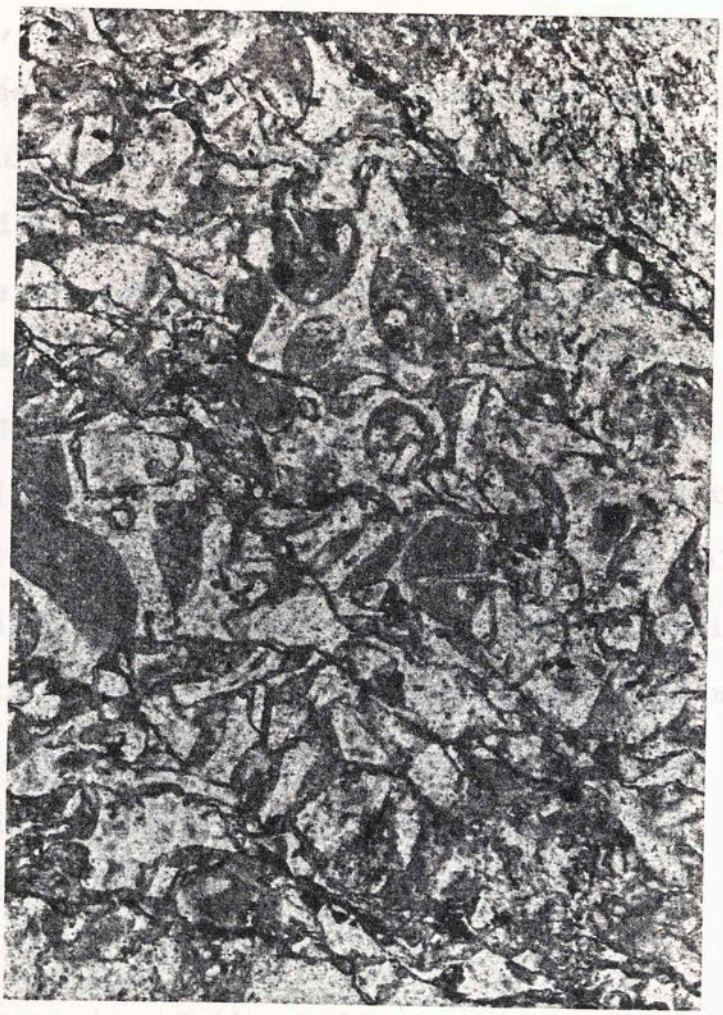

Figure 18. Cuspate and platy-type glass shard pseudomorphs in plane light.

consists of quartz + clays ± feldspar. The quartz is generally in the form of chert + polycrystalline quartz, with interspersed throughout. With diagenesis/metamorphism and time, most of the clays have been transformed into illite in the Stanley shales surrounding the tuffs (Houseknecht & Matthews, 1985). The tuffs have the same thermal and burial history as the shales, so it is assumed that the illitic clays in the tuffs have undergone the same transition (including those which are replacing feldspar phenocrysts). Where the clays are coarse-grained, they are referred to as fine-grained muscovite (or sericite). Some tuffs contain clasts of green clay (Figure 19). These have been identified as relic pumice lapilli (Niem, 1971). X-ray diffraction of the green clasts (Figure 20) shows that they are composed of celadonite, an Fe-rich illite which is very similar to glauconite. Typically, celadonite occurs as a diagenetic product in more mafic rocks where there is more Fe. Hay (1963) has used the term "celadonite subfacies" to diagenetically classify green pyroclastics.

Diagenesis of the tuffs consists of the following: 1) alteration of volcanic glass to chert/quartz + feldspar + clay, 2) alteration of plagiclase phenocrysts to either fine-grained muscovite and/or calcite, 3) alteration of K-feldspars to fine-grained muscovite and 4) a sporadic late-stage calcite

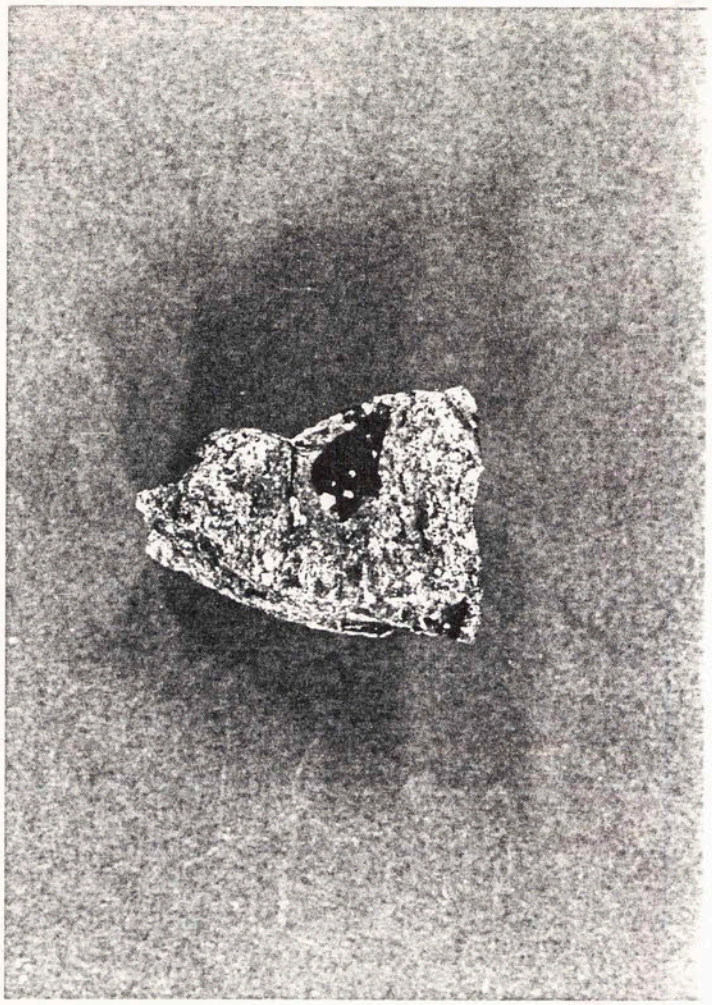

Figure 19. Green pumice lapilli with quartz phenocryst in the middle, Beavers Bend Tuff sample T-60a.

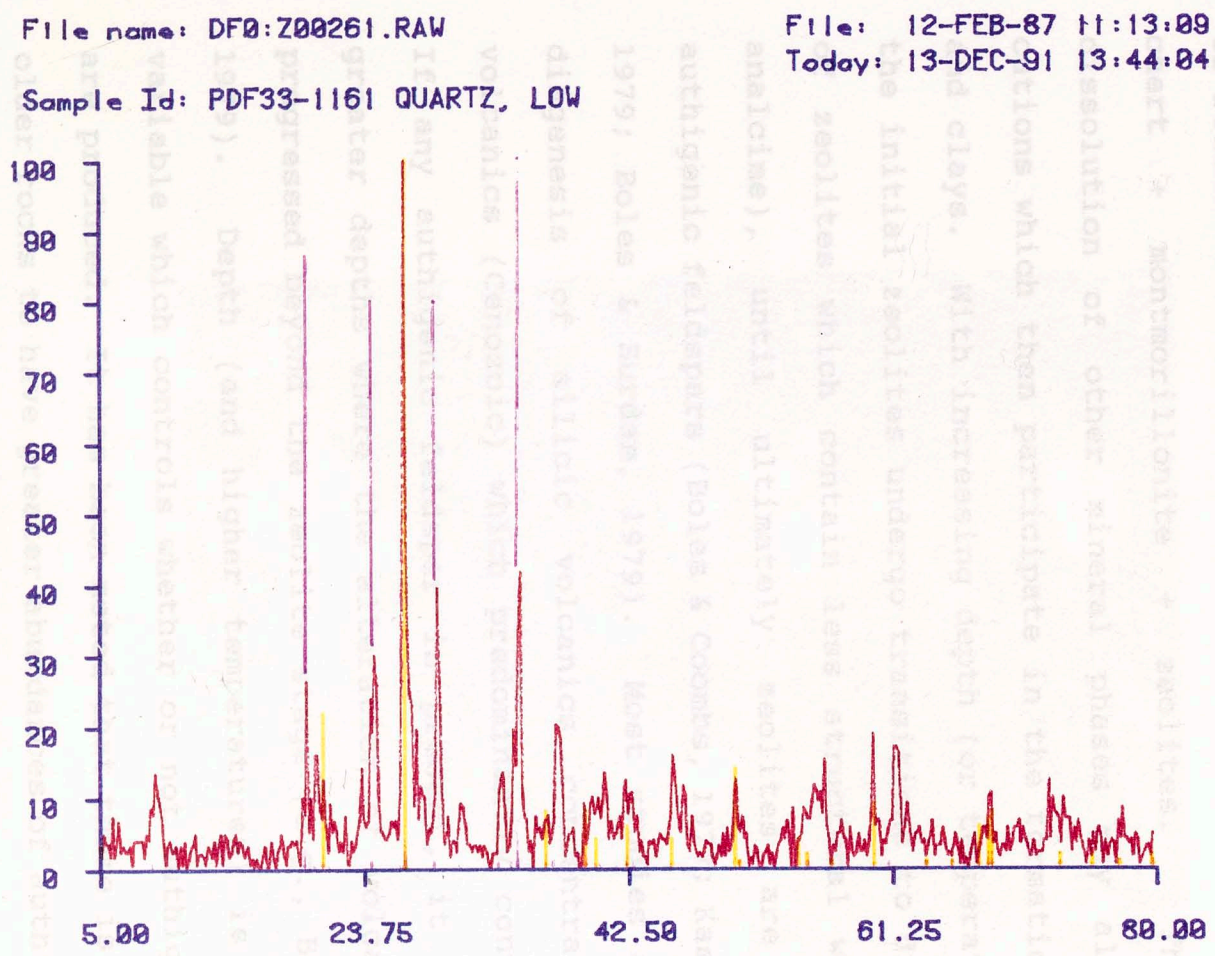

Figure 20. X-ray diffractogram of the green clasts within the Beavers Bend tuff. Purple marks celadonite peaks and yellow marks quartz peaks.

cementation (Figure 21). The alteration/diagenesis of silicic volcanics has been described by Hay (1966), Walton (1975),Boles and Coombs (1977), Boles and Surdam (1979), Kastner and Siever (1979), Sheppard and Gude (1969, 1973, 1986) and Forsman (1986) in great detail. The usual sequence of reactions involves the breakdown of volcanic glass to form chert + montmorillonite + zeolites. The concurrent dissolution of other mineral phases may also contribute cations which then participate in the formation of zeolites and clays. With increasing depth (or temperature or time), the initial zeolites undergo transitions to different types of zeolites which contain less structural water (such as analcime), until ultimately zeolites are replaced by authigenic feldspars (Boles & Coombs, 1977; Kastner & Siever, 1979; Boles & Surdam, 1979). Most studies addressing the diagenesis of silicic volcanics concentrate on recent volcanics (Cenozoic) which predominantly contain zeolites. If any authigenic feldspar is present, it is located at greater depths where the alteration of volcanic glass has progressed beyond the zeolite stage (e.g., Boles & Surdam, 1979). Depth (and higher temperatures) is the principal variable which controls whether or not authigenic feldspars are produced. It has been noted that there is a tendency for older rocks to have greater abundances of authigenic feldspar than younger rocks (Kastner & Siever, 1979). It follows that

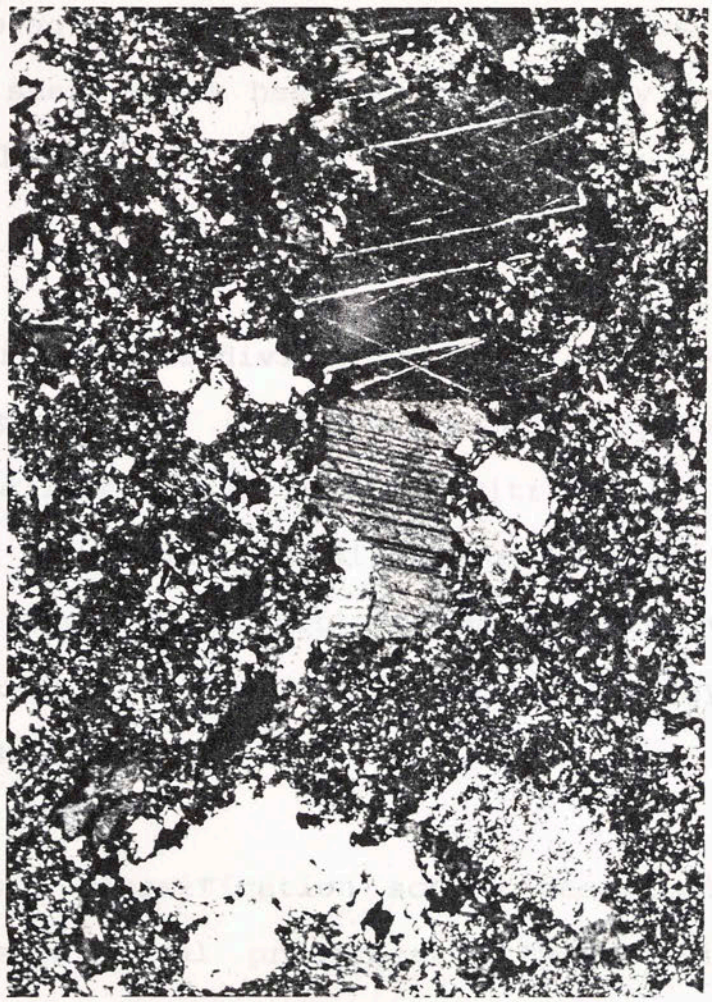

Figure 21. Calcite cementation in a Beavers Bend Tuff sample (T-35).

in older volcanics (volcanics older than the Cenozoic), time becomes the dominant variable; the zeolites formed initially from alteration of volcanic glass have since been replaced by authigenic feldspar. It is inferred that this is what is seen in the Stanley tuffs. The absence of zeolites implies that alteration of the glass shards has progressed to the quartz + clays + plagioclase stage. Figure 22 shows a pseudomorph of a glass shard which has been replaced by polycrystalline quartz + plagioclase and is surrounded by a chert + clay matrix.

The tuffs can be divided into four different categories based on petrography: crystal-rich tuff, crystal-rich vitric tuff, crystalline vitric tuff and vitric tuff. These names are not a rigorous classification scheme, but merely descriptive terms which reflect the relative variations in tuff petrography. Definitions of the terminology employed are shown in Table 2.

The tuff classification scheme described in Table 2 reflects depositional processes. Pyroclastic rocks, in general, can be separated into two groups: pyroclastic falls and pyroclastic flows. Both groups involve the explosive eruption of silicic, gaseous volcanic fragments. Pyroclastic falls are formed by the ejection of volcanic material into the

Figure 22. Glass pseudomorph (evident in plane light in photo (a)) replaced by authigenic feldspar and quartz (b).

TABLE 2. Tuff Classification Scheme

Classification Term	Definition
crystal-rich tuff	Tuff is almost entirely crystals with a clay + quartz matrix; there is no evidence of a vitric texture as pseudomorphic glass shards are absent.
crystal-rich vitric tuff	Tuff is predominantly phenocrysts + crystals (in the matrix) with some pseudomorphic glass shards.
crystalline-vitric tuff	Tuff is largely comprised of matrix material which has pseudomorphic glass shards; less than 30% phenocrysts, maximum crystal sizes range between 1-3mm.
vitric tuff	Fine-grained matrix with less than 15% phenocrysts, phenocrysts are no larger than 0.5mm.

atmosphere, followed by aeolian transport and sorting. Pyroclastic flows differ from air falls in that the gas and volcanic fragments are erupted as a coherent mass which then moves along the ground. Both types of pyroclastic rocks are found in the Stanley Group. The presence of large phenocrysts (on the order of 1-2mm in size), ripped-up shale clasts (Figure 23) and displaced shallow-water fauna in the crystal-rich tuffs are evidence that some of these tuffs are submarine pyroclastic flows (Niem, 1971), termed hyaloclastites. The vitric tuffs (crystalline-vitric and vitric) do not have ripped-up shale clasts and other foreign material. Moreover, they are better sorted and predominantly comprised of glass shards, pumice and finer-grained angular quartz and feldspar. This suggests that deposition was as volcanic material settling out of the air and through the water (Niem, 1971). The small percentage of phenocrysts and their small sizes in some of the samples reflect their aerial mode of transport.

Rhyolites

Five thin sections were prepared from the rhyolite cored in the Temple well. The upper portion (4792-4797m) of the rhyolite units has been classified as a devitrified rhyolitic pitchstone, while the lower part (4831-4837m) is an amygdaloidal spherulitic rhyolite (Nicholas, R.L., pers. comm.). The pitchstone (Figure 24) has quartz and plagioclase

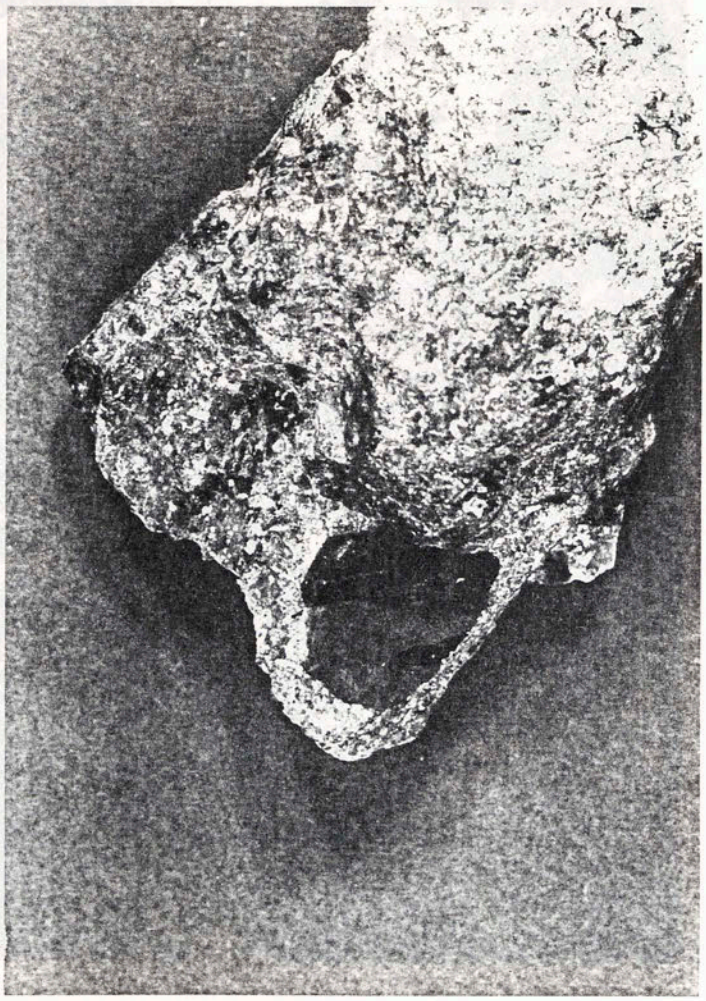

Figure 23. Ripped up shale clast in a Hatton Tuff sample (T-78).

Figure 24. Rhyolite pitchstone in crossed nichols; altered feldspar phenocrysts (with calcite) and a perlitic texture in the matrix (Sabine rhyolite sample T-43 from the Temple well at a depth of 4790m).

phenocrysts, flow structures and xenoliths of foreign rock material. The perlitic texture is caused by low-temperature adsorption of water into the glass. The amygdaloidal rhyolite has quartz, plagioclase and K-feldspar phenocrysts, a spherulitic texture. The spherulites are a result of devitrification of the volcanic glass.

RESULTS

Based upon major element abundances (Tables 3-8), the tuffs can be characterized as being sub-alkaline dacitic to rhyolitic (Figure 25; classification scheme based upon Le Bas et al., 1986). SiO_2 ranges between 63-82 weight percent, with K_2O+Na_2O values falling between 2-8 weight percent. Those tuffs that fall between 75-78 wt. % SiO_2 are classified as high-silica rhyolitic tuffs (Hildreth, 1981). A geochemical comparison of the Stanley tuffs and the rhyolite cores from the Temple well in Sabine County, Texas shows a close similarity in geochemistry. If ratios of immobile trace elements are compared (Figure 26), it can be seen that the Sabine rhyolites fall within the ratio values of the Stanley tuffs. The results of Student's t-tests also reflect a similarity in composition (Figure 27). The abundance of each element in the Stanley tuffs was compared with the element abundances in the samples from the rhyolite cored in the

TABLE 3. RATTLESNAKE BLUFF, BEAVERS BEND STATE PARK

	Beaver's Bend Tuff						
	T-32	T-33	T-34	T-35	T-36	T-37	T-38
SiO_2	78.19	73.84	82.41	76.01	77.46	79.65	81.98
Al_2O_3	12.27	14.12	9.77	13.92	13.24	11.89	10.76
P_2O_5	0.04	0.07	0.03	0.04	0.04	0.04	0.02
CaO	0.39	1.06	0.62	0.08	0.01	0.00	0.00
TiO_2	0.32	0.39	0.25	0.29	0.34	0.18	0.18
Fe_2O_3	3.00	3.68	2.12	2.73	3.12	1.60	1.62
Na_2O	0.78	1.78	2.40	4.16	0.72	3.81	2.48
K_2O	4.01	4.05	1.79	2.17	3.99	2.58	2.72
MgO	0.98	1.00	0.62	0.59	1.06	0.25	0.34
MnO	0.00	0.01	0.00	0.01	0.03	0.00	0.00
XRF							
Nb	11	11	10	13	12	9	11
Zr	205	230	172	205	217	138	160
Y	53	28	26	35	35	27	34
Sr	37	85	62	62	20	47	28
Rb	179	189	86	114	188	116	122
Th	19	15	17	23	19	16	21
Pb	20	18	19	19	16	24	12
Zn	56	61	48	57	75	44	46
Sc	8	10	6	8	8	4	6
Ba	658	721	304	425	753	709	583
La	29	27	35	31	38	42	25
Ce	61	58	72	66	73	70	67
Nd	27	25	30	29	32	31	27
INAA							
La		37.1	47.9		43.8	46.5	37.6
Ce		70.5	87.7		86.2	85.1	76.2
Nd		28.6	36.5		21.5	37.5	32.6
Sm		5.82	6.93		4.54	6.84	6.59
Eu		1.08	0.75		1.11	0.73	0.47
Tb		0.95	0.85		1.08	0.87	1.02
Yb		3.04	3.19		3.72	2.97	3.40
Lu		0.45	0.44		0.52	0.41	0.52
Ta		1.02	0.94		1.17	0.77	1.06
Hf		6.64	5.09		6.29	3.89	5.00
Co		3.6	1.7		4.6	1.3	0.7
Cr		17.7	12.0		17.1	5.0	6.4
Sc		9.0	5.9		8.0	4.5	5.3
Cs		6.3	2.8		6.0	2.7	3.0

Table 3. cont.

	Hatton Tuff			
	T-39	T-40	T-41	T-42
SiO_2	77.08	80.87	77.69	74.71
Al_2O_3	12.99	11.31	12.87	14.01
P_2O_5	0.03	0.03	0.04	0.03
CaO	0.16	0.00	0.24	0.78
TiO2	0.21	0.16	0.21	0.28
Fe_2O_3	2.41	1.58	1.90	2.56
Na_2O	4.70	3.66	3.98	4.48
K_2O	2.09	2.06	2.73	2.71
MgO	0.29	0.35	0.34	0.46
MnO	0.03	0.00	0.02	0.00
XRF				
Nb	11	11	10	13
Zr	160	147	160	209
Y	29	30	29	35
Sr	79	48	81	128
Rb	94	105	124	132
Th	20	21	18	27
Pb	21	16	21	29
Zn	70	47	50	63
Sc	7	6	6	9
Ba	616	440	748	649
La	31	29	33	31
Ce	65	56	65	70
Nd	28	24	27	30
INAA				
La	42.0	34.4	46.4	48.7
Ce	83.4	73.0	85.5	96.5
Nd	37.0	32.5	39.3	42.6
Sm	7.07	5.97	7.17	7.67
Eu	0.68	0.43	0.80	0.74
Tb	0.93	0.87	0.93	1.21
Yb	3.60	3.75	3.19	4.56
Lu	0.50	0.52	0.47	0.64
Ta	1.14	1.08	1.02	1.48
Hf	5.23	4.69	5.02	7.07
Co	1.7	0.6	1.4	2.4
Cr	6.3	5.6	6.2	10.8
Sc	6.1	5.3	5.9	7.4
Cs	3.2	3.2	3.4	3.9

TABLE 4. BEAVERS BEND TUFF SECTION, ARKANSAS/OKLAHOMA BORDER

	T-60A	T-60B	T-60C	T-60D	T-60E	T-60V
SiO_2	76.11	76.54	75.61	78.48	82.16	76.73
Al_2O_3	13.60	12.75	14.67	14.30	12.07	18.10
P_2O_5	0.03	0.04	0.02	0.02	0.01	0.02
CaO	0.00	0.10	0.08	0.00	0.00	0.00
TiO_2	0.27	0.31	0.27	0.26	0.17	0.26
Fe_2O_3	2.29	2.95	2.45	2.47	1.95	2.33
Na_2O	2.66	3.36	2.97	1.48	0.00	0.32
K_2O	4.72	3.60	3.49	2.68	2.99	1.84
MgO	0.39	0.36	0.45	0.41	0.94	0.47
MnO	0.00	0.00	0.00	0.00	0.00	0.00
XRF						
Nb	13	12	14	14	11	18
Zr	202	220	220	219	149	214
Y	29	37	37	32	26	42
Sr	50	60	44	21	2	6
Rb	175	133	161	126	152	125
Th	21	21	25	28	21	32
Pb	20	23	13	20	9	28
Zn	49	67	46	56	30	44
Sc	8	9	7	7	6	12
Ba	1198	1028	763	466	469	240
La	31	33	43	40	28	62
Ce	70	70	88	81	60	123
Nd	27	29	36	30	25	46

TABLE 5. BEAVERS BEND TUFF, OUACHITA MOUNTAINS

	T-4	T-55A	T-55B	T-55C	T-56	T-57	T-59A
SiO_2	74.27	77.29	77.72	80.50	80.86	79.36	79.78
Al_2O_3	13.52	13.19	12.11	11.74	11.56	14.07	12.26
P_2O_5	0.05	0.01	0.04	0.02	0.02	0.02	0.01
CaO	1.31	0.00	0.67	0.06	0.00	0.00	0.00
TiO_2	0.24	0.32	0.29	0.23	0.24	0.22	0.20
Fe_2O_3	2.7	1.47	2.01	1.11	1.99	2.20	1.48
Na_2O	5.15	3.79	4.92	3.67	4.07	0.00	2.87
K_2O	2.95	3.09	3.07	2.46	1.26	4.27	3.49
MgO	0.37	0.30	0.36	0.28	0.38	1.08	0.31
MnO	0.07	0.00	0.07	0.00	0.00	0.00	0.00
XRF							
Nb	11	12	11	12	11	12	12
Zr	184	212	198	182	169	177	169
Y	32	32	31	31	31	38	29
Sr	192	75	114	45	44	6	28
Rb	119	130	112	95	71	204	136
Th	20	19	19	22	20	24	21
Pb	24	19	21	15	18	23	9
Zn	51	69	77	24	55	45	34
Sc	10	9	6	5	8	8	6
Ba	916	764	829	513	251	617	638
La	26	37	24	37	41	40	37
Ce	53	76	56	72	65	80	69
Nd	20	31	24	29	28	33	28

TABLE 5 cont.

	T-59B	T-59C	T-74	T-75	T-76	T-77	T-80
SiO_2	76.41	77.42	79.00	78.71	81.62	81.67	79.34
Al_2O_3	13.4	13.86	13.48	12.99	11.25	11.03	12.58
P_2O_5	0.02	0.01	0.02	0.02	0.03	0.02	0.01
CaO	0.08	0.00	0.00	0.00	0.00	0.00	0.00
TiO_2	0.29	0.25	0.25	0.23	0.26	0.18	0.25
Fe_2O_3	2.08	2.19	2.22	1.79	1.89	1.89	1.94
Na_2O	2.91	2.58	2.24	2.70	2.90	3.64	3.51
K_2O	3.88	4.28	2.91	3.19	2.20	1.59	1.89
MgO	0.42	0.28	0.37	0.34	0.41	0.32	0.37
MnO	0.00	0.00	0.00	0.00	0.01	0.00	0.00
XRF							
Nb	12	12	12	12	10	11	11
Zr	207	191	183	177	169	154	173
Y	33	29	34	43	28	30	27
Sr	47	42	32	36	64	43	58
Rb	160	163	137	140	99	95	109
Th	21	21	23	21	17	21	21
Pb	26	16	23	14	17	20	15
Zn	37	40	46	34	48	50	52
Sc	8	7	6	7	5	7	7
Ba	959	1073	557	590	507	277	428
La	37	26	35	39	34	34	32
Ce	75	56	70	75	59	75	69
Nd	32	20	30	34	26	29	28

TABLE 5 cont.

	T-81
SiO_2	81.63
Al_2O_3	11.53
P_2O_5	0.02
CaO	0.00
TiO_2	0.21
Fe_2O_3	1.84
Na_2O	3.11
K_2O	1.51
MgO	0.38
MnO	0.00
XRF	
Nb	10
Zr	153
Y	28
Sr	48
Rb	83
Th	19
Pb	22
Zn	55
Sc	4
Ba	322
La	24
Ce	58
Nd	24

TABLE 6. HATTON TUFF, OUACHITA MOUNTAINS

	T-71	T-72	T-78
SiO_2	75.94	80.06	79.62
Al_2O_3	13.84	12.32	12.01
P_2O_5	0.04	0.03	0.03
CaO	0.12	0.03	0.39
TiO_2	0.26	0.35	0.20
Fe_2O_3	2.47	1.56	1.74
Na_2O	4.00	3.54	4.22
K_2O	3.77	2.17	1.72
MgO	0.39	0.32	0.32
MnO	0.00	0.00	0.00
XRF			
Nb	13	11	10
Zr	201	226	155
Y	35	35	26
Sr	80	90	58
Rb	154	83	100
Th	22	16	17
Pb	26	19	22
Zn	53	39	46
Sc	7	6	5
Ba	803	852	421
La	35	33	26
Ce	73	65	53
Nd	30	32	23

TABLE 7. MUD CREEK TUFFS, OUACHITA MOUNTAINS

	T-1	T-3	T-5A	T-5B	T-7	T-29
SiO_2	71.77	77.64	71.68	74.68	78.22	67.56
Al_2O_3	14.07	12.77	15.51	14.48	12.36	14.84
P_2O_5	0.16	0.11	0.15	0.10	0.10	0.13
CaO	2.99	0.01	0.35	0.62	0.58	4.32
TiO_2	0.62	0.94	0.69	0.48	0.50	0.54
Fe_2O_3	4.85	4.36	3.70	3.16	3.46	5.26
Na_2O	2.85	1.43	3.28	3.54	1.88	2.91
K_2O	1.78	2.29	2.42	2.99	2.67	1.34
MgO	1.22	0.96	1.02	1.14	1.53	1.14
MnO	0.09	0.01	n.d.	0.03	0.01	0.12
XRF						
Nb	11	15	12	11	12	9
Zr	235	325	275	225	195	194
Y	25	30	21	27	26	22
Sr	189	46	148	90	86	242
Rb	78	103	112	140	107	51
Th	4	9	10	16	10	10
Pb	13	10	15	21	22	18
Zn	72	61	42	50	53	67
Sc	12	13	12	8	8	11
Ba	1027	579	704	802	468	3445
La	28	35	25	30	25	26
Ce	52	71	52	63	57	43
Nd	21	33	24		25	18
INAA						
La	30.6		34.1	38.9		30.9
Ce	59.3		65.7	69.3		58.5
Nd	25.6		26.8	27.8		25.2
Sm	5.10		4.94	5.05		5.05
Eu	1.12		1.07	1.24		1.33
Tb	0.67		0.64	0.75		0.73
Yb	2.34		2.19	2.74		2.30
Lu	0.35		0.33	0.41		0.32
Ta	0.89		0.93	0.99		0.78
Hf	6.18		7.11	5.62		5.03
Co	7.6		4.9	6.5		5.2
Cr	32.0		19.1	17.3		26.6
Sc	8.7		10.2	7.3		8.6
Cs	3.0		2.7	5.8		2.2

TABLE 7 cont.

	T-58	T-73	T-79A	T-79B	T-82
SiO_2	68.44	66.56	70.78	63.32	71.49
Al_2O_3	17.53	15.47	14.79	17.22	14.24
P_2O_5	0.11	0.21	0.14	0.21	0.13
CaO	0.23	2.66	1.08	1.16	1.35
TiO_2	0.59	0.84	0.61	0.79	0.76
Fe_2O_3	4.26	5.75	4.13	7.49	5.10
Na_2O	3.89	2.72	4.80	5.51	3.01
K_2O	3.21	2.52	1.46	1.21	2.26
MgO	1.13	1.79	1.65	2.31	1.40
MnO	0.00	0.06	0.03	0.10	0.03
XRF					
Nb	10	14	12	12	13
Zr	210	404	281	341	306
Y	33	33	30	23	25
Sr	127	278	267	432	162
Rb	136	105	57	39	102
Th	8	12	14	5	14
Pb	16	21	18	12	17
Zn	100	91	69	101	75
Sc	11	16	12	19	13
Ba	873	1072	649	1158	608
La	50	39	38	27	27
Ce	86	71	68	57	61
Nd	43	30	31	28	27

TABLE 8. RHYOLITES, SABINE COUNTY, TEXAS

	Temple #1					Jones #1
	T-43	T-44	T-45	T-46	T-47	T-48
SiO_2	77.93	74.86	77.29	79.89	83.05	69.70
Al_2O_3	13.25	14.53	12.35	11.12	10.46	14.36
P_2O_5	0.00	0.01	0.01	0.01	0.01	0.03
CaO	0.05	0.78	0.49	1.31	0.32	0.43
TiO_2	0.05	0.10	0.08	0.06	0.05	0.15
Fe_2O_3	0.53	1.12	0.81	1.01	0.38	8.13
Na_2O	2.11	0.50	2.14	0.41	2.03	0.16
K_2O	5.73	4.83	5.15	3.63	4.66	4.83
MgO	0.28	1.78	0.24	1.78	0.19	1.04
MnO	0.00	0.03	0.00	0.07	0.00	0.00
XRF						
Nb	9	11	13	13	10	11
Zr	83	110	102	90	79	161
Y	46	53	71	44	53	23
Sr	14	15	37	29	29	39
Rb	219	263	200	228	177	222
Th	13	18	19	21	15	64
Pb	7	10	7	8	12	3540
Zn	27	32	20	18	21	69
Sc	3	5	4	2	4	6
Ba	104	120	313	269	268	268
La	21	34	16	11	3	35
Ce	68	104	62	40	23	81
Nd	31	50	24	22	12	33
INAA						
La	29.8	43.5	26.4	20.9	11.9	46.7
Ce	75.8	120.4	78.0	56.1	30.9	104.8
Nd	37.4	57.5	35.5	27.9	14.9	46.1
Sm	9.19	14.05	8.65	7.76	4.36	8.19
Eu	0.54	0.72	0.40	0.32	0.21	1.03
Tb	1.53	1.88	1.69	1.53	1.38	0.85
Yb	4.41	5.30	6.98	5.13	5.31	2.54
Lu	0.59	0.73	0.95	0.67	0.71	0.35
Ta	0.93	1.26	1.38	1.78	1.16	1.26
Hf	3.24	4.64	4.37	4.79	3.50	5.37
Co	0.5	0.5	0.5	0.1	0.5	12.2
Cr	1.2	1.7	1.7	1.6	1.4	6.1
Sc	2.7	3.2	3.2	3.0	2.7	4.6
Cs	9.6	13.1	3.2	3.8	1.3	5.1

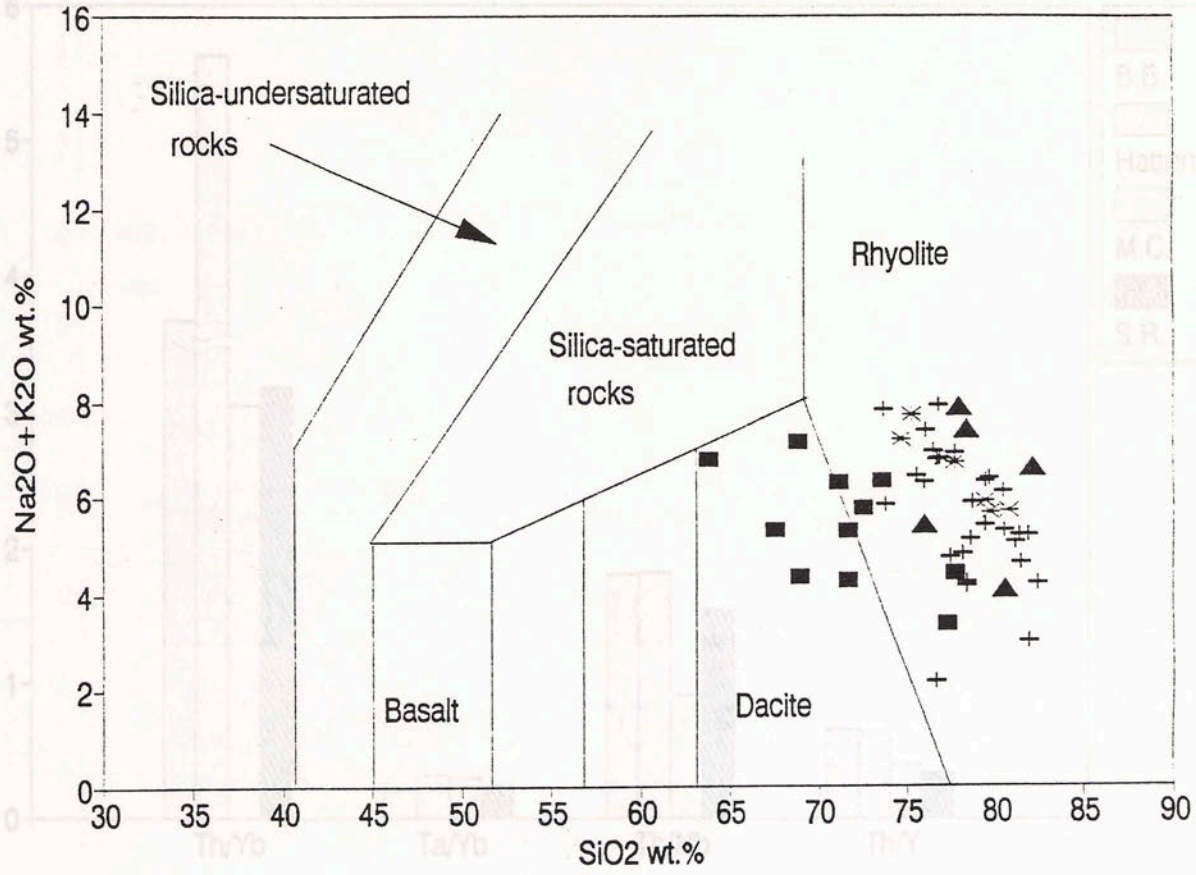

Figure 25. Classification of tuffs and rhyolites. Solid triangles, Sabine rhyolites; pluses, Beavers Bend Tuff; asterisks, Hatton Tuff; solid squares, Mud Creek Tuffs.

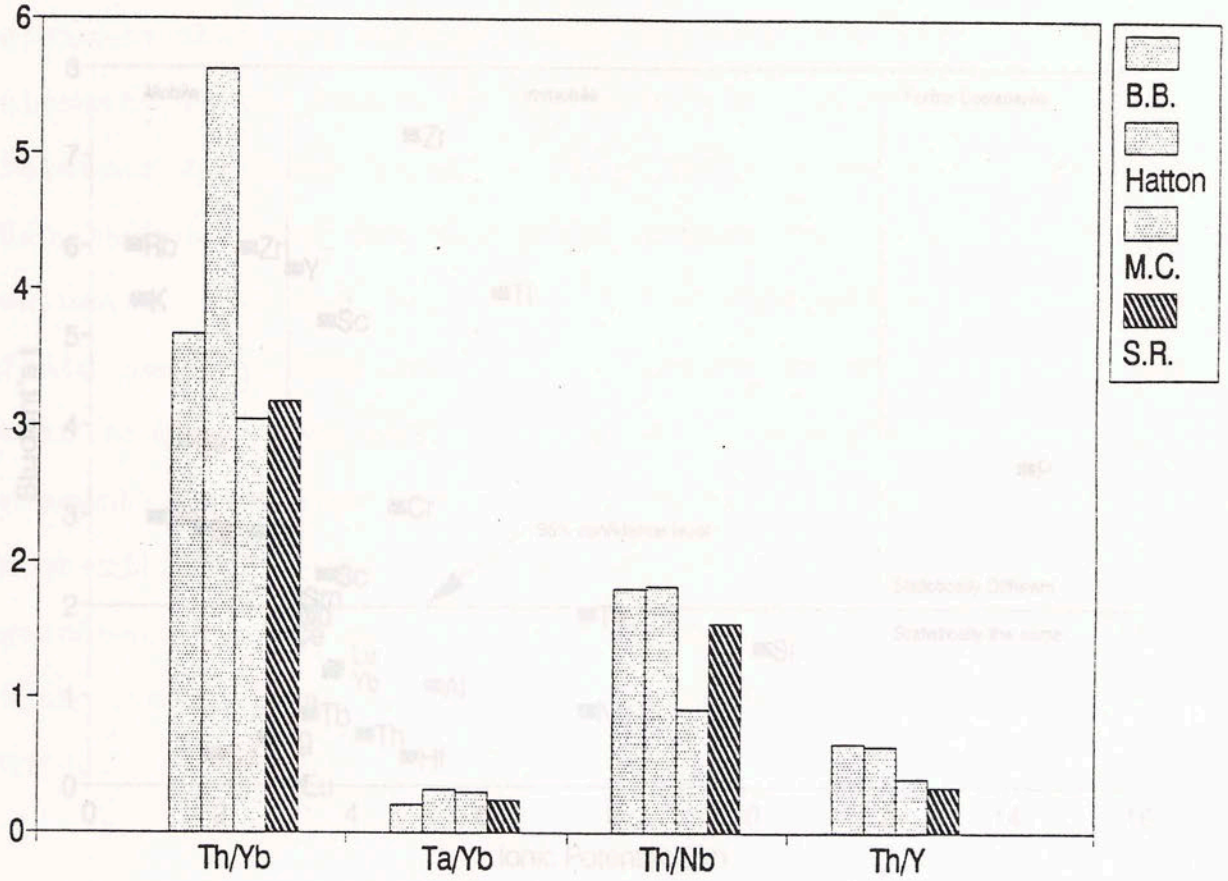

Figure 26. Comparison of trace element ratios between the Stanley tuffs (B.B.= Beavers Bend, M.C.= Mud Creek tuffs) and the Sabine Rhyolite (S.R.).

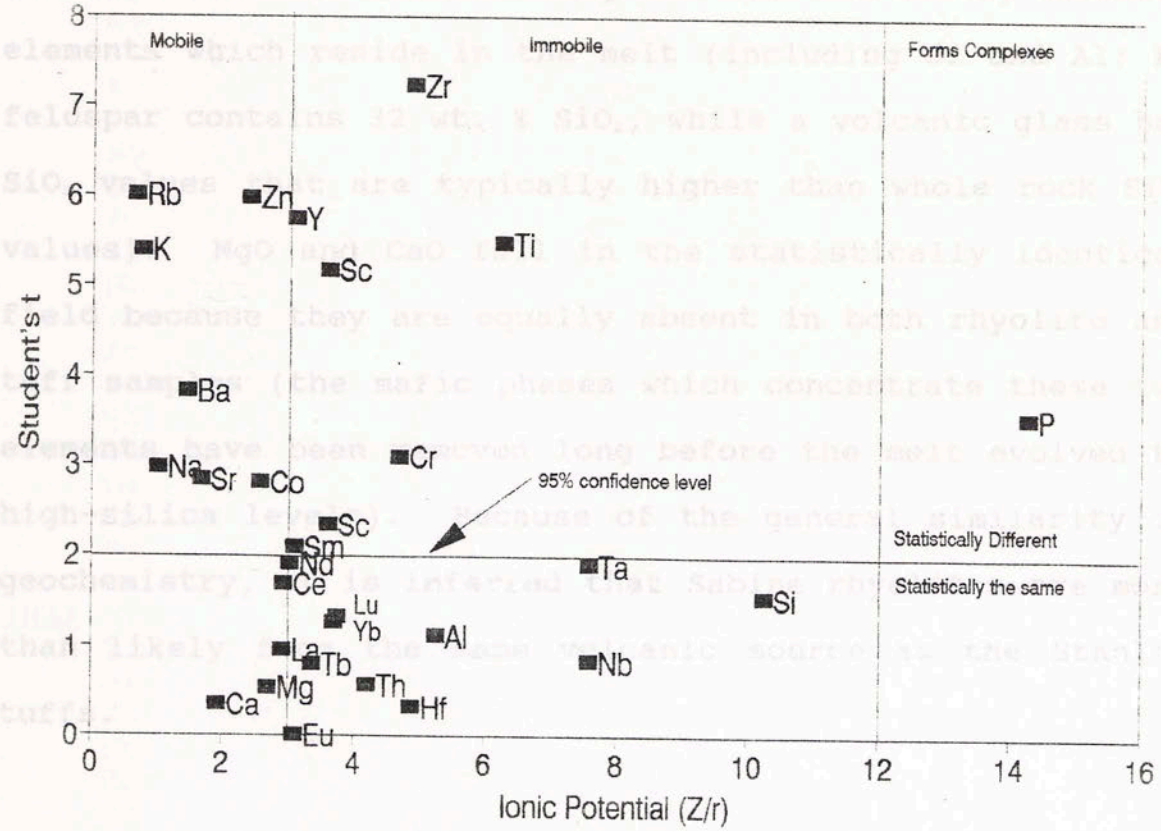

Figure 27. Comparison of the degree of geochemical similarity between the tuffs and rhyolite with ionic potential. The degree of element mobility is independent of whether or not element abundances are statistically comparable.

Temple well, using t-tests (see Table 9). Most of the elements that plot in the "statistically different" field are those which reside in mineral phases that are affected by differential settling during deposition; namely, feldspar, Fe-Ti oxides and other heavy minerals such as zircon. The elements that are statistically the same are mostly immobile elements which reside in the melt (including Si and Al; K-feldspar contains 32 wt. % SiO_2, while a volcanic glass has SiO_2 values that are typically higher than whole rock SiO_2 values). MgO and CaO fall in the statistically identical field because they are equally absent in both rhyolite and tuff samples (the mafic phases which concentrate these two elements have been removed long before the melt evolved to high-silica levels). Because of the general similarity in geochemistry, it is inferred that Sabine rhyolites are more than likely from the same volcanic source as the Stanley tuffs.

Before rhyolite and tuff petrogenesis can be addressed, post-eruptive processes which might change relative elemental distributions must be characterized.

Graded Bedding

Two different sites have tuff exposures at which fining-upward units that can be clearly seen. The basal portions of the units have high abundances of feldspar and quartz

TABLE 9. Student's T-Test

Element	Tuffs x	Tuffs σ	Rhyolite x	Rhyolite σ	σ_{t-r}*	t-test**
XRF						
Si	76.65	4.08	79.01	2.37	3.22	1.56
Ti	0.35	0.15	0.07	0.02	0.09	6.99
Al	13.34	1.66	12.42	1.73	1.69	1.16
Fe	2.74	1.30	0.78	0.32	0.81	5.16
Mg	0.69	0.40	0.86	0.86	0.63	0.58
Ca	0.48	1.37	0.60	0.49	0.93	0.26
Na	2.99	1.30	1.44	0.90	1.10	3.00
K	2.70	0.73	4.83	0.77	0.75	6.02
P	0.05	0.04	0.01	0.00	0.02	4.63
Nb	12	1.68	11	1.73	1.71	0.83
Zr	206	67.70	93	12.88	40.29	6.01
Y	31	4.17	53	10.55	7.36	6.38
Sr	88	110.92	25	9.93	60.42	2.20
Rb	121	33.38	217	32.10	32.74	6.29
Th	18	3.77	17	3.27	3.52	0.72
Pb	19	3.88	9	2.30	3.09	6.84
Zn	55	19.67	24	5.95	12.81	5.26
Sc	8	3.09	3	1.05	2.07	5.09
Ba	728	829.24	215	95.85	462.54	2.36
La	33	8.00	17	11.49	9.75	3.61
Ce	67	11.67	60	30.81	21.24	0.77
Nd	28	6.65	28	14.15	10.40	0.14
INAA						
La	39.9	7.62	26.5	11.68	9.65	0.70
Ce	76.7	12.18	72.2	32.93	22.56	1.52
Nd	31.8	5.54	34.6	15.55	10.55	1.57
Sm	6.06	0.78	8.80	3.48	2.13	2.09
Eu	0.89	0.23	0.44	0.20	0.22	0.27
Tb	0.88	0.07	1.60	0.19	0.13	1.51
Yb	3.15	0.11	5.43	0.94	0.53	2.63
Lu	0.45	0.01	0.73	0.13	0.07	2.97
Ta	1.02	0.06	1.30	0.31	0.19	2.29
Hf	5.60	1.10	4.11	0.70	0.90	0.74
Co	3.2	1.31	0.4	0.17	0.74	2.56
Cr	14.0	4.00	1.5	0.23	2.11	2.95
Sc	7.1	2.21	3.0	0.26	1.23	2.62

*σ_{t-r} -- $(\sigma_{tuff}+\sigma_{rhyolite})/2$ for every element

**t-test --confidence level is 95% at t=2.00, elements having t>2.00 have statistically different abundances; elements having t<2.00 have abundances which are statistically the same

phenocrysts, while the upper portions of the units have few (if any) phenocrysts, and greater amounts of glass pseudomorphs. The two sites are located at Rattlesnake Bluff (where both the Beavers Bend and Hatton Tuffs were sampled) and a site 1 mile east of the Oklahoma/Arkansas border, north of the Cross Mountains (the T-60 series where the Beavers Bend Tuff was sampled). Together, the Beavers Bend Tuff at Rattlesnake Bluff and the T-60 series show that the tuff beds are not only vertically graded, but horizontally graded as well. The Beavers Bend Tuff at Rattlesnake Bluff is a thick, massive unit containing both crystal-rich and less crystalline units. It is only the top unit where the distinct green clasts in a white crystalline matrix are found; this is the portion of the Beavers Bend Tuff which has been found surrounding the Broken Bow uplift and the Cross Mountains. This top unit is the basal unit at the T-60 site in Arkansas. Upwards, the T-60 tuff becomes increasingly vitric with fewer and smaller crystals. Together, these two sites represent a decrease in average grain size with distance towards the north. This vertical and horizontal grain size segregation can be seen in the hand samples shown in Figure 28.

Figure 29 compares the total percent of feldspar phenocrysts to the percent of K_2O+Na_2O in the T-60 Beavers Bend sequence. Trends in total feldspar phenocrysts and total

a)

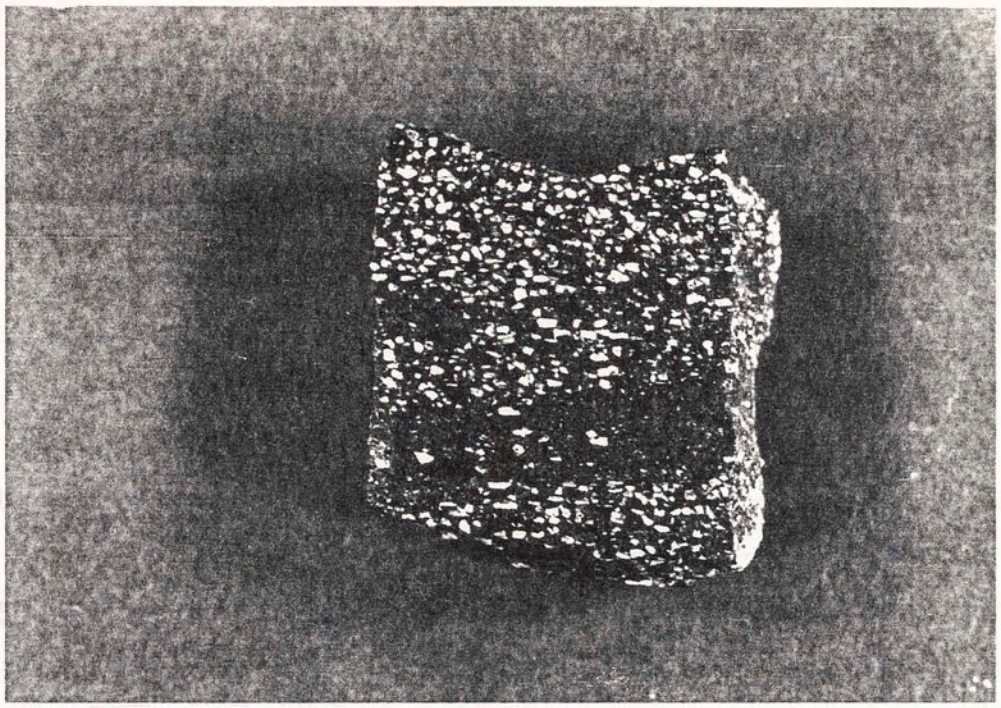

b)

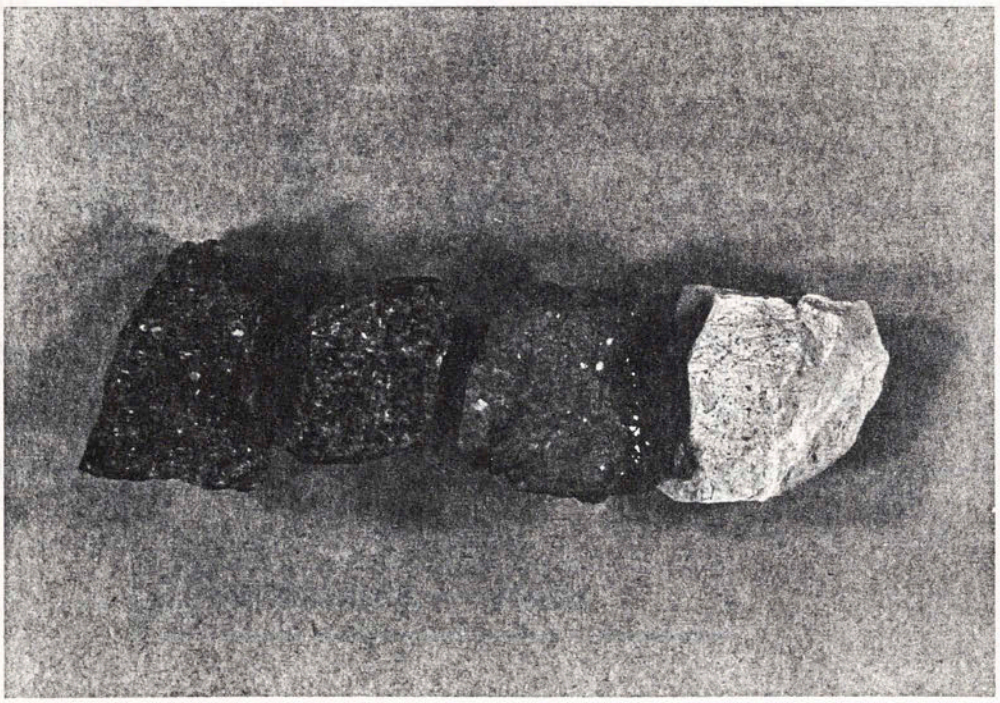

Figure 28. Graded bedding in hand samples. Photo (a) is a Mud Creek sample (T-73) with vertical differential settling of the feldspar phenocrysts. Photo (b) shows 4 of the Beavers Bend samples (T-60a, T-60b, T-60d and T-60e) which show differential settling of feldspar phenocrysts towards the base (T-60a) with increasing amounts of pseudomorphic glass material upwards (present as clay in T-60e).

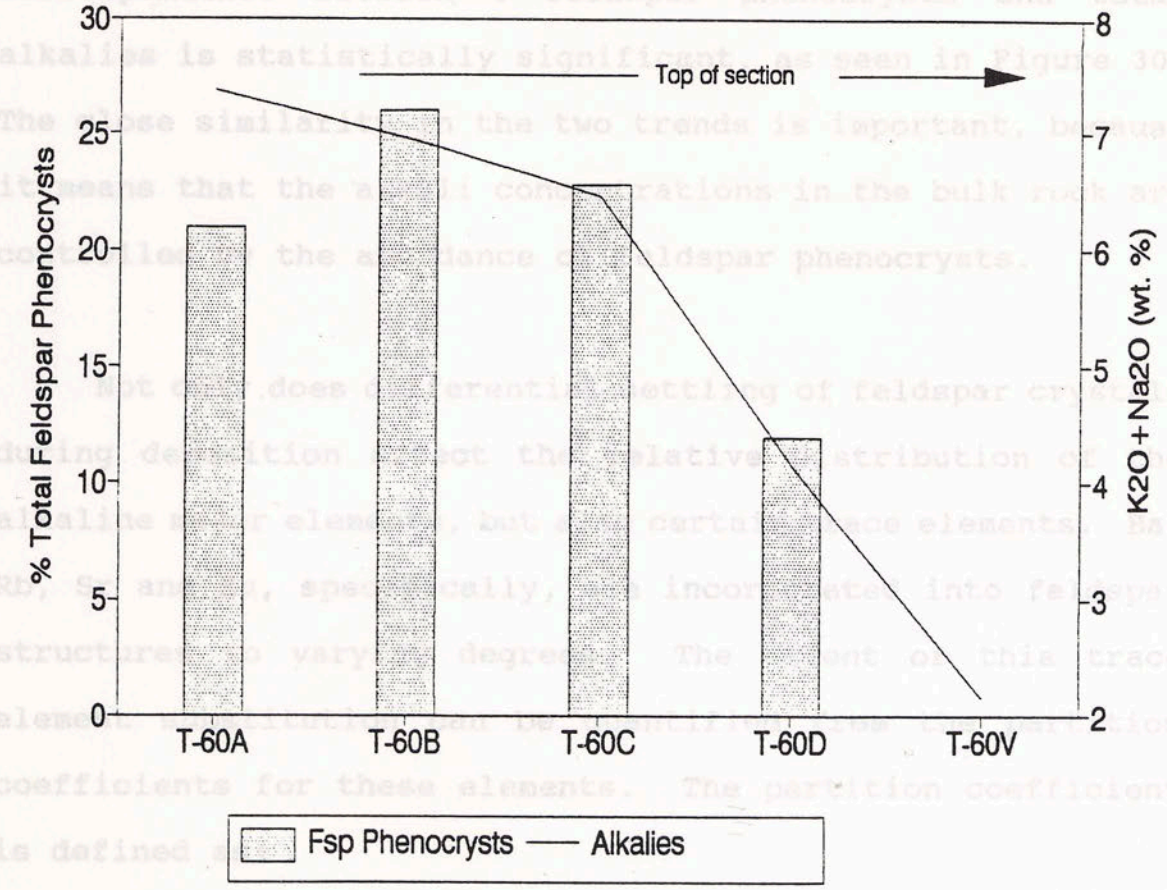

Figure 29. Total amount of feldspar phenocrysts in the T-60 sequence compared with whole rock Na and K abundances.

alkali element abundances are compared because the alkali feldspar is not pure K-feldspar, as evidenced by the patchy perthitic texture. There is a strong similarity in the two trends up the stratigraphic section; upwards decreases/increases in % feldspar phenocrysts are generally matched by upward decreases/increases in alkalies. The correspondence between % feldspar phenocrysts and total alkalies is statistically significant, as seen in Figure 30. The close similarity in the two trends is important, because it means that the alkali concentrations in the bulk rock are controlled by the abundance of feldspar phenocrysts.

Not only does differential settling of feldspar crystals during deposition affect the relative distribution of the alkaline major elements, but also certain trace elements. Ba, Rb, Sr and Eu, specifically, are incorporated into feldspar structures to varying degrees. The extent of this trace element substitution can be quantified from the partition coefficients for these elements. The partition coefficient is defined as:

$$K_d = \frac{\text{concentration of element in mineral}}{\text{concentration of element in liquid}}$$

The partition coefficient, K_d, can be determined for every

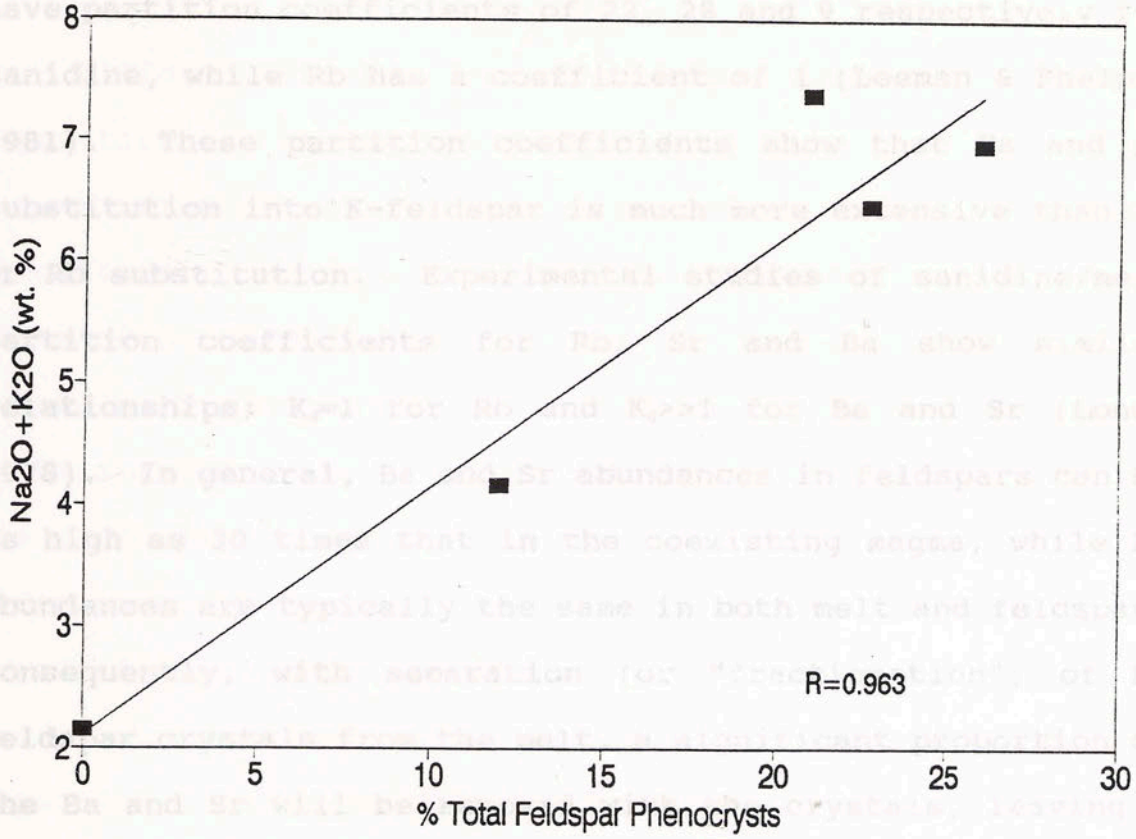

Figure 30. Linear regression between total alkalies and total feldspar phenocrysts.

trace element for any given mineral. Partition coefficients have been calculated for Ba, Sr and Eu in sanidine by ratioing element concentrations in sanidine with concentrations in the surrounding glass matrix (coexisting melt) (Long, 1978; Leeman & Phelps, 1981; Mahood & Hildreth, 1983). In high-silica rhyolites from the Yellowstone volcanic field, Ba, Sr and Eu have partition coefficients of 22, 28 and 9 respectively for sanidine, while Rb has a coefficient of 1 (Leeman & Phelps, 1981). These partition coefficients show that Ba and Sr substitution into K-feldspar is much more extensive than Eu or Rb substitution. Experimental studies of sanidine/melt partition coefficients for Rb, Sr and Ba show similar relationships; $K_d=1$ for Rb and $K_d>>1$ for Ba and Sr (Long, 1978). In general, Ba and Sr abundances in feldspars can be as high as 30 times that in the coexisting magma, while Rb abundances are typically the same in both melt and feldspar. Consequently, with separation (or "fractionation") of K-feldspar crystals from the melt, a significant proportion of the Ba and Sr will be removed with the crystals, leaving a residual melt that is depleted in Ba and Sr. With a partition coefficient of 1, the amount of Rb in the melt will not be affected by the removal of K-feldspar. The magnitude of the relative depletion in Ba and Sr is a function of the value of K_d and the percentage of feldspar crystals removed from the system. In igneous terms, fractionation of K-feldspar will

fractionate Ba and Sr (and Eu), resulting in a depleted residual melt, and will not fractionate Rb. It should also be noted that in the case of trace elements, where $K_d << 1$ for K-feldspar (or any crystal phase), removal of the K-feldspar results in a relative enrichment of that element in the residual melt.

Differential settling of feldspar phenocrysts during deposition, to create the fining-upwards tuff units, serves to mechanically fractionate some of the trace elements. Specifically, the trace elements which reside in feldspar are affected by differential settling of crystals in the same manner as the alkalies. Figures 31 and 32 compare the trends of Ba and K-feldspar, and Sr and plagioclase phenocrysts in the T-60 Beavers Bend sequence. Ba matches the relative decreases of K-feldspar in both sequences and Sr matches the trend of plagioclase phenocrysts. The relationships between trace elements and their feldspar host is statistically significant, with R=0.957 for Ba and K-feldspar and R=0.951 for Sr and plagioclase (Figures 33 and 34). Clearly, whole rock compositions in the tuffs are affected by the mechanical segregation of feldspar crystals from the smaller crystals and glass shards, so that samples collected from different portions of one eruptive unit do not represent the bulk chemistry of that tuff.

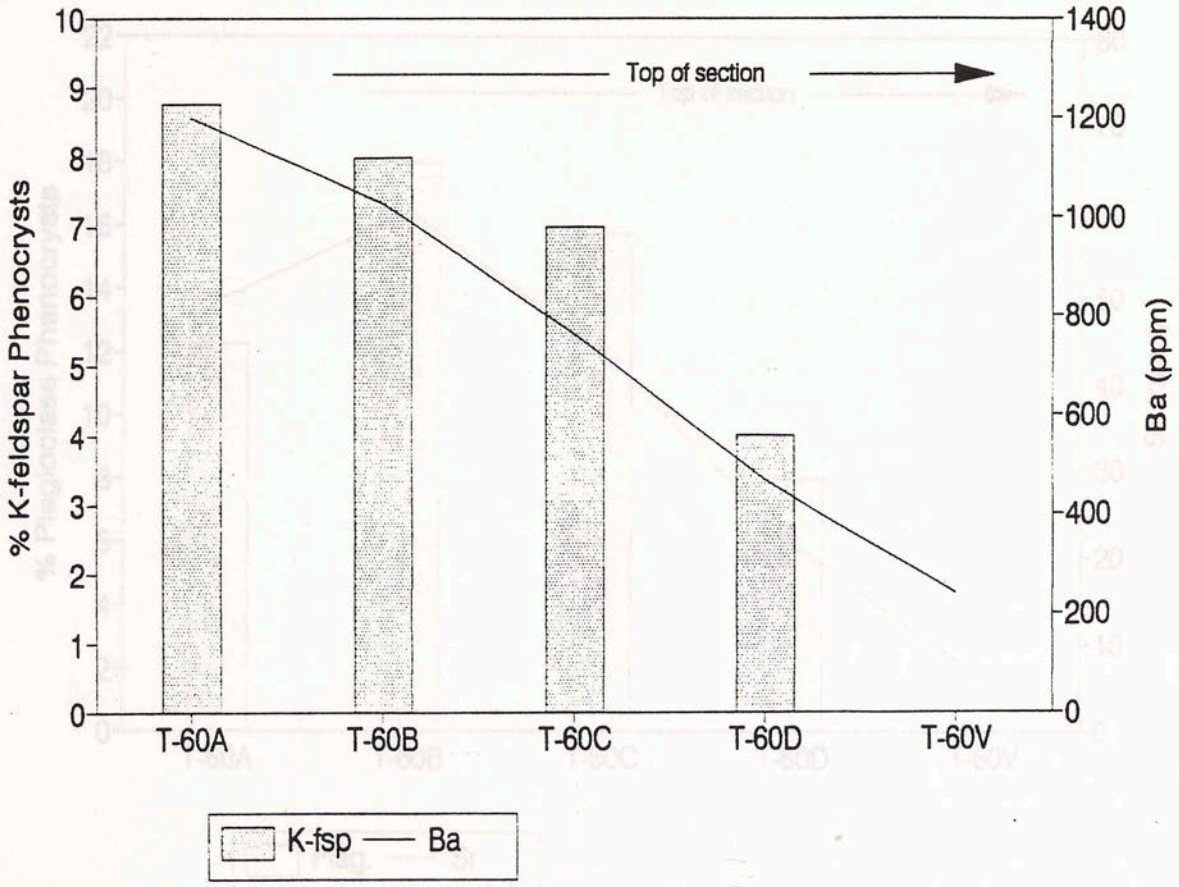

Figure 31. Ba abundances compared to total K-feldspar phenocrysts in samples from the T-60 sequence.

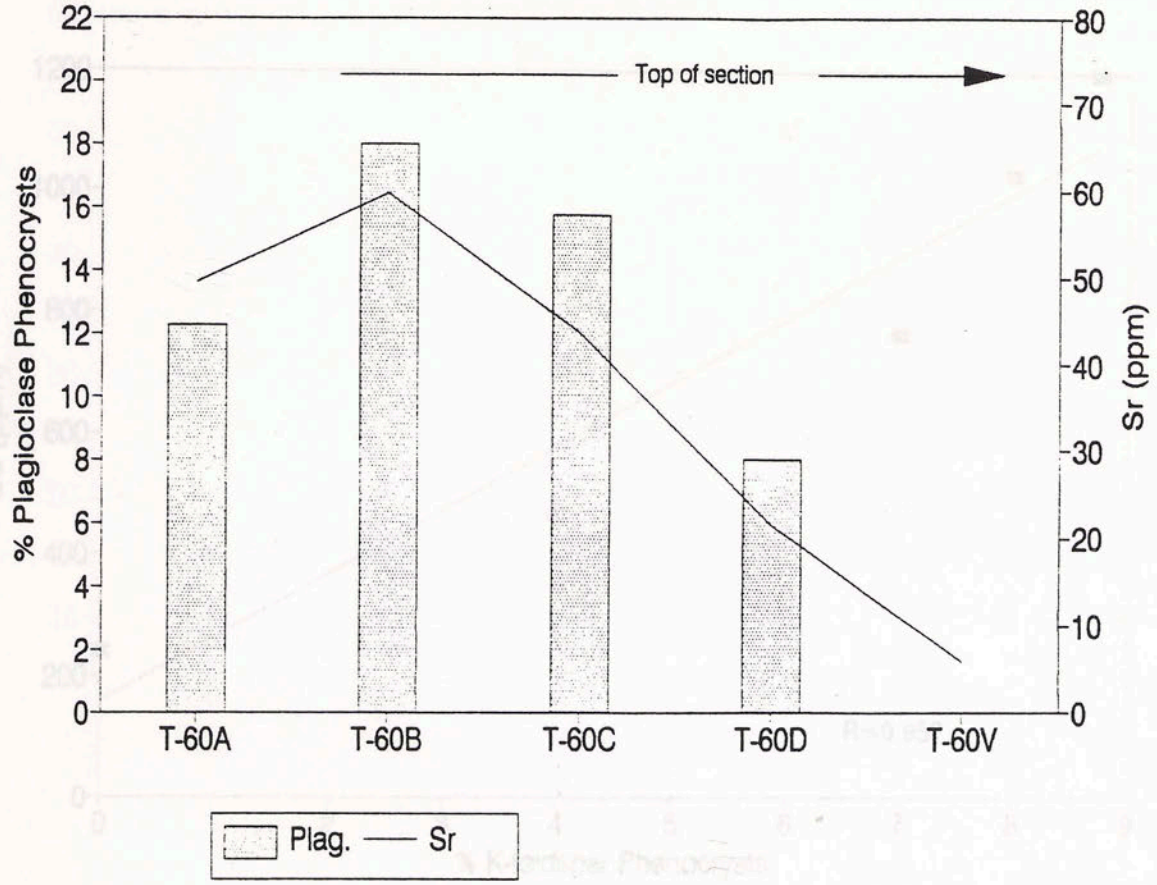

Figure 32. Sr abundances versus total plagioclase phenocrysts, T-60 sequence.

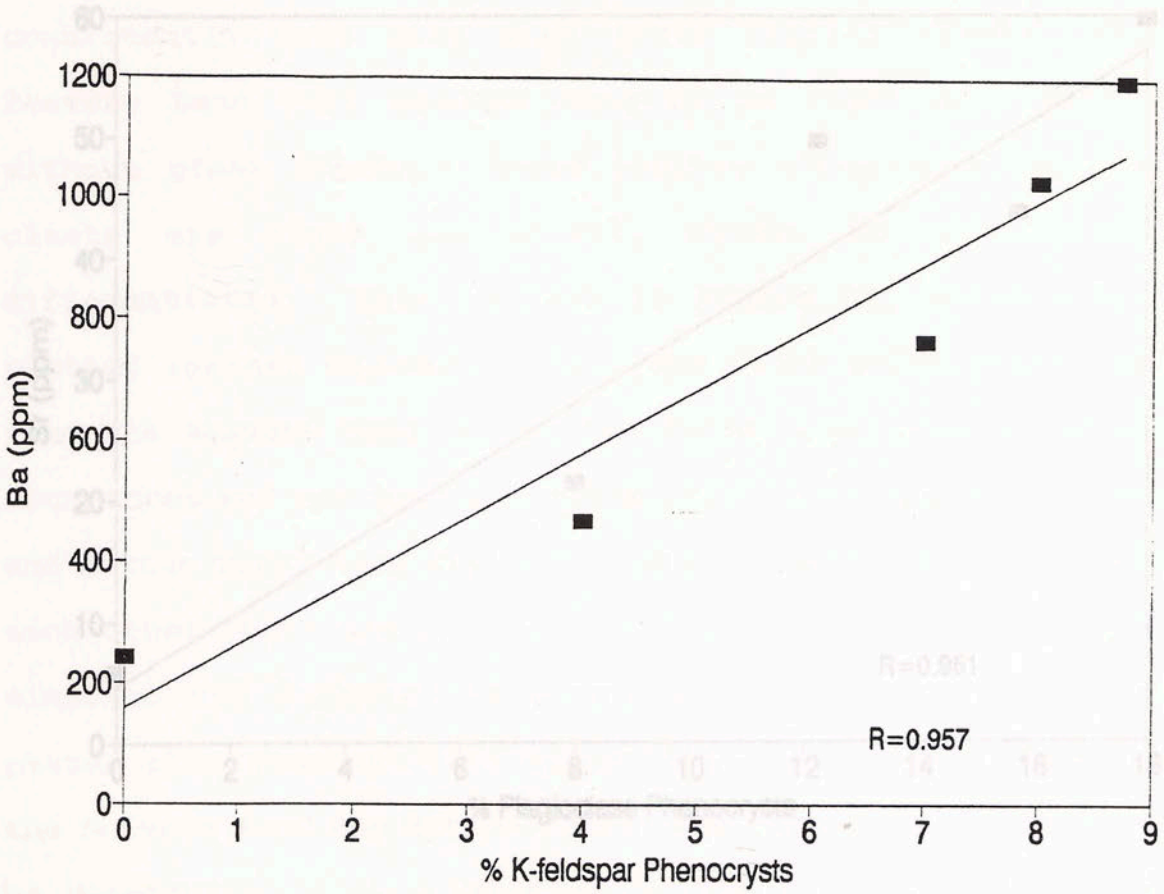

Figure 33. Linear regression between Ba and total K-feldspar phenocrysts.

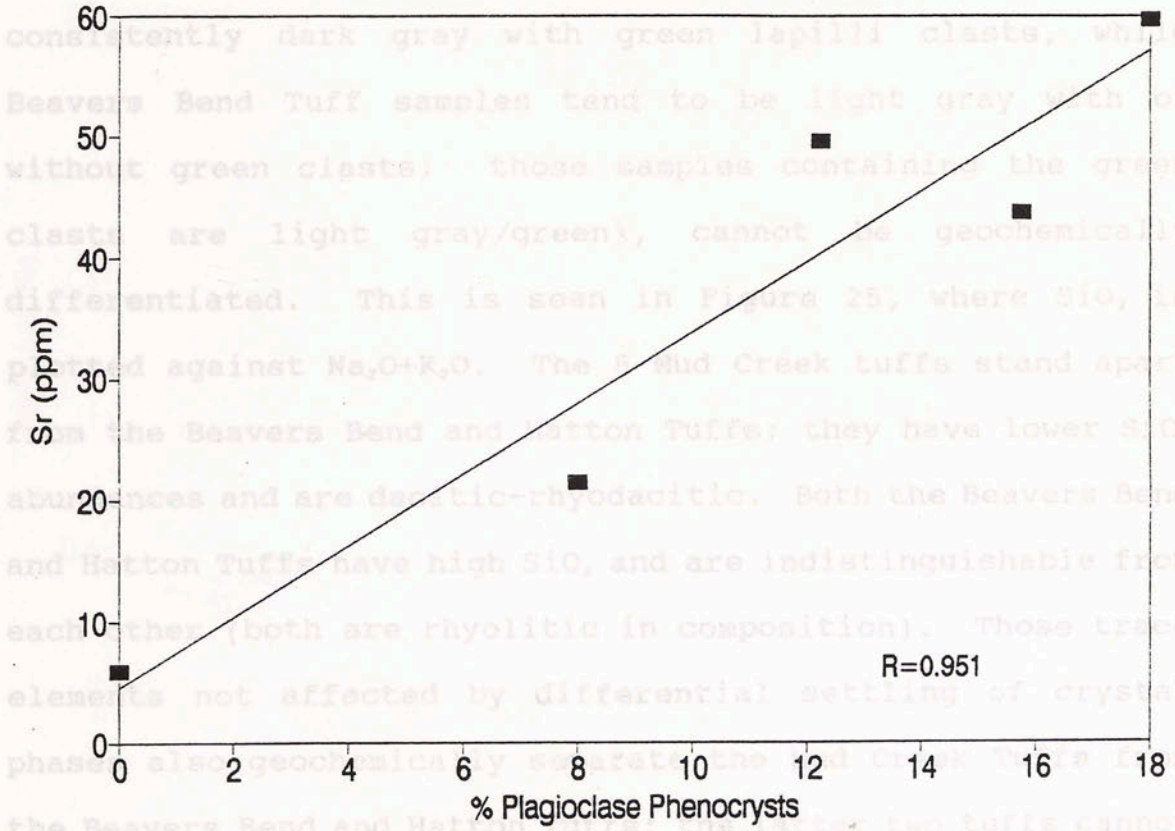

Figure 34. Linear regression between Sr and total plagioclase phenocrysts.

The effect of differential settling on whole rock geochemistry can be minimized if the geochemistry of all tuff samples is considered collectively. This approach is justified because the Beavers Bend Tuff and Hatton Tuff (all but 8 of the total collection of tuff samples), while distinguishable in hand samples (Hatton Tuff samples are consistently dark gray with green lapilli clasts, while Beavers Bend Tuff samples tend to be light gray with or without green clasts; those samples containing the green clasts are light gray/green), cannot be geochemically differentiated. This is seen in Figure 25, where SiO_2 is plotted against Na_2O+K_2O. The 8 Mud Creek tuffs stand apart from the Beavers Bend and Hatton Tuffs; they have lower SiO_2 abundances and are dacitic-rhyodacitic. Both the Beavers Bend and Hatton Tuffs have high SiO_2 and are indistinguishable from each other (both are rhyolitic in composition). Those trace elements not affected by differential settling of crystal phases also geochemically separate the Mud Creek Tuffs from the Beavers Bend and Hatton Tuffs; the latter two tuffs cannot be geochemically discriminated by trace element abundances. Figures 35 and 36 are typical of the geochemical relationships found between the various Stanley tuffs; the Mud Creek tuffs geochemically stand apart from the Beavers Bend and Hatton Tuffs. Collective consideration of the Beavers Bend and Hatton Tuff compositions serves to "homogenize" the

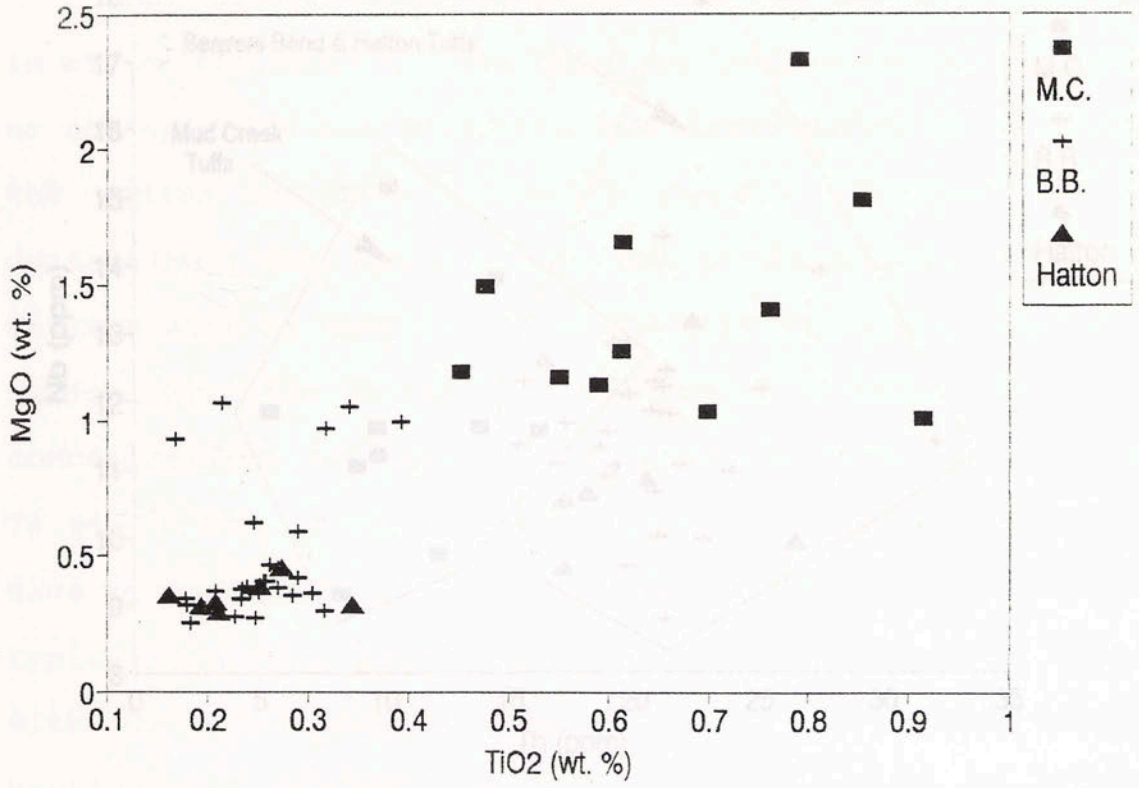

Figure 35. Ti versus Mg, shows how the Mud Creek tuffs plot as a separate group from the bulk of the Beavers Bend and Hatton Tuff samples. M.C.= Mud Creek Tuffs, B.B.= Beavers Bend Tuffs.

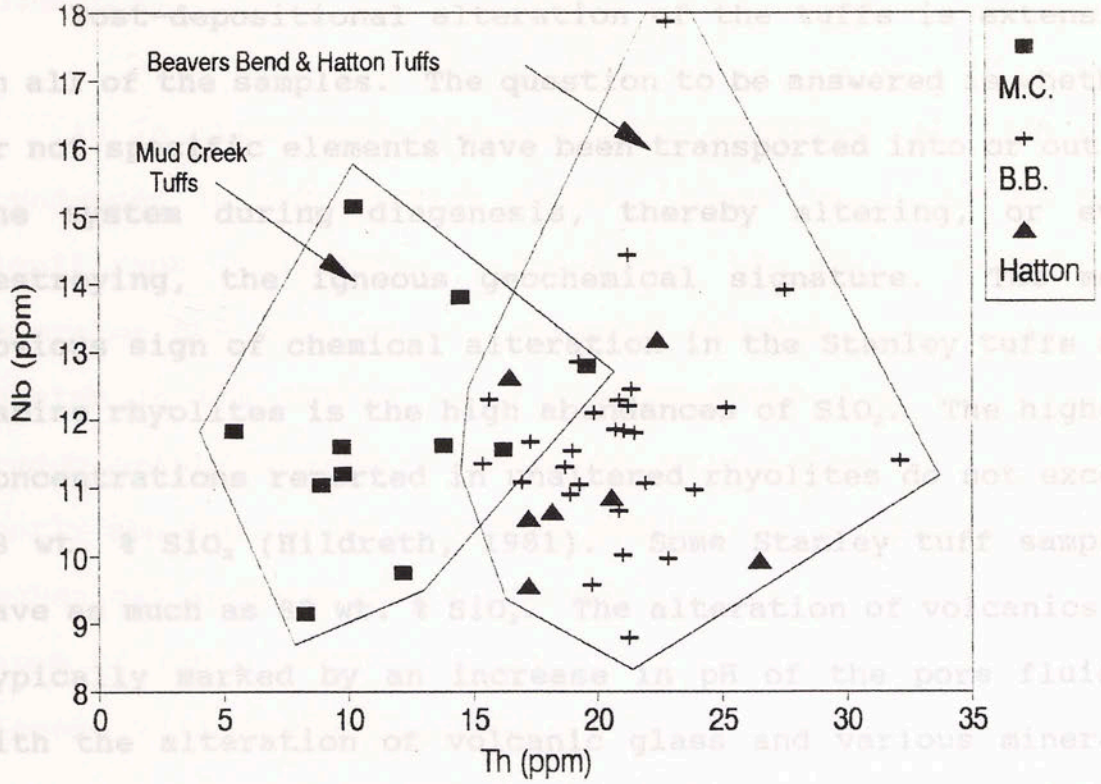

Figure 36. A plot of Th against Nb serves to geochemically differentiate the Mud Creek Tuffs from both the Beavers Bend and Hatton Tuffs. M.C.= Mud Creek Tuffs, B.B.= Beavers Bend Tuffs.

compositional variability caused by differential settling during deposition. The resolution of the igneous geochemical signature is thereby improved, allowing the geochemical tectofacies of the tuffs to be discerned.

Diagenesis

Post-depositional alteration of the tuffs is extensive in all of the samples. The question to be answered is whether or not specific elements have been transported into or out of the system during diagenesis, thereby altering, or even destroying, the igneous geochemical signature. The most obvious sign of chemical alteration in the Stanley tuffs and Sabine rhyolites is the high abundances of SiO_2. The highest concentrations reported in unaltered rhyolites do not exceed 78 wt. % SiO_2 (Hildreth, 1981). Some Stanley tuff samples have as much as 82 wt. % SiO_2. The alteration of volcanics is typically marked by an increase in pH of the pore fluids. With the alteration of volcanic glass and various minerals particularly susceptible to alteration (such as biotite, amphiboles etc.), enough alkalies are released into solution so that the pH increases to basic levels -- up to pH=9 (Walton, 1975; Forsman, 1986). With high silica activity in basic solutions, it is conceivable that some of the silica could have been exported from localized areas within a tuff unit and then transported and precipitated in other localized areas within the same unit, producing isolated zones which

have higher or lower SiO_2 values relative to the average whole rock SiO_2 concentration. In this case, a tuff unit qualifies as a closed system. If the tuff layers are open systems, then it is probable that the removal of certain mobile elements from the tuff layers produced the observed increase in SiO_2 abundances.

It is clear that diagenesis has modified the elemental abundances in the Stanley tuffs. Given the occurrence of significant diagenetic alteration, it is important to determine how much of the original igneous signature still remains in the tuffs; are the geochemical signatures still predominantly igneous in character, or are they now reflecting mostly the cumulative effect of weathering, diagenesis and/or mechanical segregation of grains? Figure 37 illustrates the range of ionic potentials for the elements of interest. An element with an ionic potential less than 3 will be highly mobile in aqueous solutions (Goldschmidt, 1934). Plots of mobile elements against immobile elements indicate whether diagenesis acted as a mechanism whereby elements were separated from each other (or fractionated). Figure 38 is a plot of Sr against total Fe (which, due to sample preparation techniques, is now entirely Fe^{+3}, and is therefore represented as Fe_2O_3). The correlation coefficient of the linear regression is 0.826, significant at greater than the 99%

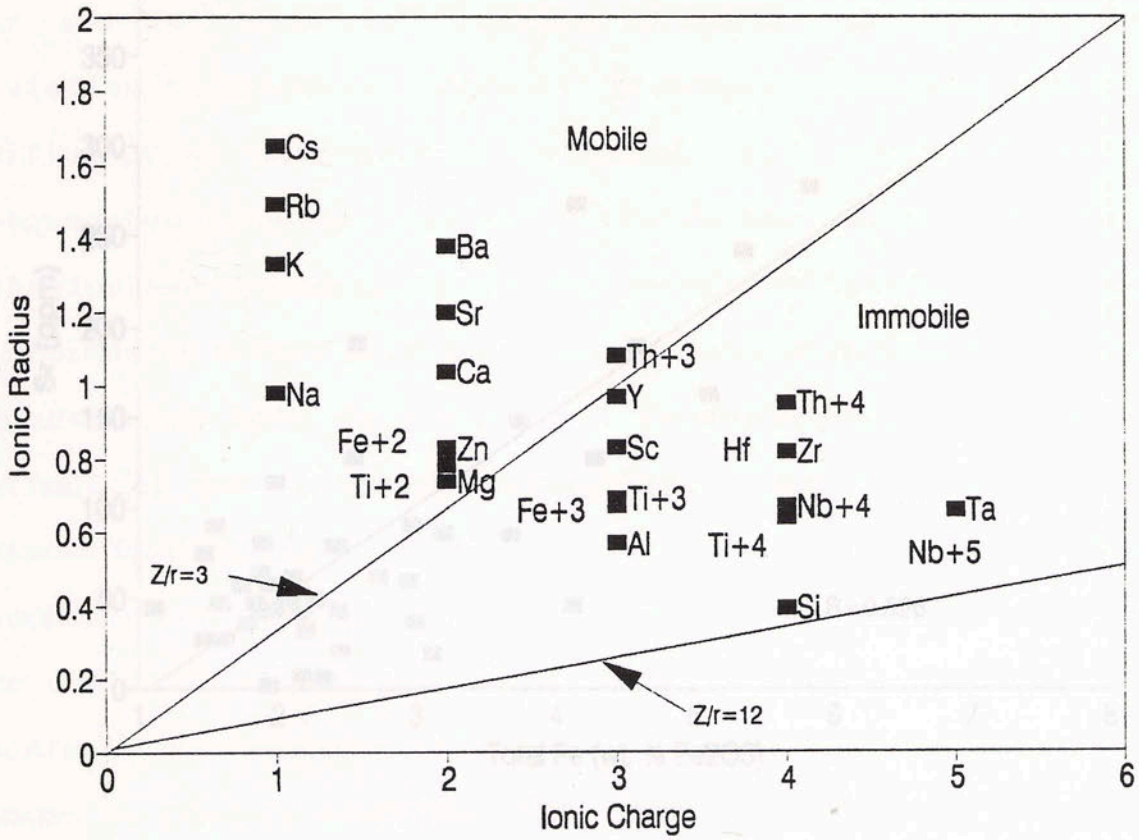

Figure 37. Ionic potentials (ionic charge, Z, over ionic radius, r) of elements important in the Ouachita Mountain tuffs.

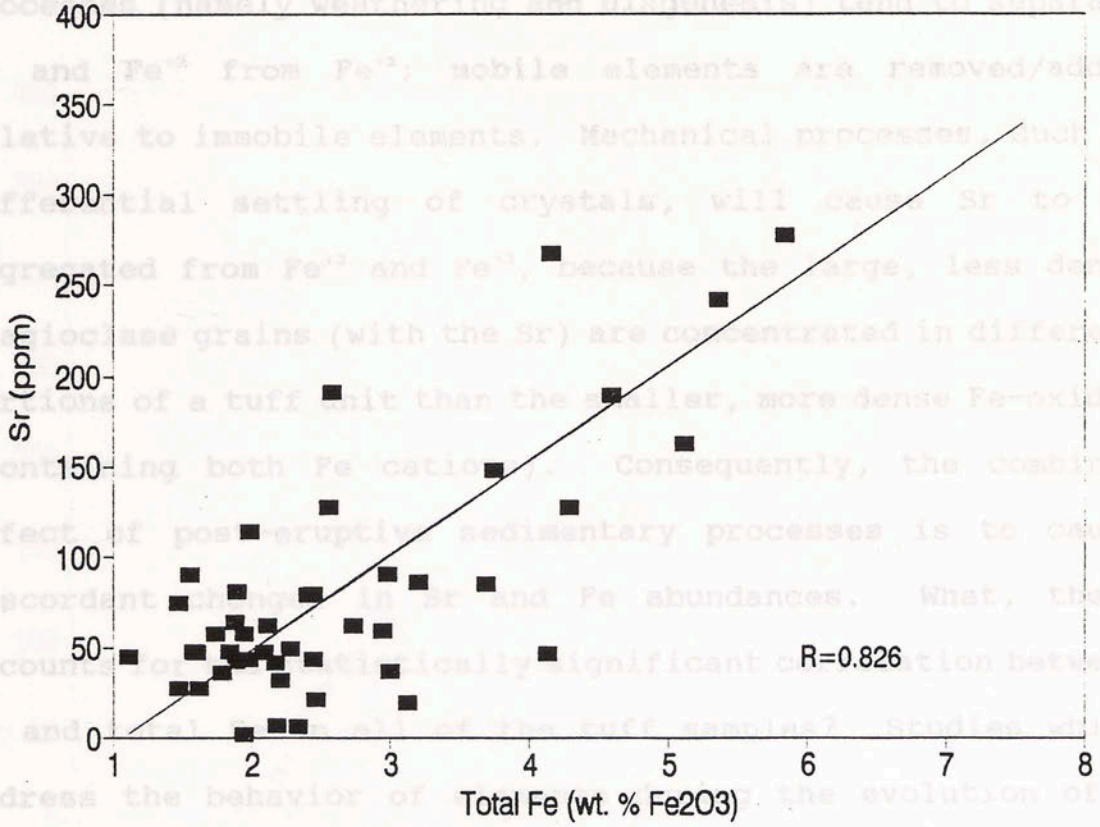

Figure 38. Sr against total Fe for all of the Stanley tuff samples. Linear regression yields a correlation coefficient of 0.826.

confidence level. Apart from their igneous source and igneous components, the tuffs are essentially sedimentary rocks. In sedimentary systems, the three ions, Sr^{+2}, Fe^{+2} and Fe^{+3}, are fractionated relative to each other. Sr has an ionic potential of 1.27; Fe^{+2}, 2.27; and Fe^{+3}, 4.48. Chemical processes (namely weathering and diagenesis) tend to separate Sr and Fe^{+2} from Fe^{+3}; mobile elements are removed/added relative to immobile elements. Mechanical processes, such as differential settling of crystals, will cause Sr to be segregated from Fe^{+2} and Fe^{+3}, because the large, less dense plagioclase grains (with the Sr) are concentrated in different portions of a tuff unit than the smaller, more dense Fe-oxides (containing both Fe cations). Consequently, the combined effect of post-eruptive sedimentary processes is to cause discordant changes in Sr and Fe abundances. What, then, accounts for the statistically significant correlation between Sr and total Fe in all of the tuff samples? Studies which address the behavior of elements during the evolution of a magma to produce higher-silica rhyolites and tuffs show that Sr and Fe behave in a similar manner. Igneous processes (namely crystal fractionation and/or convection-controlled diffusion within the magma chamber) which generate higher-silica magmas tend to collectively exclude both Sr and Fe from increasingly evolved melts (Hildreth, 1981). Evidence of this igneous relationship between Sr and total Fe is seen in Figure

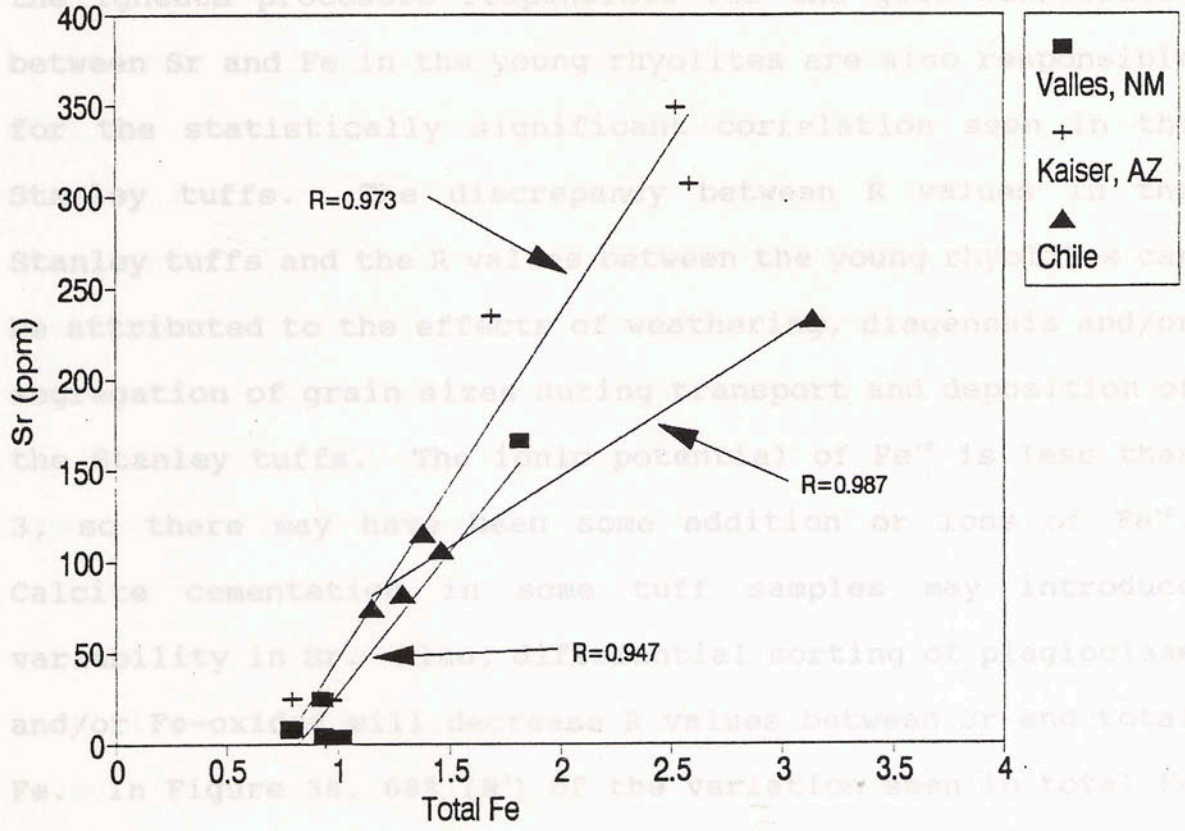

Figure 39. Same plot as Figure 38, only abundances are from three young volcanic suites. Valles Caldera, New Mexico; Kaiser Spring, Arizona; San Pedro-Pellado, Chile.

39, which depicts three different suites of young, unaltered rhyolites (Valles Caldera, N.M., Spell & Kyle, 1989; Kaiser Spring, Arizona, Moyer & Esperanca, 1989; Andes, Chile, Davidson et. al., 1988). Linear regressions between Sr and total Fe concentrations in each of the three data sets yields correlation coefficients of at least 0.94. It follows that the igneous processes responsible for the good correlation between Sr and Fe in the young rhyolites are also responsible for the statistically significant correlation seen in the Stanley tuffs. The discrepancy between R values in the Stanley tuffs and the R values between the young rhyolites can be attributed to the effects of weathering, diagenesis and/or segregation of grain sizes during transport and deposition of the Stanley tuffs. The ionic potential of Fe^{+2} is less than 3, so there may have been some addition or loss of Fe^{+2}. Calcite cementation in some tuff samples may introduce variability in Sr. Also, differential sorting of plagioclase and/or Fe-oxides will decrease R values between Sr and total Fe. In Figure 38, 68% (R^2) of the variation seen in total Fe can be attributed to its dependence on Sr. The interdependence between Sr and Fe results from their similar behavior in the magma prior to eruption, deposition and diagenesis. 32% of the variation in Fe relative to Sr is due to processes where Sr and Fe do not behave in a similar manner; weathering, diagenesis and differential settling of

crystals are probably all partially responsible for the discrepancy between R values for the Stanley tuffs and the younger rhyolites.

A plot of Sr against TiO_2 (Figure 40) also shows a statistical correlation between a mobile element and an immobile element (R=0.807, significant at greater than the 99% confidence level). Like Fe and Sr, Ti and Sr behave in a similar manner in igneous systems (Figure 41), with correlation coefficients exceeding 0.99. Weathering and diagenesis, if extensive, will destroy the igneous geochemical relationship. Differential settling of plagioclase and Fe-Ti oxides will also destroy the igneous geochemical relationship. The discrepancy between the R values of the 3 suites of young rhyolites and the R value of the Stanley tuffs can be attributed to the combined effects of weathering, diagenesis and differential sorting of crystal phases. It is notable that Ti and Sr have a higher correlation coefficient in the young rhyolites than total Fe and Sr, while total Fe and Sr have the higher correlation coefficient in the Stanley tuffs. Given the fact that some portion of the total Fe is mobile Fe^{+2}, one would expect there to be an even larger discrepancy between Sr and total Fe than between Sr and Ti. Because there is not, it might be inferred that either most of the total Fe is Fe^{+3}, or that post-eruptive processes did not extensively

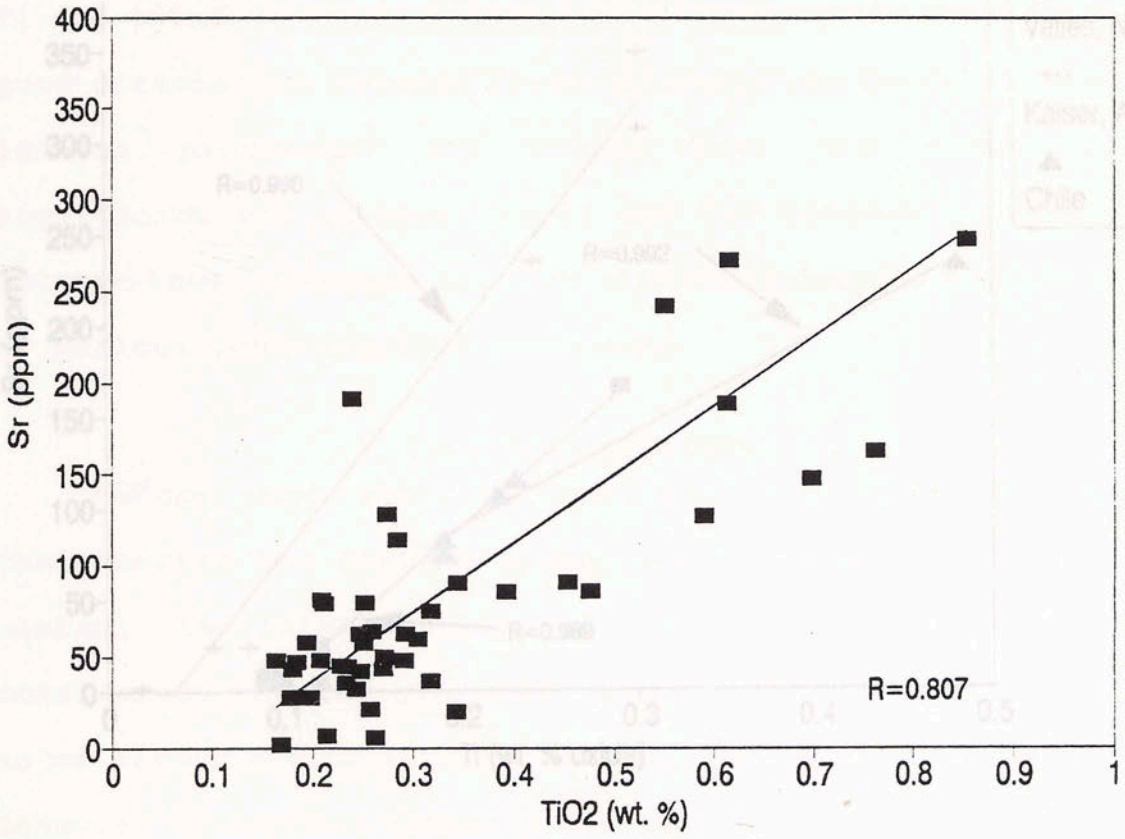

Figure 40. Sr compared to Ti abundances with a linear regression yielding an R value of 0.807.

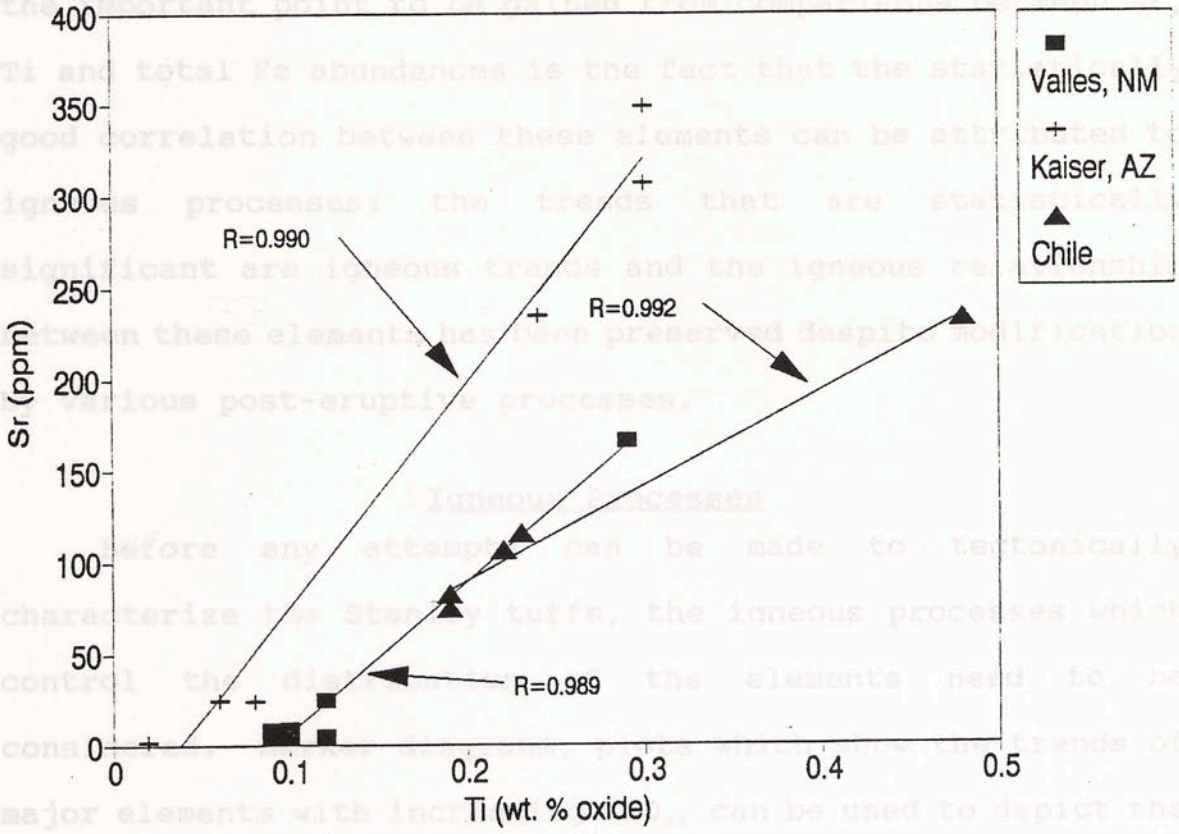

Figure 41. Sr versus Ti in the same three volcanic suites as those depicted in Figure 39.

cause Sr, Fe^{+2} and Fe^{+3} to be segregated from each other.

One can only speculate as to which of the three post-eruptive processes are largely responsible for modification of the original igneous geochemical signatures. Nevertheless, the important point to be gained from comparisons between Sr, Ti and total Fe abundances is the fact that the statistically good correlation between these elements can be attributed to igneous processes; the trends that are statistically significant are igneous trends and the igneous relationship between these elements has been preserved despite modification by various post-eruptive processes.

Igneous Processes

Before any attempts can be made to tectonically characterize the Stanley tuffs, the igneous processes which control the distribution of the elements need to be considered. Harker diagrams, plots which show the trends of major elements with increasing SiO_2, can be used to depict the behavior of various elements during differentiation of a melt to form high-SiO_2 volcanics. In the Stanley tuffs, comparison of all of the elements with SiO_2 (Table 10a) shows that with the exception of Th, Yb and Lu, all the statistically significant relationships involve elements that decrease with increasing SiO_2 (Figures 42, 43). Those elements which have a statistically significant correlation with SiO2 (Ti, Al, Fe,

TABLE 10. Correlation Coefficients, Elements versus SiO_2

Part A.	Element	R value
	XRF	
	Ti	**-0.761**
	Al	**-0.829**
	Fe	**-0.889**
	Mg	**-0.734**
	Ca	**-0.660**
	Na	-0.286
	K	+0.052
	P	**-0.848**
	Nb	-0.157
	Zr	**-0.737**
	Y	+0.187
	Sr	**-0.846**
	Rb	+0.195
	Th	**+0.553**
	Pb	-0.010
	Zn	**-0.716**
	Sc	**-0.828**
	Ba	**-0.554**
	INAA	
	La	+0.083
	Ce	+0.017
	Nd	+0.083
	Sm	+0.167
	Eu	**-0.764**
	Tb	+0.337
	Yb	**+0.406**
	Lu	**+0.383**
	Ta	+0.212
	Hf	**-0.399**
	Co	**-0.703**
	Cr	**-0.587**
	Sc	**-0.612**

degrees of freedom = 46
99% confidence level = 0.372
95% confidence level = 0.288

Table 10. cont.

Part B.	Mud Creek	Beavers Bend	Hatton
degrees of freedom:	8	26	5
Rb	+0.443	**-0.524**	-0.739
Y	-0.061	-0.272	-0.501
Nb	+0.262	**-0.438**	**-0.797**
Pb	-0.111	-0.344	**-0.911**
Na	**-0.809**	-0.109	-0.602
K	+0.411	**-0.557**	-0.722
99% level:	0.765	0.478	0.874
95% level:	0.632	0.374	0.754

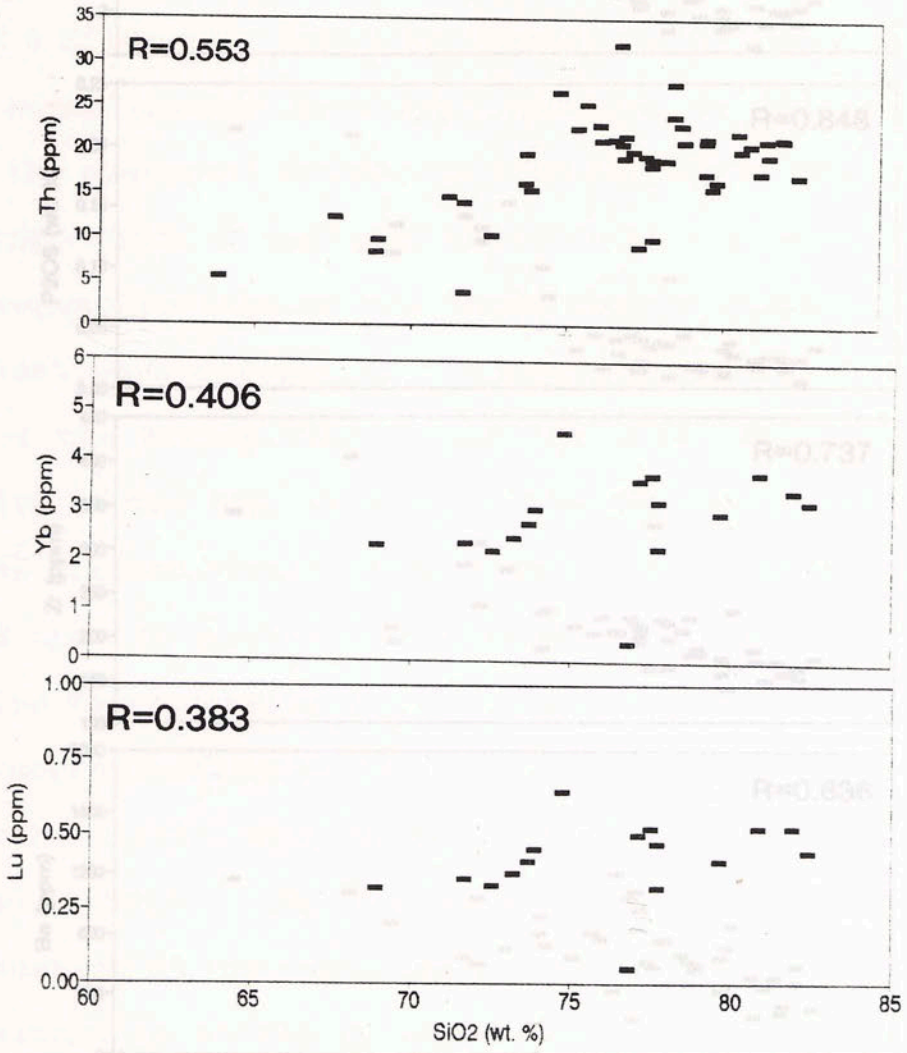

Figure 42. Trace element and rare earth elements which systematically increase with increasing silica.

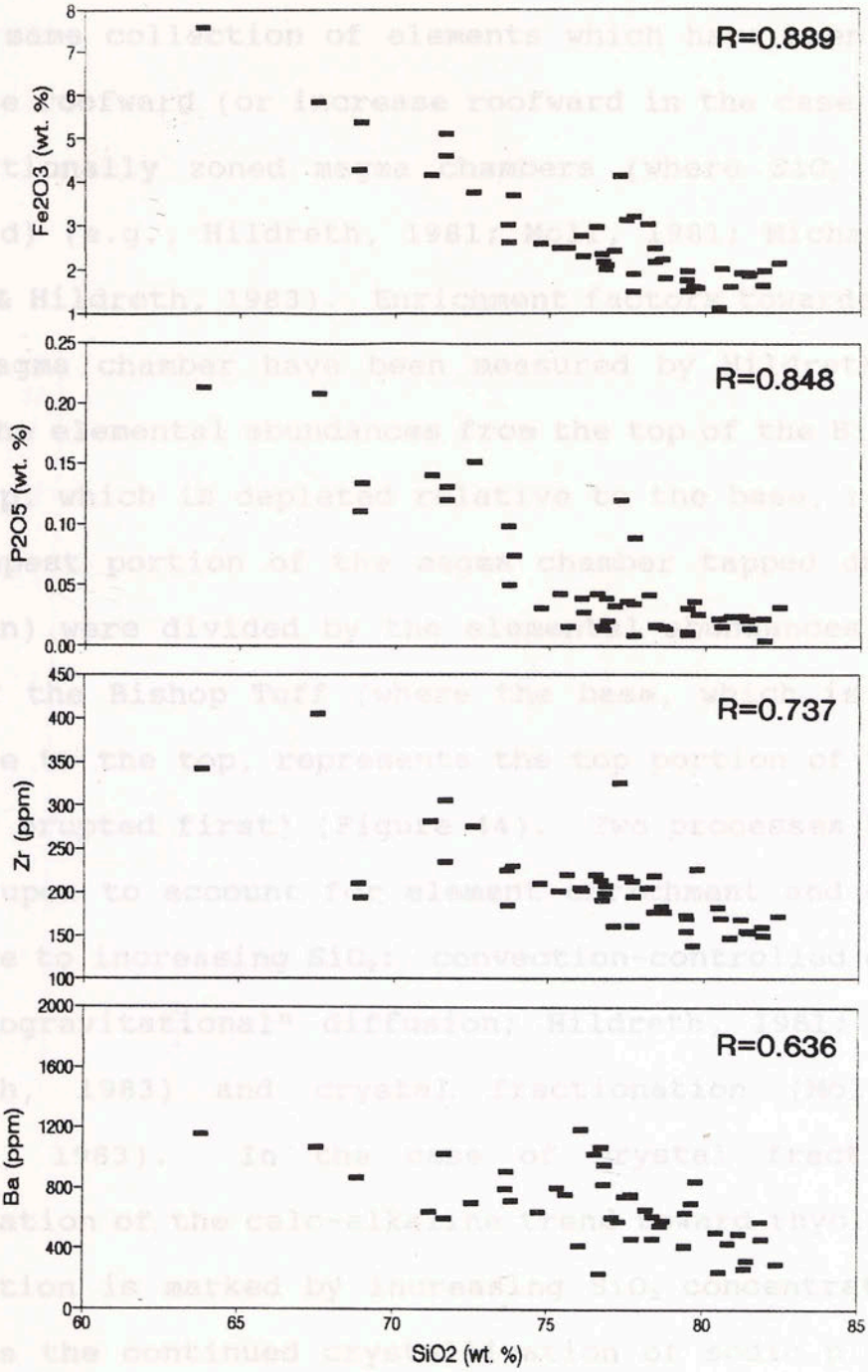

Figure 43. Major and trace elements which systematically decrease with increasing silica.

Mg, Ca, P, Zr, Sr, Zn, Sc, Ba, Eu, Co, Cr, and Th) are part of the same collection of elements which have been found to decrease roofward (or increase roofward in the case of Th) in compositionally zoned magma chambers (where SiO_2 increases roofward) (e.g., Hildreth, 1981; Moll, 1981; Michael, 1983; Mahood & Hildreth, 1983). Enrichment factors towards the roof of a magma chamber have been measured by Hildreth (1981), where the elemental abundances from the top of the Bishop Tuff (the top, which is depleted relative to the base, represents the deepest portion of the magma chamber tapped during the eruption) were divided by the elemental abundances from the base of the Bishop Tuff (where the base, which is enriched relative to the top, represents the top portion of the magma chamber erupted first) (Figure 44). Two processes have been called upon to account for element enrichment and depletion relative to increasing SiO_2: convection-controlled diffusion ("thermogravitational" diffusion; Hildreth, 1981; Mahood & Hildreth, 1983) and crystal fractionation (Moll, 1981; Michael, 1983). In the case of crystal fractionation, continuation of the calc-alkaline trend toward rhyolitic melt composition is marked by increasing SiO_2 concentrations and involves the continued crystallization of sodic plagioclase + K-feldspar + Fe-Ti oxides + apatite $\pm$ zircon $\pm$ amphiboles $\pm$ biotite. Because these mineral phases contain Ba, Sr, Fe, Ti, P, and Zr, the residual melt is increasingly depleted in

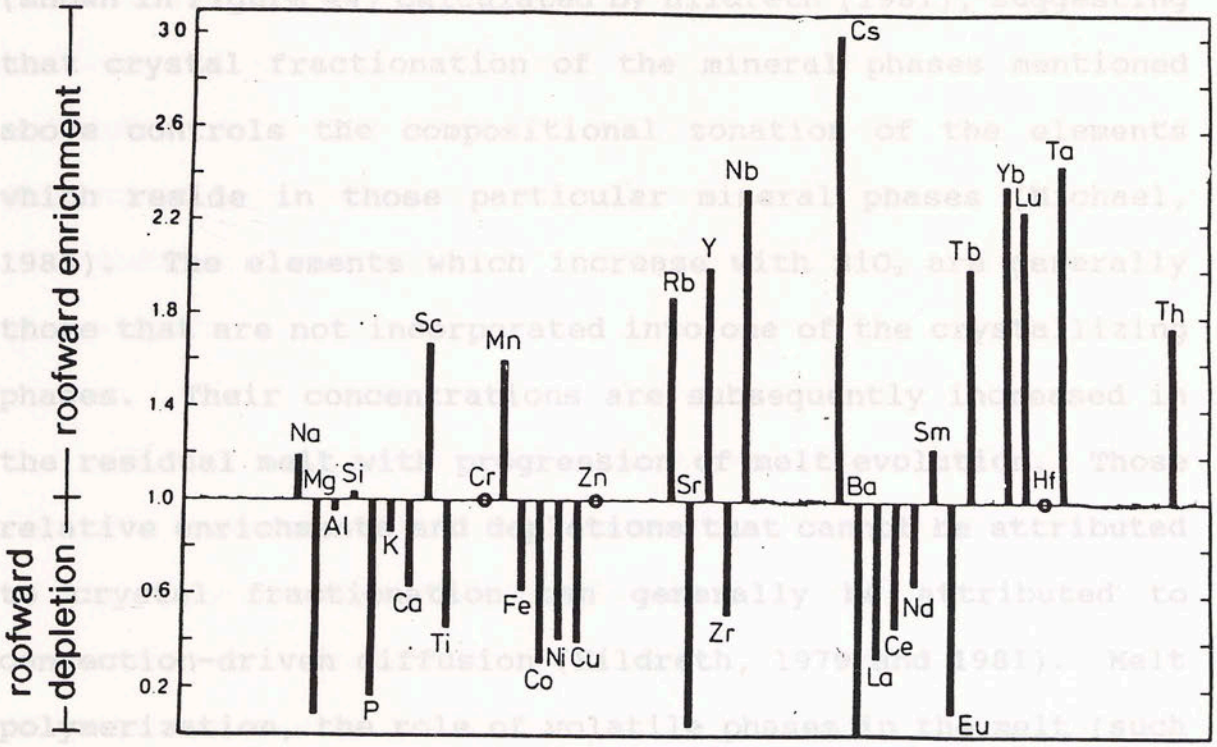

Figure 44. Enrichment factors towards the roof of a compositionally zoned magma chamber (after Hildreth, 1981).

these elements if the mineral phases are removed from the melt by gravitational settling. This is reflected in Figure 44, where Ba, Sr, Fe, Ti, P and Zr all have ratios less than one. Michael (1983) has demonstrated that mineralogy correlates with chemical gradients. Specifically, crystal-liquid partition coefficients correlate with the enrichment factors (shown in Figure 44) calculated by Hildreth (1981), suggesting that crystal fractionation of the mineral phases mentioned above controls the compositional zonation of the elements which reside in those particular mineral phases (Michael, 1983). The elements which increase with SiO_2 are generally those that are not incorporated into one of the crystallizing phases. Their concentrations are subsequently increased in the residual melt with progression of melt evolution. Those relative enrichments and depletions that cannot be attributed to crystal fractionation can generally be attributed to convection-driven diffusion (Hildreth, 1979 and 1981). Melt polymerization, the role of volatile phases in the melt (such as H_2O, F, Cl), and thermal gradients are some of the phenomena included in convection-driven diffusion model (Hildreth, 1979).

One additional post-eruptive process should be added to these two igneous processes, and that is differential settling of erupted material during deposition. The mechanical

segregation of crystals and glass shards in the Stanley tuffs during deposition can produce results similar to those produced by crystal fractionation in the magma chamber. In the Stanley tuffs, plagioclase, K-feldspar, and minor accessory mineral phases (e.g., Fe-Ti minerals, zircon, apatite) are segregated from the melt/glass phases by both crystal fractionation in the silicic melt and differential settling of crystal and glass during deposition. A sample collected from the base of a tuff unit has most of the phenocrysts and very little glass, while a sample from the top of a tuff unit contains most of the vitric material minus the phenocrysts.

As previously mentioned, the same elements that have been shown in various studies to undergo depletion towards the roof of the magma chamber (as depicted in Figure 44) decrease with increasing SiO_2 in the Stanley tuffs. This means that one of the three process mentioned above is responsible for the elemental trends with increasing SiO_2. It is not important to know which specific process (or combination of processes) was responsible for the Harker diagram trends since the end result is the same. The important point is that the relative depletion in Fe, Mg, Ca, Ti, P, Zr, Ba, Zn, Sr and Eu is the result of processes inherent in all rhyolitic flows and tuffs. Because rhyolites and tuffs are associated with all types of

tectonic environments, occurrence of these major and trace element enrichments and depletions is independent of tectonic setting.

The above discussion of some of the tectonically-independent processes which control the distribution of elements provides a basis upon which to assess tectonically-dependent processes. High-silica rhyolites and tuffs are constrained to certain types of tectonic environments. Magmatic arcs formed at subduction zones (both oceanic and continental island-arcs) and within-plate extension zones, such as continental rift zones and back-arc basins, are the principal tectonic settings where rhyolitic volcanics are produced. Apart from oceanic island-arcs, all of these tectonic settings have a continental crust component. Also, all of the tectonic settings involve subduction of oceanic crust, with the exception of continental rift settings. Involvement with either a subduction zone and/or continental crust shows up in the geochemical signatures of magmas. Normally, basalts are the principal volcanic rocks that are studied for the purpose of determining tectonic environment. This is because their petrogenetic history is not as complicated as that of higher-silica volcanics (those volcanics which evolve from basaltic and basaltic-andesitic melts). In basalts, a subduction and/or continental

geochemical signature can be seen in the trace element and rare earth element geochemistry. If the same geochemical signatures are preserved in the geochemistry of rhyolites and tuffs, then high-silica volcanics can be used to determine the tectonic setting of a suite of volcanics.

Before considering the effect of tectonically-dependent processes (those specifically associated with subduction and interaction with continental crust) on the geochemistry of rhyolites from known tectonic settings, the manner in which whole rock geochemistry is assessed needs to be addressed. The most informative way of depicting the geochemistry of rhyolites is by plotting spiderdiagrams; so called because of the "spidery" appearance of the resulting trace element and rare earth element trends. Spiderdiagrams provide a frame of reference by which a collection of samples can be compared to one particular normalization factor (which is generally an average composition of a specific type of rock). Different normalization factors are used; common igneous normalization factors include chondrite (thought to represent bulk earth), primordial mantle (hypothetical), and mid-ocean ridge basalt (MORB). North American shale composite (NASC), post-Archean Australian shale (PAAS), European Paleozoic shales (ES) are some of the normalization factors used in sedimentary geochemistry. For melts which are derived from the mantle,

the chondrite or primordial mantle composition is used. The resulting spiderdiagrams provide information about the petrogenetic history of a melt (the composition of which is assumed to be similar to that of either the bulk earth or the primordial mantle). For example, taking the trace element abundances of a mid-ocean ridge basalt and dividing them by the trace element abundances of an average chondrite yields a spiderdiagram pattern where relative enrichments and depletions of the trace elements (relative to chondrites) provide information about the different processes which acted upon a rock to ultimately form the MORB. The initial rock that melts to produce the "parent" melt is assumed to have the same composition as the bulk earth before segregation occurred to form the core, mantle and crust. For the consideration of rhyolite petrogenesis, the trace element abundances are normalized to MORB (the MORB composition used is from Pearce, 1983). By dividing the trace element abundances by the MORB composition, the petrogenetic history behind the formation of MORBs, or basaltic melts, is factored out. The resulting relative enrichments and depletions (relative to MORB) in the spiderdiagrams therefore reflect processes acting upon a basaltic melt to produce the rhyolites -- the post-basalt petrogenetic history is the only part considered. It should be noted that a variety of spiderdiagram formats are commonly used in igneous geochemistry, where the order in which

elements are plotted along the X-axis varies. The specific format employed here is the same as that employed by Pearce (1983), in which rare earth and trace elements are ordered by their ionic potential. Elemental mobility therefore decreases from left to right.

Because the petrogenesis of rhyolites and tuffs involves a complicated history of element/mineral fractionation, mixing and fractionation during deposition, no attempts to tectonically differentiate tuffs or rhyolites exist in the literature. Trace element compositions of granites, however, have been studied within the context of tectonic environment (Pearce et al., 1984). Granites from known tectonic environments were geochemically compared to determine which specific trace elements are reflective of tectonic setting. It was found that ocean ridge granites (ORG), volcanic arc granites (VAG), within plate granites (WPG) and collision granites (COLG) could be discriminated using Rb, Nb, Y, Yb and Ta. These particular trace elements were plotted for 600 granite samples; the resulting plots were used to derive trace element discrimination diagrams. There are 4 different discrimination diagrams that can be used to characterize the tectonic setting of granites: 1) Nb versus Y, 2) Ta versus Yb, 3) Rb versus Y+Nb, and 4) Rb versus Yb+Ta. The lines that define tectonic fields, though drawn

empirically, have a theoretical basis that is related to granite petrogenesis (Pearce et. al., 1984).

Before trying to identify the tectonic environment of the Stanley tuffs, the geochemical signatures of tuffs and rhyolites from known tectonic environments need to be characterized. Eight spiderdiagrams of rhyolites and tuffs (Figures 45-52) from various types of known tectonic environments have been chosen from around the world. Table 11 summarizes the locations, tectonic environments of the high-silica volcanics and data sources for these spiderdiagrams. The rhyolites and tuffs from Papua, New Guinea and central Japan are associated with an ocean island-arc. The important features to note in the two sets of spiderdiagrams (Figures 45 and 46) are the following: 1) the elements on the left side of the diagram are more enriched relative to MORB than those elements on the right side (K, Rb, and Th on the left end, specifically), 2) both spiderdiagrams have troughs (pronounced negative anomalies) at P and Ti, 3) Ta and Nb are depleted relative to the two elements on either side, Th and La (not clearly evident in the Japan spiderdiagrams due to the incomplete data sets), and 4) Sr is strongly depleted relative to K, Rb and Th. It should be not all of the data sets used have both Ta and Nb analyses. Ta and Nb (Nb^{+5}) behave in a geochemically similar manner due to

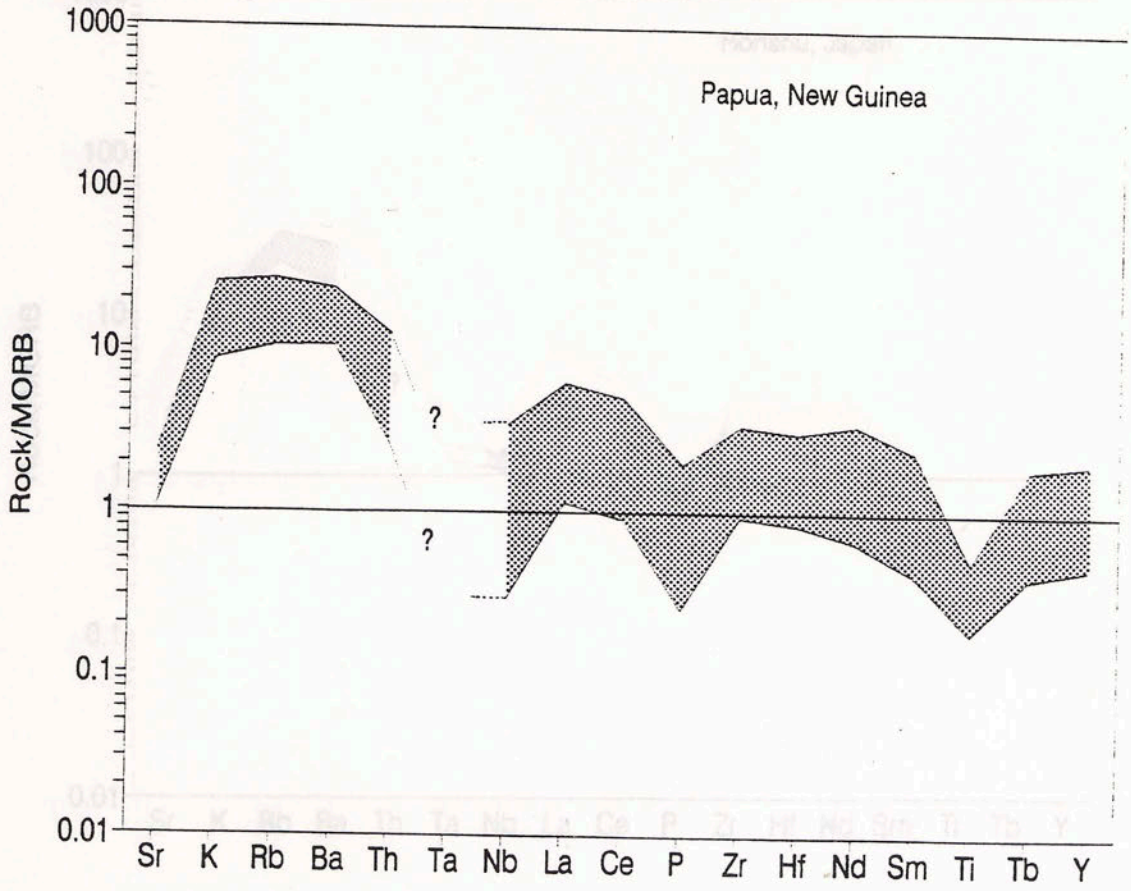

Figure 45. Spiderdiagrams depicting the range of MORB normalized trace and rare earth elements from Papua, New Guinea (see Table 9 for references).

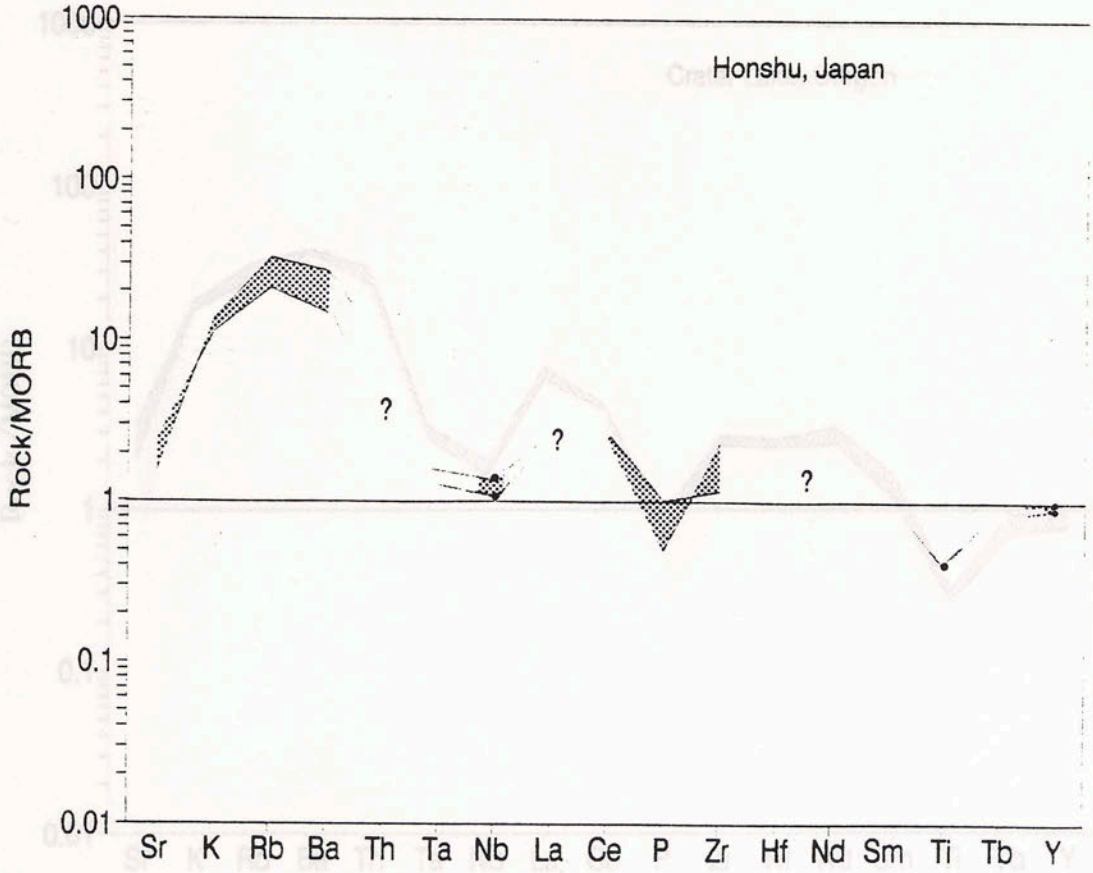

Figure 46. Spiderdiagrams depicting the range of MORB normalized trace and rare earth elements from Honshu, Japan (see Table 9 for references).

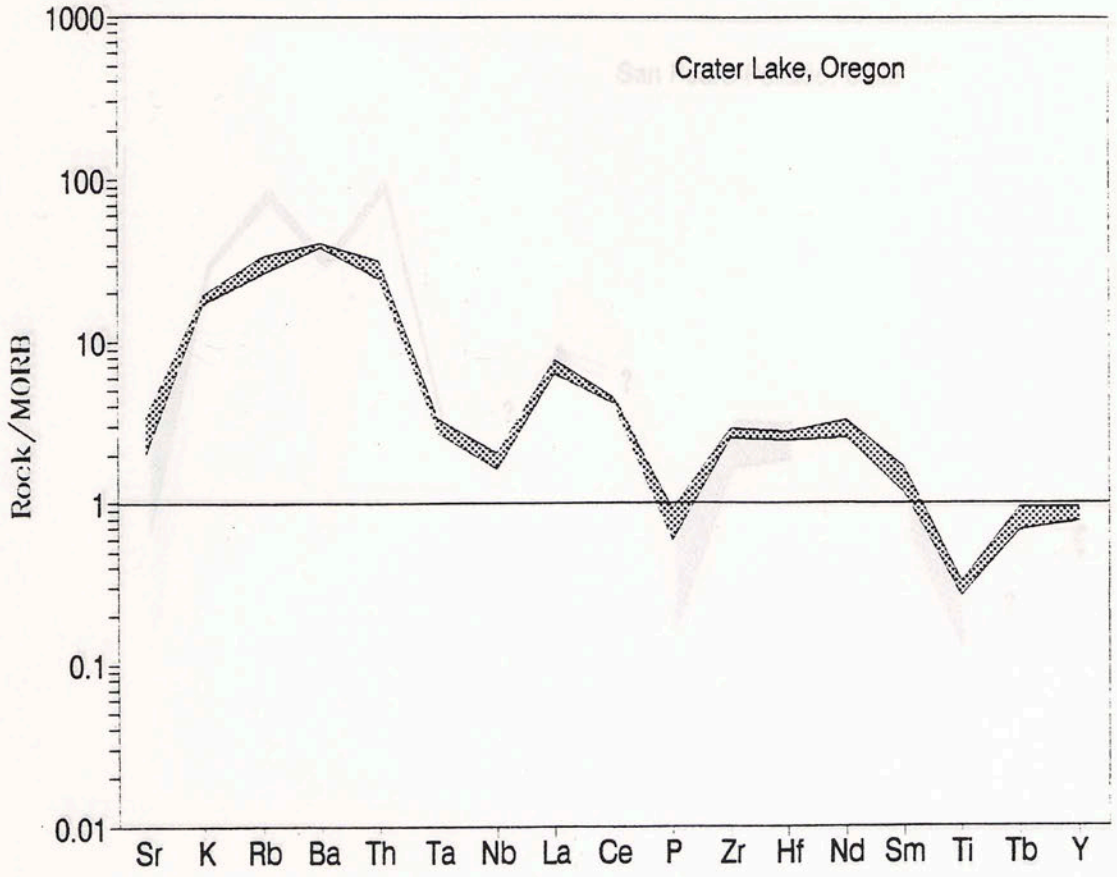

Figure 47. Spiderdiagrams depicting the range of MORB normalized trace and rare earth elements from Crater Lake, Oregon (see Table 9 for references).

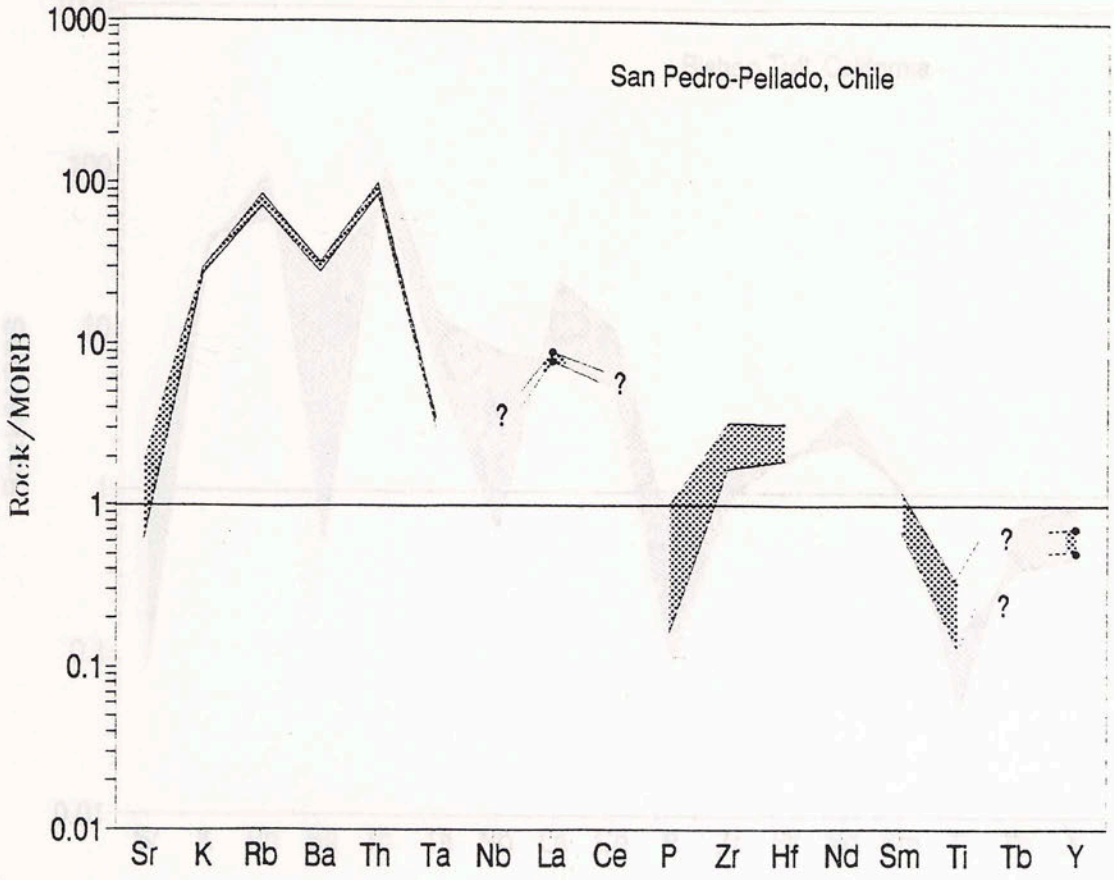

Figure 48. Spiderdiagrams depicting the range of MORB normalized trace and rare earth elements from San Pedro-Pellado, Chile (see Table 9 for references).

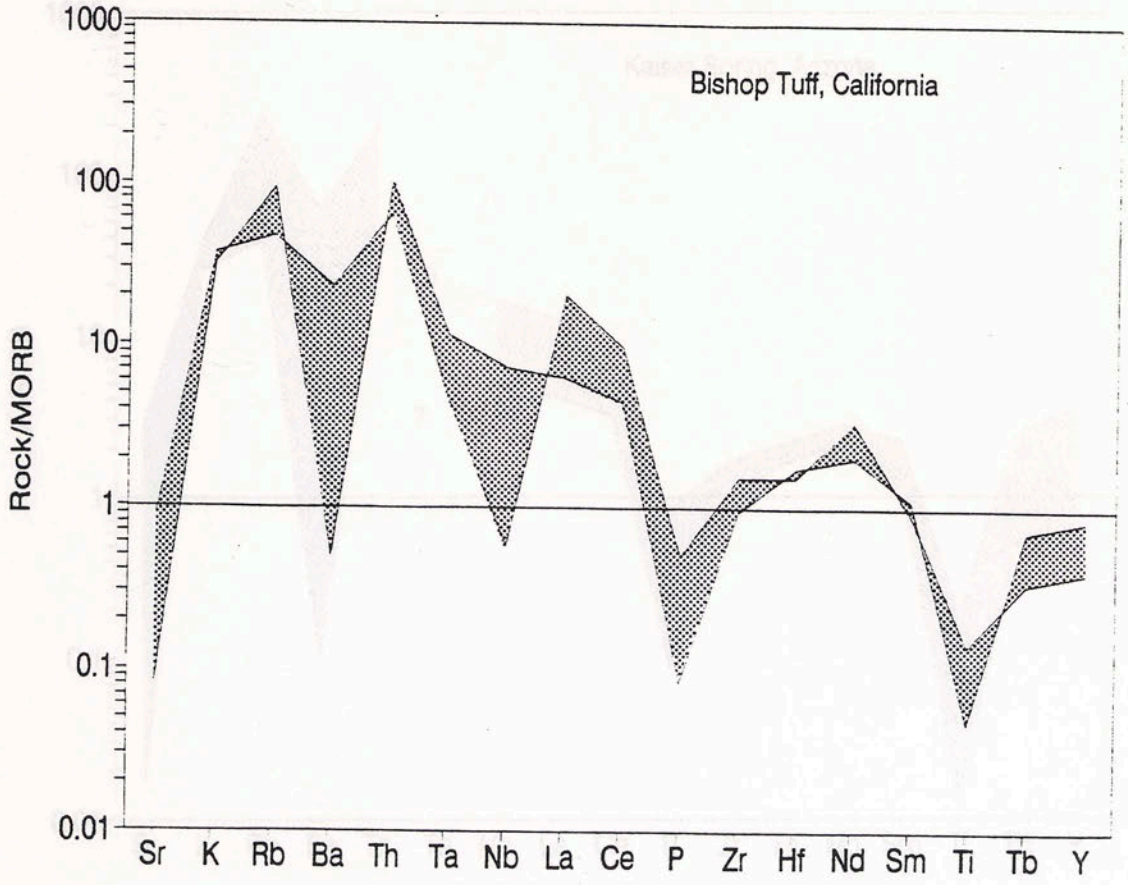

Figure 49. Spiderdiagrams depicting the range of MORB normalized trace and rare earth elements from the Bishop Tuff, California (see Table 9 for references).

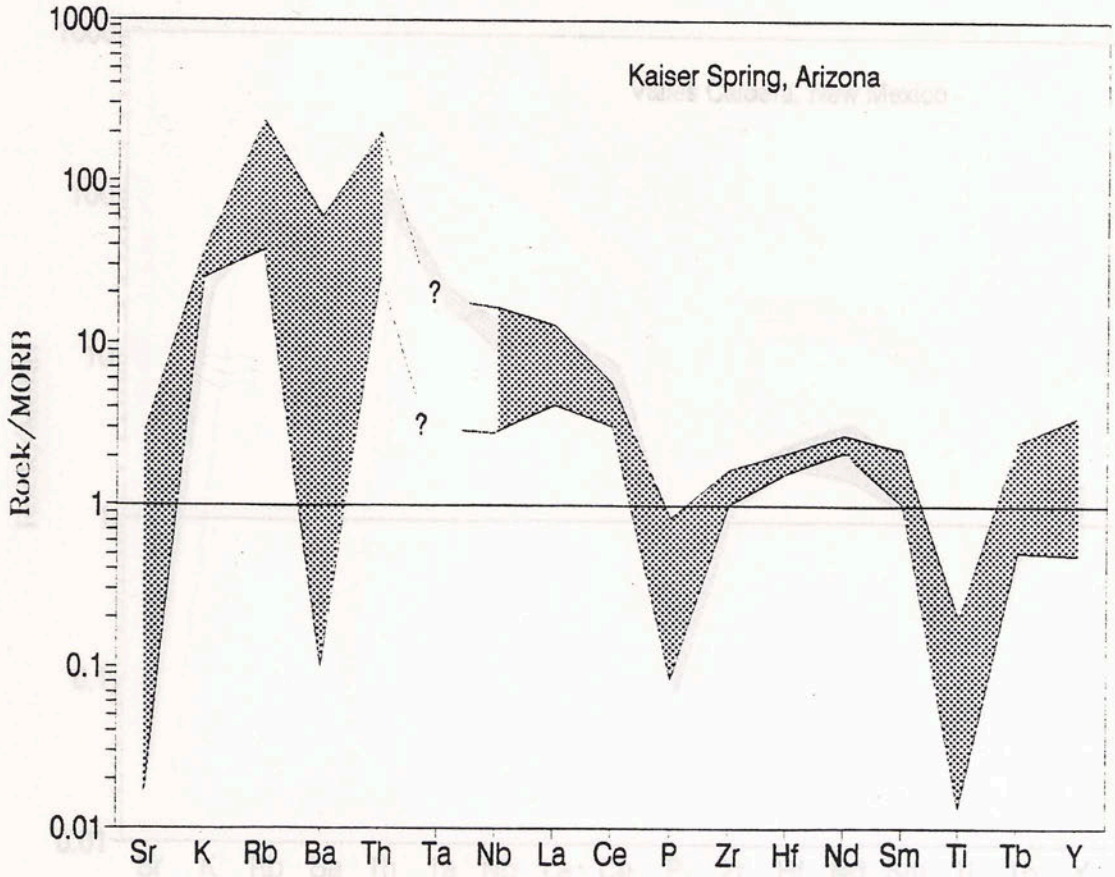

Figure 50. Spiderdiagrams depicting the range of MORB normalized trace and rare earth elements from Kaiser Spring, Arizona (see Table 9 for references).

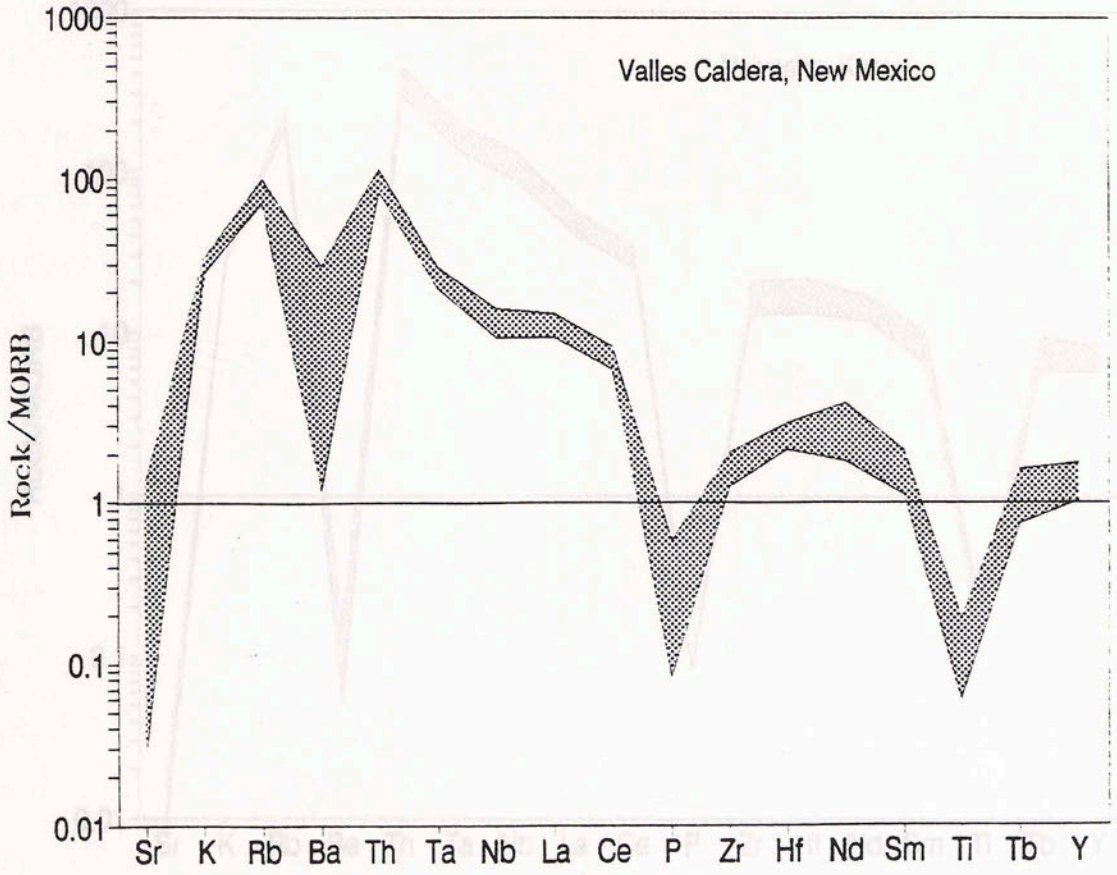

Figure 51. Spiderdiagrams depicting the range of MORB normalized trace and rare earth elements from Valles Caldera, New Mexico (see Table 9 for references).

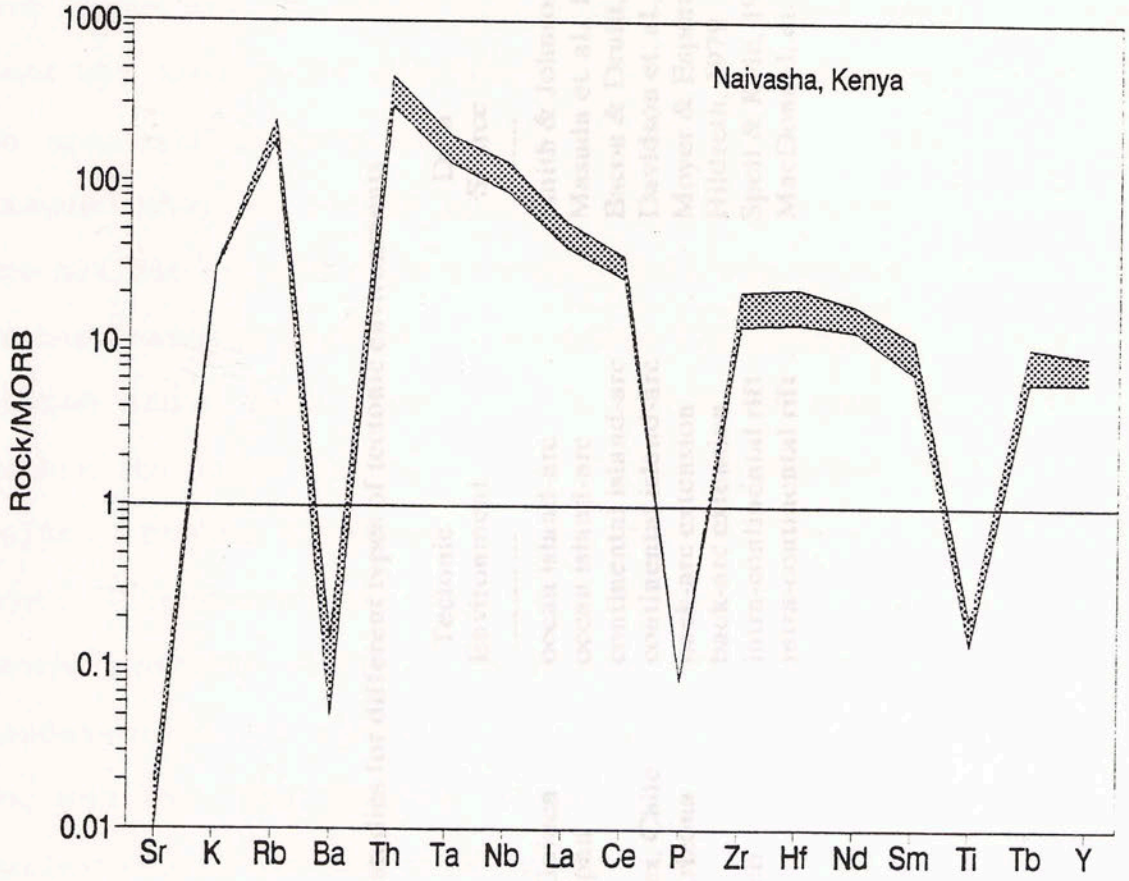

Figure 52. Spiderdiagrams depicting the range of MORB normalized trace and rare earth elements from Naivasha, Kenya (see Table 9 for references).

TABLE 11 Case studies for different types of tectonic environments

Volcanic Area	Tectonic Environment	Data Source
New Britain, Papua, New Guinea	ocean island-arc	Smith & Johnson, 1981
Nohi Volcanics, Central Japan	ocean island-arc	Masuda et. al., 1976
Crater Lake, Oregon	continental island-arc	Bacon & Druitt, 1988
San Pedro-Pellado Complex, Chile	continental island-arc	Davidson et. al., 1988
Kaiser Spring Volcanics, Arizona	back-arc extension	Moyer & Esperanca, 1989
Bishop Tuff, California	back-arc extension	Hildreth, 1979
Valles Caldera, New Mexico	intra-continental rift	Spell & Kyle, 1989
Naivasha, Kenya	intra-continental rift	MacDonald, et. al., 1987

their identical ionic potential values (7.58). Consequently, the extent of Ta and Nb depletion relative to Th and La is usually comparable. Volcanics associated with a subduction zone almost always have a strong Ta-Nb anomaly and New Guinea and Japan are no exception. The analytical data for Japan does not include Ta abundances. However, because both Ta and Nb are collectively depleted relative to Th and La, it is assumed that Nb points plot at MORB normalized values which are not much greater than Ta values in the spiderdiagram. All of the features present in the ocean island-arc spiderdiagrams listed above mean something in terms of what has happened within the magma during its evolution to produce the rhyolitic melts. Figure 53 shows a spiderdiagram of a basalt from an ocean island-arc setting. One of the important features of melts produced during subduction of oceanic crust is the preferential enrichment of the more mobile elements, Sr, K, Rb, and Ba. The immobile elements on the right side of the spiderdiagram are not greatly enriched relative to MORB. Note in this particular case, that the enrichments of the mobile elements are enrichments relative to a straight line that is not at 1. Different degrees of partial melting and crystal fractionation to form the basaltic melt do not affect the straightness of the line, but the position of the line along the y-axis of the spiderdiagram; not all mid-ocean ridge basalts plot at 1 when normalized to MORB. This enrichment

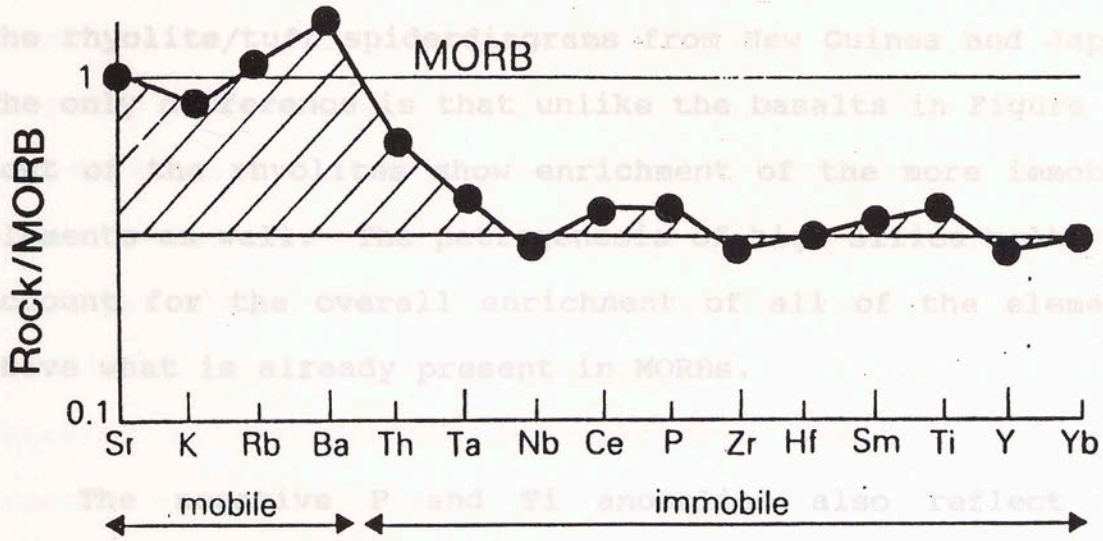

Figure 53. Spiderdiagrams of an ocean island-arc tholeiitic basalt. Mobile elements (and Th) show preferential enrichment relative to the immobile elements, as depicted by the shaded area beneath the geochemical pattern (after Pearce, 1983).

is attributed to dewatering of the subducting slab. Higher pressures and temperatures drive fluids out of the already metasomatized oceanic crust. The fluids then induce partial melting of the overlying mantle wedge (a sliver of the asthenosphere), thereby generating a basaltic melt. The mobile elements go into solution during dewatering of the slab and are incorporated into the basaltic melt. The same general preferential enrichment of mobile elements is seen in both of the rhyolite/tuff spiderdiagrams from New Guinea and Japan. The only difference is that unlike the basalts in Figure 53, most of the rhyolites show enrichment of the more immobile elements as well. The petrogenesis of high-silica melts can account for the overall enrichment of all of the elements above what is already present in MORBs.

The negative P and Ti anomalies also reflect the petrogenesis of rhyolitic melts. Apatite saturation is typically reached during crystal fractionation of an intermediate melt (SiO_2 ranges between 60-66 wt. %) to form a high-SiO_2 melt (Watson & Capobianco, 1981). Titaniferous minerals are also crystallizing during the evolution of silicic melts. With the pervasive crystallization of apatite and titanomagnetite in dacitic-rhyolitic melts, any segregation of these mineral phases from the melt fraction will produce a residual melt depleted in P and Ti, resulting

in the negative P and Ti anomalies in the spiderdiagrams.

The Ta-Nb anomaly (the depletion of both Ta and Nb relative to Th and La) can be indicative of tectonic environment. One explanation for the preferential depletion of Ta and Nb in subduction zones is that a mineral phase containing Ta and Nb, such as sphene, is retained in the solid rock phase during partial melting of the mantle wedge. The resulting melt produced by partial melting of the mantle rock material is subsequently depleted in Ta and Nb (Wilson, 1989). A Ta-Nb anomaly is not only pervasive in subduction volcanics, but also in some volcanics at extensional within-plate settings where there is a continental crust component. Studies of these non-subduction areas show that crustal material is incorporated into the melt (the melt undergoes crustal contamination). The crustal material itself is depleted in Ta and Nb relative to Th and La. A magma which has had a large proportion of this crustal material mixed into it will reflect the addition of a Ta-Nb depleted component by the presence of a Ta-Nb trough in the spiderdiagram.

Ta and Nb increase with increasing SiO_2 values in silicic melts. The spiderdiagrams for volcanics from New Guinea represent a collection of rhyolites and tuffs that contain a range of SiO_2 contents. It is notable that despite the range

of SiO_2 in the volcanics, there is very little vertical variation in the range of MORB-normalized Ta and Nb abundances in the spiderdiagrams. The overall enrichment of Ta and Nb during the generation of rhyolitic melts is not extensive enough to significantly decrease the depth of the Ta-Nb trough (relative to Th and La).

In island-arc volcanics, Sr and Ba are usually enriched with the other mobile elements, K, Rb, and Th. Those enrichments are no longer apparent in the spiderdiagrams of the rhyolites and tuffs. Sr partitions into plagioclase and because of its charge (and similar ionic potential), substitution is more extensive in Ca-rich plagioclase. Because Ca-plagioclase is the first plagioclase to start crystallizing in the calc-alkaline trend (the Bowen reaction series), Sr is depleted in the melt fairly early. By the time rhyolitic compositions are reached, Sr is greatly depleted relative to K and Rb. Variations in plagioclase fractionation account for the different degrees of Sr depletion. Feldspar fractionation also affects the relative abundance of Ba. Ba is readily substituted into alkali feldspar, which starts to become an important crystalizing phase at intermediate SiO_2 levels in the calc-alkaline trend. Alkali feldspar fractionation affects Ba in the same way plagioclase fractionation affects Sr. The only difference is that the

crystal fractionation of K-feldspar does not have a great affect on Ba abundances until SiO_2 reaches 60-66 wt.%, while plagioclase fractionation is controlling Sr abundances in the early stages of melt evolution, where SiO_2 is 55-60 wt. %. Consequently, Ba anomalies reflect a shorter history of feldspar fractionation than Sr anomalies, so that the negative Sr anomalies are noticeably larger than the negative Ba anomalies. The spiderdiagrams of both the New Guinea and Japan volcanics show that none of the Ba has been removed relative to the other mobile elements, K and Rb, indicating that little, if any, alkali feldspar was fractionated from the melts. Clearly, in these two examples of ocean island-arc volcanism, K-feldspar fractionation is insignificant (if not completely absent). At the same time, plagioclase fractionation is an inherent feature of rhyolites and tuffs, as evidenced by the persistent Sr anomalies. It will be seen that the size of both the Sr and Ba anomalies changes with tectonic environment; implying that the importance of alkali feldspar fractionation compared to Ca-plagioclase fractionation changes.

The same features described above in the spiderdiagrams for the two ocean island-arc settings are also present in the spiderdiagrams for the other tectonic settings. The continental island-arc spiderdiagrams (Figures 47 and 48) both

depict rhyolitic volcanics having a wide range of SiO_2 abundances (meaning, the geochemical signatures reflect varying degrees of melt differentiation). The Chilean volcanics have SiO_2 between 66-74 weight percent, while the Crater Lake, Oregon, volcanics have SiO_2 between 70-72 weight percent. Mobile element enrichment in the continental island-arc volcanics is anywhere between 10-80 times that of MORB. Sr is depleted relative to K, resulting in a strong Sr anomaly. Again, plagioclase fractionation during the petrogenesis of rhyolitic melts produced the large negative Sr anomalies in these volcanics. Alkali feldspar fractionation seems to be variable, as it was in the more mature ocean island-arc volcanics. Crater Lake volcanics have a slight Ba enrichment relative to Rb and Th, while the Chilean volcanics are all uniformly depleted in Ba. It can be inferred that alkali feldspar fractionation overwhelmed the overall enrichment of the mobile elements in the Chilean volcanics such that a significant quantity of Ba was removed from the high-silica melts to form negative Ba anomalies. If there was alkali feldspar fractionation in the Crater Lake volcanics, it was not extensive enough to result in a net depletion of Ba relative to Rb and Th. P and Ti anomalies are still pervasive as well. Note that there is more variability in the degree of relative P, Ti and Sr depletion (depletion relative to neighboring elements in the spiderdiagrams) in the

Chilean volcanics than in the Crater Lake volcanics. This is because the analyses shown in the Chilean spiderdiagram reflect varying degrees of melt differentiation, as evidenced by their greater range in SiO_2; there is a range of 8 weight percent in the Chilean volcanics, as opposed to a range of 2 weight percent SiO_2 in the Crater Lake volcanics. With the large variablility in SiO_2 in the Chilean volcanics, it is important to note the consistency of the shape of the Ta-Nb trough (Nb data is lacking in the Chilean volcanics; it is assumed that the MORB-normalized value of the Nb data, if present, would be close to the MORB-normalized Ta values, thereby depicting a Ta-Nb trough where both elements are depleted relative to Th and La). Differing degrees of melt evolution usually result in the subsequent enrichment of elements such as Ta and Nb with increasing SiO_2. This is not seen in the continental island-arc volcanics; despite varying degrees of SiO_2, the amount of relative Ta and Nb depletion remains consistent.

Unlike the island-arc volcanics, modification of the Ta-Nb trough is evident in the spiderdiagrams from back-arc basins. The lower limits of the Kaiser Spring volcanics spiderdiagram shows a depletion in Nb relative to La, so it can be assumed that Ta is probably also depleted such that there is a slight Ta-Nb trough. The upper limits of the

spiderdiagram, however, do not show any Nb depletion relative to La. On the contrary, Nb is slightly enriched relative to La; it is therefore assumed that the top of the spiderdiagram pattern does not have a Ta-Nb trough. The vertical range in MORB-normalized Nb values in the Arizona spiderdiagram reflects increasing Nb abundances. Because the bottom Nb point is depleted relative to La and the top Nb point is not, it can be inferred that the Ta-Nb trough disappears with increasing Nb concentrations. The same is true in the Bishop Tuff spiderdiagram, where the shaded area covers the vertical range in MORB-normalized elemental abundances. The depleted trend depicts a Ta-Nb trough where Ta and Nb are both depleted relative to La and the other enriched trend show Ta and Nb to be enriched relative to La.

Trace element and rare earth elements from samples which represent the two end-members (an enriched end-member from the base of the tuff unit and a depleted end-member from the top of the tuff unit) are shown in the spiderdiagram of the Bishop Tuff (Figure 49). The analyses of the two Bishop Tuff endmembers are the same analyses used to produce the elemental ratios (the enrichment factors) in Figure 44 (Hildreth, 1981). The spiderdiagrams for the Kaiser Spring rhyolites, Arizona (Figure 50) show essentially the same trends as those for the Bishop Tuff; enriched volcanics and depleted volcanics. There

are two groups of samples in the Kaiser Spring spiderdiagrams. One group is referred to as high-silica rhyolites (HSR; silica ranges between 76-77 wt. % SiO_2) and the other group is low-silica rhyolites (LSR; 70-74 wt. % SiO_2). In this particular suite of rhyolites, the HSR melt is thought to have been derived directly from the LSR melt by crystal fractionation. Consideration of the HSR spiderdiagrams shows that continued differentiation of the LSR melt served to remove the Ta-Nb trough, increase the relative depletion of Sr, P and Ti and to create a persistent negative Ba anomaly. Given the absence of large Ba anomalies in the LSRs, it can be inferred that alkali feldspar fractionation was not an important process during the formation of the LSR melts, yet was quite important during the generation of the HSR melts. The same situation is seen in the Bishop Tuff. The more evolved melt (the melt with higher SiO_2 values) no longer has a Ta-Nb trough (Ta and Nb are not depleted relative to La), Sr, P and Ti anomalies are even more negative and there is a large Ba depletion. Here, some alkali feldspar fractionation produced the small Ba anomaly in the depleted melt. The processes driving magma differentiation within the magma chamber must have involved greater degrees of alkali feldspar fractionation to produce the enriched melt, resulting in an even larger negative Ba anomaly.

Looking at the spiderdiagrams from back-arc basin volcanics, it can be seen that essentially the same processes are at work to produce the same assortment of anomalies and enrichments relative to MORB. Specifically, a subduction component is increasing K, Rb and Th abundances relative to the rest of trace and rare earth elements, feldspar fractionation causes Sr to be depleted relative to K and Ba to be depleted relative to Rb and Th, partial melting of the mantle wedge and/or incorporation of crustal material produces a Ta-Nb trough (which is absent in those back-arc basin samples which experienced melt evolution to higher silica concentrations), and the fractionation of apatite and a titaniferous mineral produces the negative P and Ti anomalies (depletions in P relative to Ce and Zr and depletions in Ti relative to Sm and Tb). What sets the back-arc extensional volcanics apart from the island-arc volcanics is the absence of a Ta-Nb trough in the higher silica volcanics and the extremely large negative Ba anomalies present in some of the samples. Apparently, melt evolution seems to progress even further in the back-arc basin volcanics than in the island-arc volcanics and alkali feldspar fractionation is much more active. The reason for these seemingly tectonically-dependent geochemical differences is not known.

In the spiderdiagrams from continental rift zones, the

absence of a subduction component is clearly reflected in the geochemical trends by the lack a Ta-Nb trough in all samples. Volcanics from both the Rio Grande rift zone in New Mexico and the East African rift zone in Kenya are shown in Figures 51 and 52. Apart from the persistent absence of a Ta-Nb trough, the spiderdiagram trends are very similar to those of the continental island-arcs and back-arc basins. Subtle differences can be noted, however. Specifically, the maximum depths of the relative Sr and Ba depletions (depletions relative to K, Rb and Th) are noticeably greater in rift zone spiderdiagrams. In spiderdiagrams from island-arc settings, the values of Ba minima in all of the samples are still at least 10 times that of MORB. The extent of Ba depletion relative to Rb and Th in both back-arc basins and rift zones is highly variable; MORB-normalized Ba minima typically range between 0.1-60 times that of MORB. The size of the negative Sr anomalies also varies between island-arc settings and within plate settings. Island-arc volcanics have Sr minima values limited to being no less than 0.1 times that of MORB. Within-plate volcanics, on the other hand, have Sr minima values much less than 0.1 times that of MORB, with some samples showing abundances reaching almost 0.01 times that of MORB.

Tectonic Discrimination

There are three key features in the spiderdiagrams that can be collectively used to discriminate between tectonic

environments: 1) the presence or absence of a Ta-Nb trough within a volcanic suite and whether or not this trough has been modified in any of the volcanics, 2) both the magnitude and degree of variability of Sr and Ba anomalies and 3) the extent of mobile element enrichment relative to MORB. The latter feature is only useful in discriminating between oceanic and continental island-arcs. The first two features, used in conjunction, can differentiate between convergent island arcs, back-arc extensional volcanics and rift-zone extensional volcanics. The manner in which these geochemical features can be used to differentiate between tectonic settings, using spiderdiagrams of tuffs and rhyolites, is summarized in Table 12.

Spiderdiagrams of the Stanley tuffs (Beavers Bend and Hatton Tuffs, specifically) and Sabine rhyolites (Figures 54 through 56) have the same appearance as those of the young, unaltered rhyolites and tuffs from the various tectonic settings. In particular, the same anomalies are present for Sr, Ba, Ta-Nb, P and Ti. Given the combined occurrence of weathering, diagenesis and differential settling of grains during deposition, it is notable that all of the tuffs and rhyolites plot in a fairly consistent manner. The variable extent of weathering, diagenesis and differential settling of grains in the different tuff samples is reflected in the

TABLE 12 Discrimination of tectonic environment

	Lithophile Enrichment	Ba & Sr Anomalies	Ta-Nb Trough
Ocean island-arc:	noticeable less than 100xMORB (unless arc is mature like Japan)	Ba: if present, anomaly minima > 10xMORB Sr: if present, anomaly minima > 0.5xMORB	present in all samples
Continental island arc:	100xMORB or greater	Ba: anomaly minima generally > 10xMORB Sr: anomaly minima generally > 0.5xMORB	present in all volcanics with little modification with melt differentiation
Back-arc extension:	100xMORB or greater	Ba: anomaly minima generally < 100xMORB and > 0.1xMORB Sr: anomaly minima generally < 10xMORB and > 0.01xMORB	present in less evolved volcanics, modified in more evolved volcanics due to Ta and/or Nb enrichment
Intra-continental rift:	100xMORB or greater	Ba: anomaly minima generally < 100xMORB and > 0.1xMORB Sr: anomaly minima generally < 10xMORB and > 0.01xMORB	not present in any of the volcanics unless there is fractionation of a Ta/Nb mineral phase

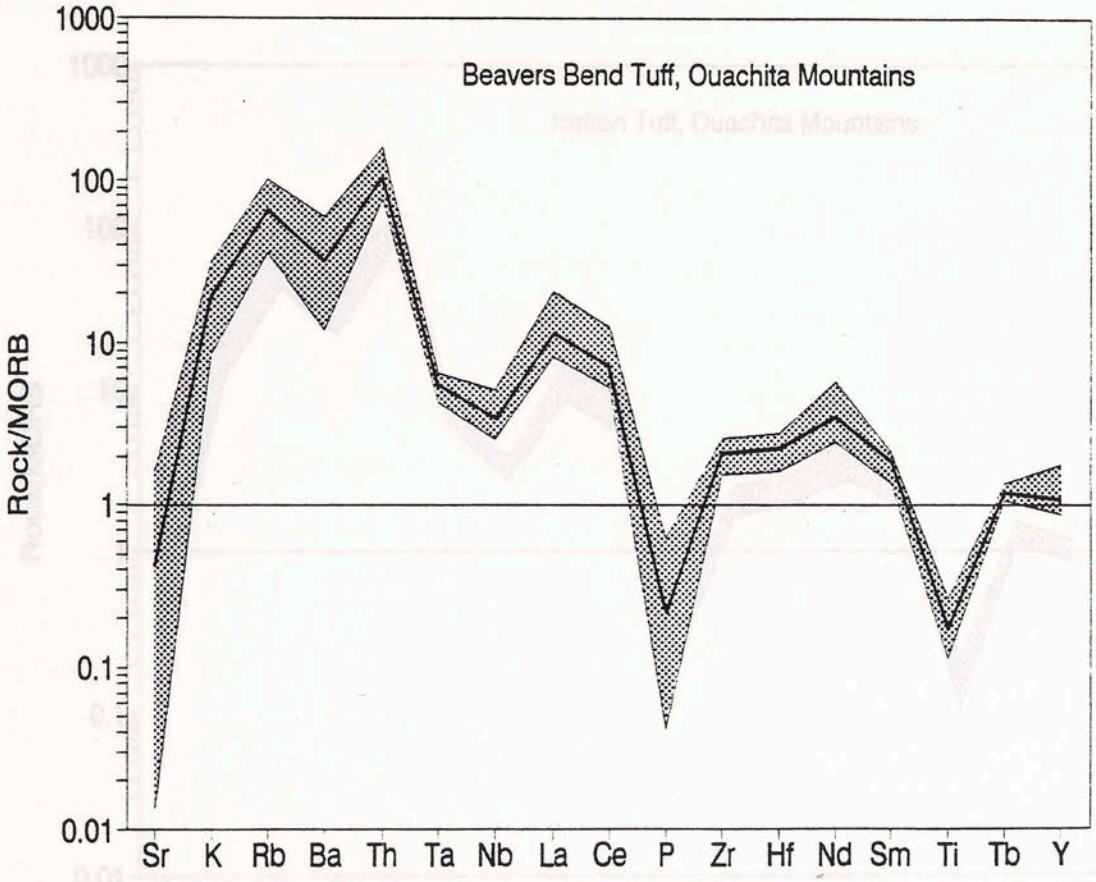

Figure 54. Spiderdiagrams depicting the range of MORB normalized trace and rare earth elements for the Beavers Bend Tuff samples. The solid black line in Figure 54 represents the average Beavers Bend Tuff composition.

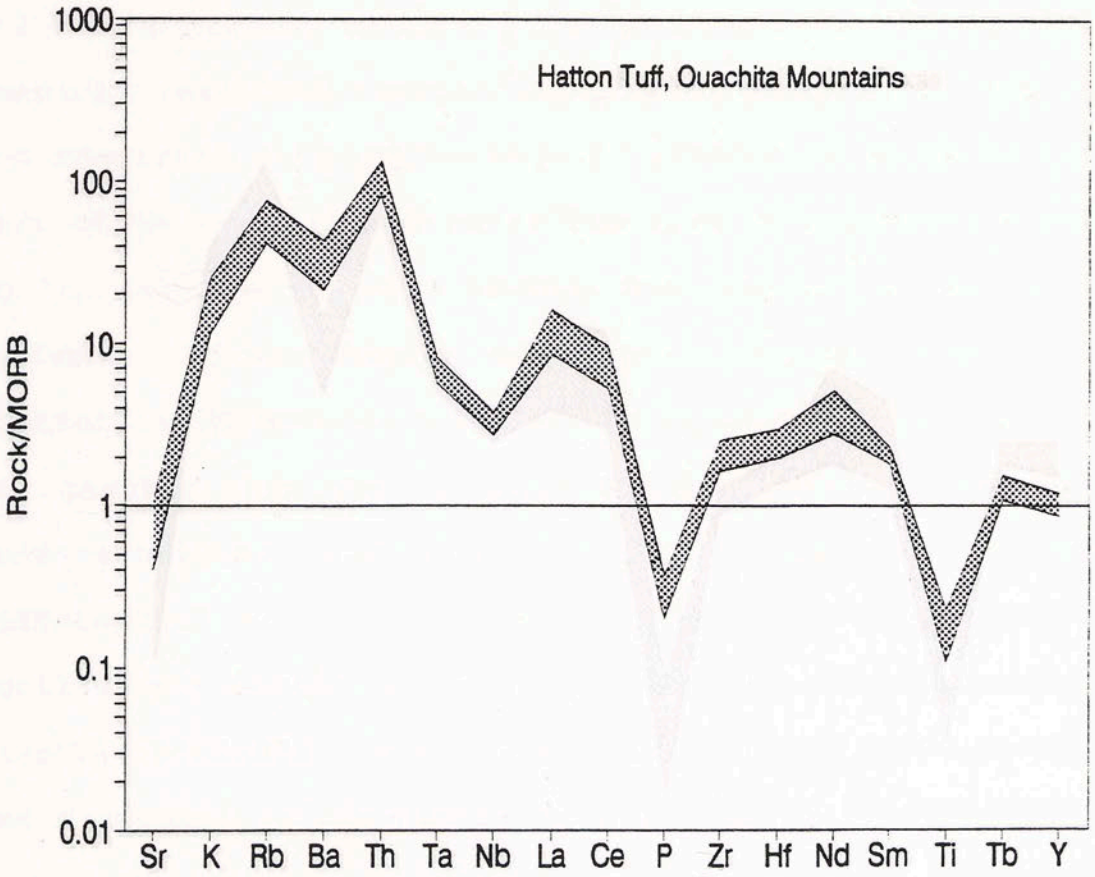

Figure 55. Spiderdiagrams depicting the range of MORB normalized trace and rare earth elements for the Hatton Tuff samples.

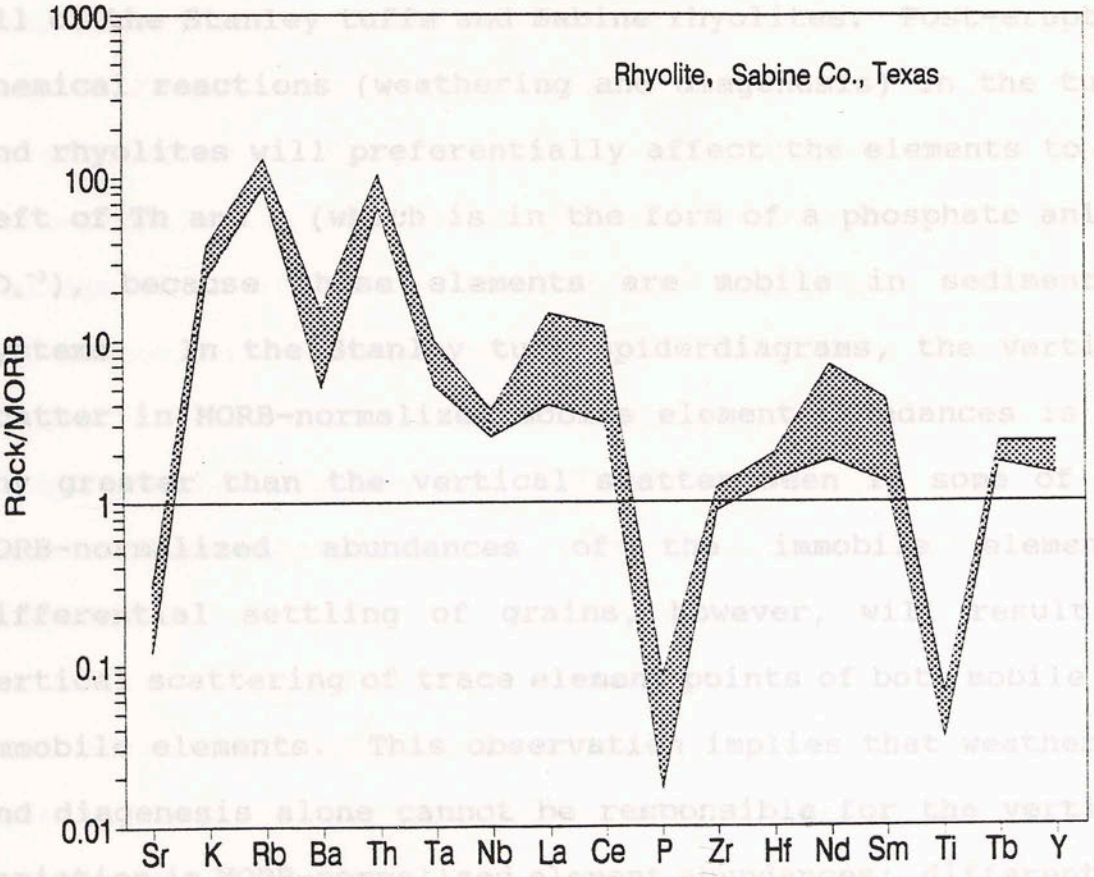

Figure 56. Spiderdiagrams depicting the range of MORB normalized trace and rare earth elements for the Sabine rhyolite samples.

spiderdiagrams of individual samples by the vertical scatter in MORB-normalized element abundances and the slight differences between samples of spiderdiagram patterns. Despite the vertical scatter in element abundances relative to MORB, the overall geochemical patterns are consistent for all of the Stanley tuffs and Sabine rhyolites. Post-eruptive chemical reactions (weathering and diagenesis) in the tuffs and rhyolites will preferentially affect the elements to the left of Th and P (which is in the form of a phosphate anion, PO_4^{-3}), because these elements are mobile in sedimentary systems. In the Stanley tuff spiderdiagrams, the vertical scatter in MORB-normalized mobile element abundances is not any greater than the vertical scatter seen in some of the MORB-normalized abundances of the immobile elements. Differential settling of grains, however, will result in vertical scattering of trace element points of both mobile and immobile elements. This observation implies that weathering and diagenesis alone cannot be responsible for the vertical variation in MORB-normalized element abundances; differential settling of grains must be causing most the "noise" in the spiderdiagrams. In the case of the Stanley tuffs, Sr, Ba, K, P, Ti, Zr and Hf are the elements which would be the directly affected by differential settling of feldspars, Fe-Ti oxides and heavy minerals (apatite and zircon). These specific elements do show vertical variation in the spiderdiagrams.

As mentioned previously, differential settling of grains during deposition results in the same relative enrichments and depletions of elements as do igneous processes in the magma chamber (crystal fractionation and convection-driven diffusion). This means that most of the variation seen in the MORB-normalized element abundances for the various tuff samples (especially in those elements which are immobile) can be attributed as much to igneous processes as it can be to post-eruptive depositional process. The mean elemental abundances in all of the Beavers Bend Tuff samples and all of the Hatton Tuff samples are normalized to MORB and shown in Figure 57. It is concluded that the resulting spiderdiagrams of the average Beavers Bend Tuff and the average Hatton Tuff represent geochemical patterns which largely reflect igneous processes.

Sr and Ba anomalies in Figure 57 show depletions which have minimum values consistent with those values seen in continental island-arcs. Even if the maximum range in vertical variation in MORB-normalized Sr and Ba abundances is considered in the individual Stanley tuff samples, the Sr points are all still greater than 0.1 times that of MORB. The same situation is true of Ba. Despite the vertical range in MORB-normalized Ba concentrations, the negative Ba anomaly minima are still greater than 10 times that of MORB. The

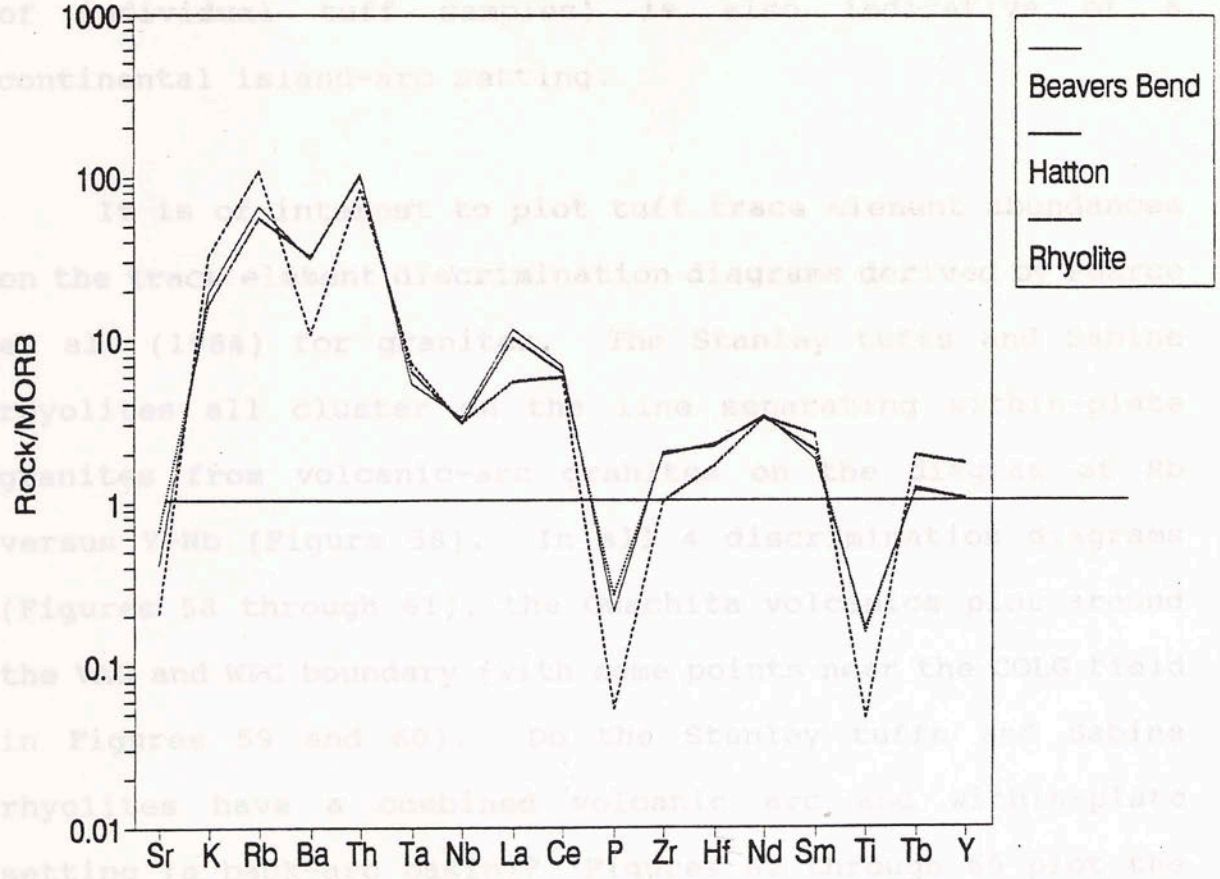

Figure 57. Mean abundances of the Beavers Bend Tuff samples, Hatton Tuff samples and Sabine rhyolite samples normalized to MORB.

average tuff spiderdiagram patterns reflect the same Sr and Ba characteristics. Together, the nature of the two anomalies is characteristic of continental island-arc volcanics. The persistent occurrence and shape of a Ta-Nb trough in the Stanley tuffs and rhyolites (especially in the spiderdiagrams of individual tuff samples) is also indicative of a continental island-arc setting.

It is of interest to plot tuff trace element abundances on the trace element discrimination diagrams derived by Pearce et al. (1984) for granites. The Stanley tuffs and Sabine rhyolites all cluster on the line separating within-plate granites from volcanic-arc granites on the diagram of Rb versus Y+Nb (Figure 58). In all 4 discrimination diagrams (Figures 58 through 61), the Ouachita volcanics plot around the VAG and WPG boundary (with some points near the COLG field in Figures 59 and 60). Do the Stanley tuffs and Sabine rhyolites have a combined volcanic arc and within-plate setting (a back-arc basin)? Figures 62 through 65 plot the rhyolites and tuffs from the 8 different tectonic settings to see if rhyolite analyses can be tectonically discriminated by the granite discrimination diagrams. The continental rift zone volcanics from Kenya and the Valles Caldera volcanics from New Mexico consistently plot in the WPG field. Likewise, both the continental and oceanic island-arc volcanics (Andes,

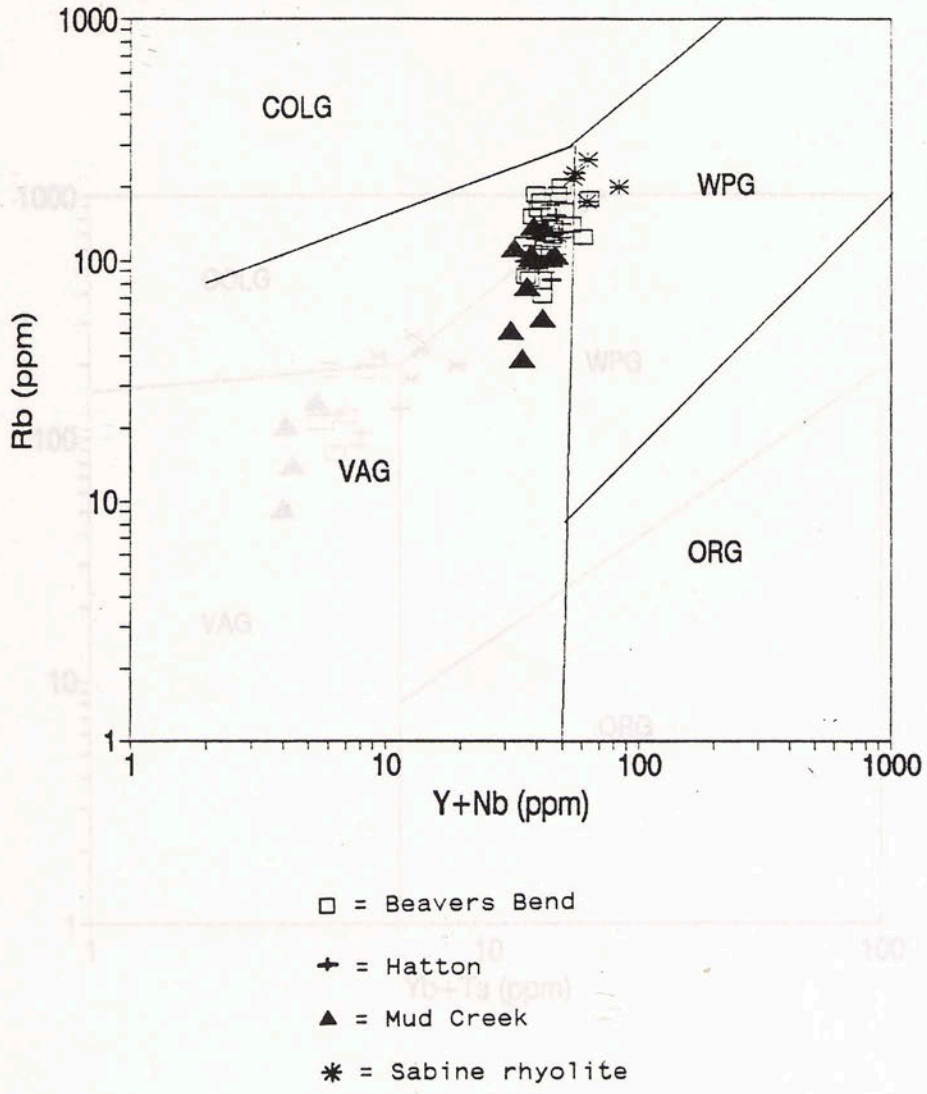

Figure 58. Plot of the Stanley tuffs and Sabine rhyolite on a granite tectonic discrimination diagram developed by Pearce et al. (1984). ORG = ocean ridge granites, VAG = volcanic arc granites, WPG = within plate granites, COLG = collision granites.

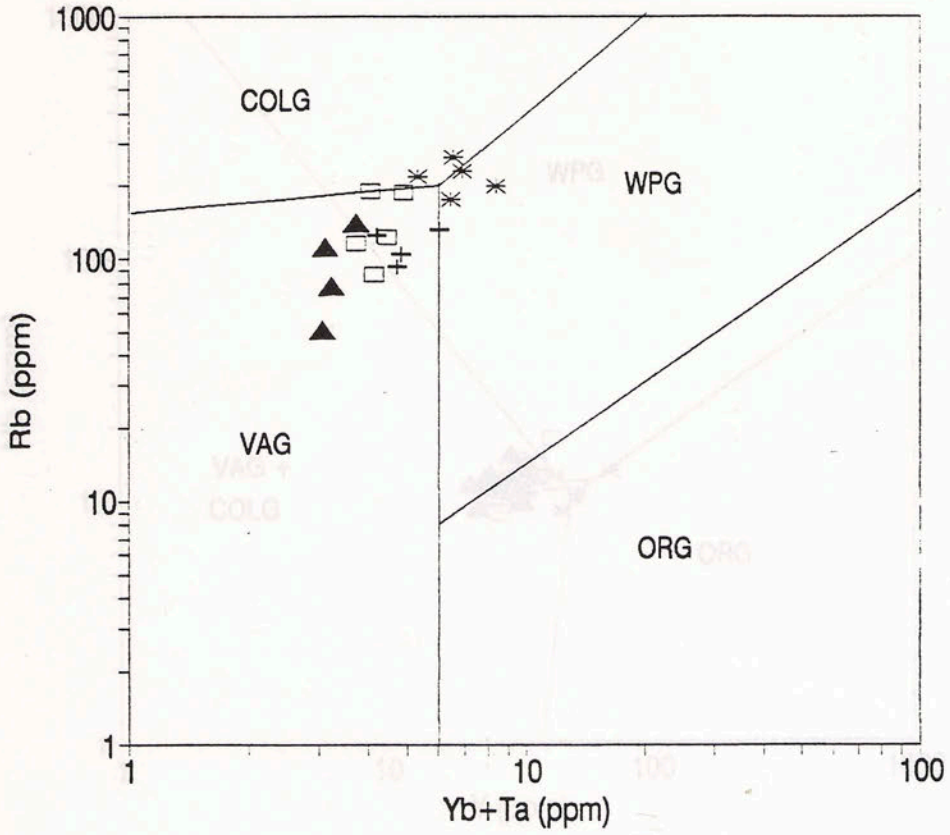

Figure 59. Plot of the Stanley tuffs and Sabine rhyolite on a granite tectonic discrimination diagram developed by Pearce et al. (1984). ORG = ocean ridge granites, VAG = volcanic arc granites, WPG = within plate granites, COLG = collision granites.

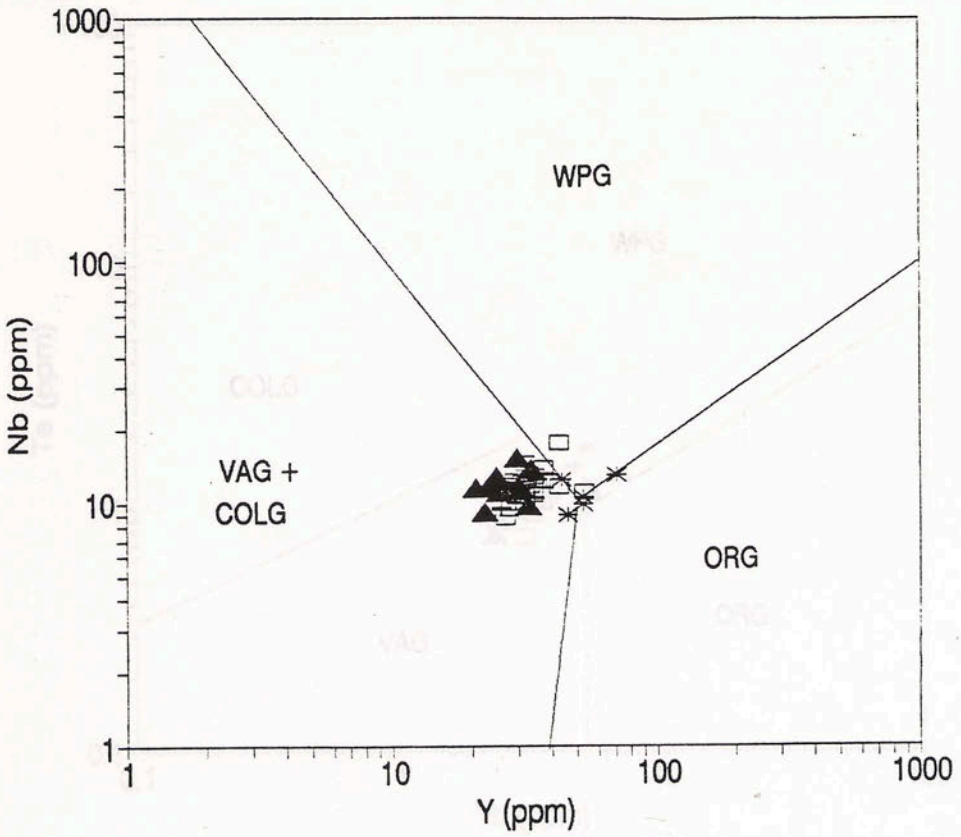

Figure 60. Plot of the Stanley tuffs and Sabine rhyolite on a granite tectonic discrimination diagram developed by Pearce et al. (1984). ORG = ocean ridge granites, VAG = volcanic arc granites, WPG = within plate granites, COLG = collision granites.

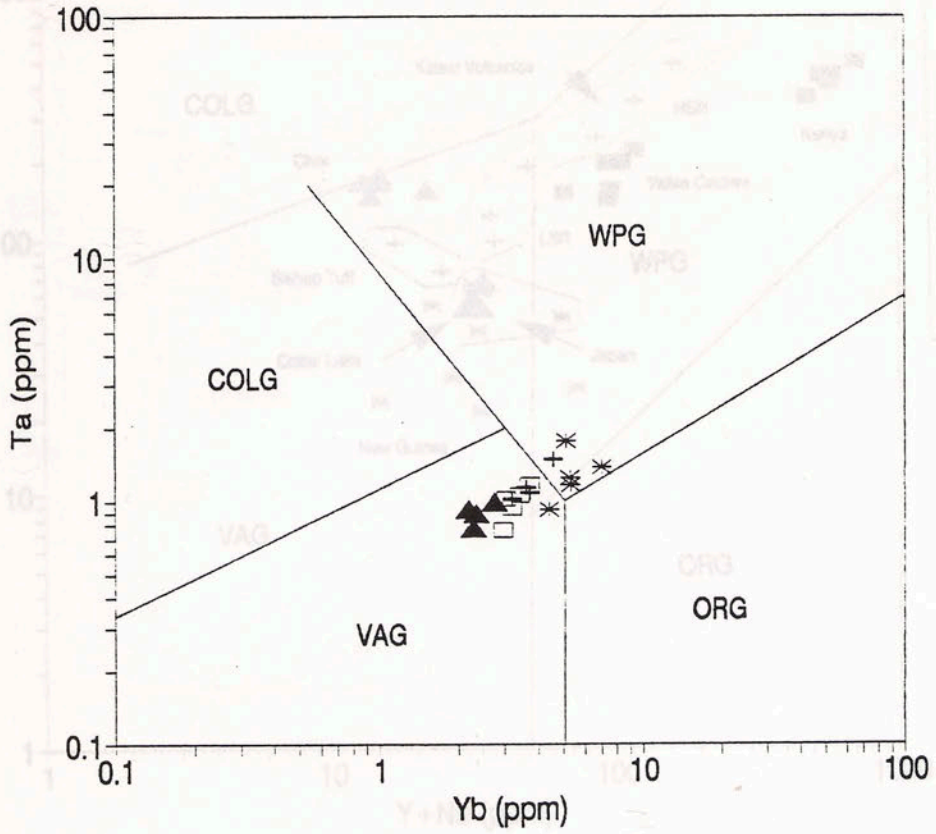

Figure 61. Plot of the Stanley tuffs and Sabine rhyolite on a granite tectonic discrimination diagram developed by Pearce et al. (1984). ORG = ocean ridge granites, VAG = volcanic arc granites, WPG = within plate granites, COLG = collision granites.

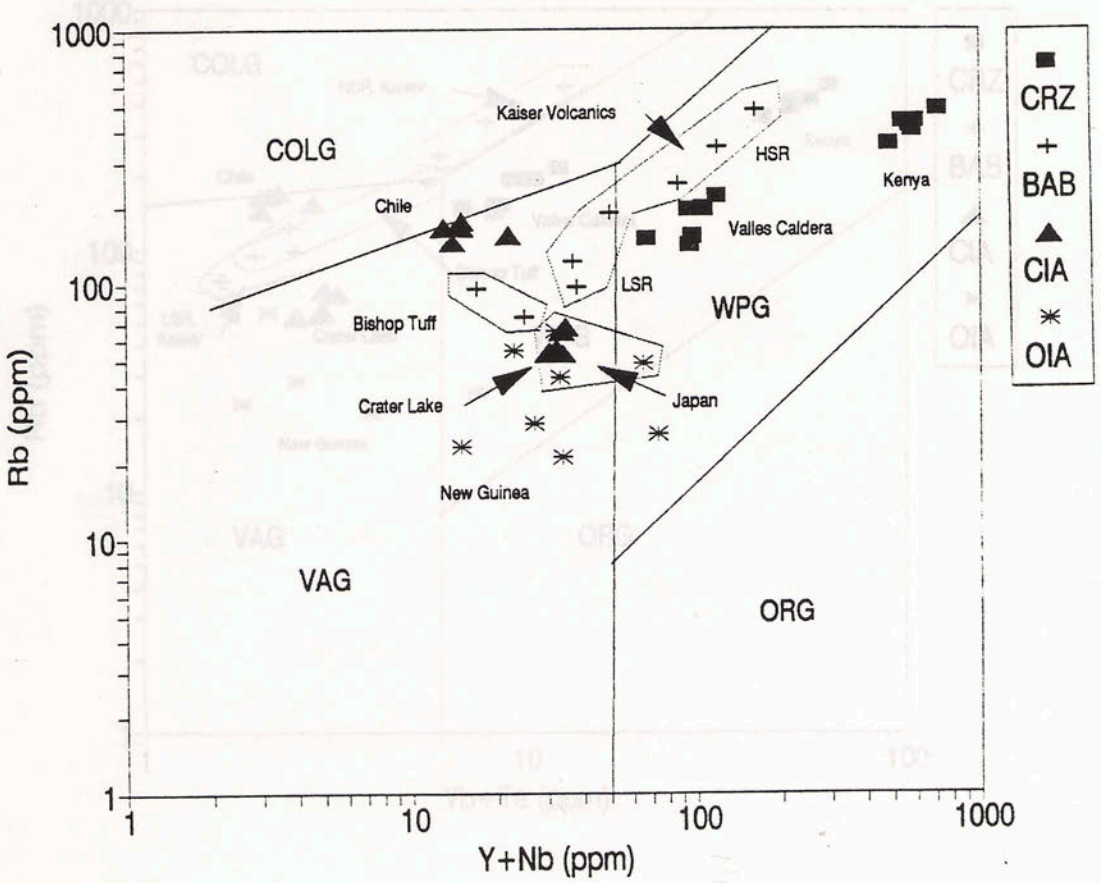

Figure 62. Trace element abundances in the volcanics from the eight modern tectonic settings plotted on a granite discrimination diagram. Asterisks = ocean island-arc, triangles = continental island-arc, pluses = back-arc basins, squares = continental rift zone.

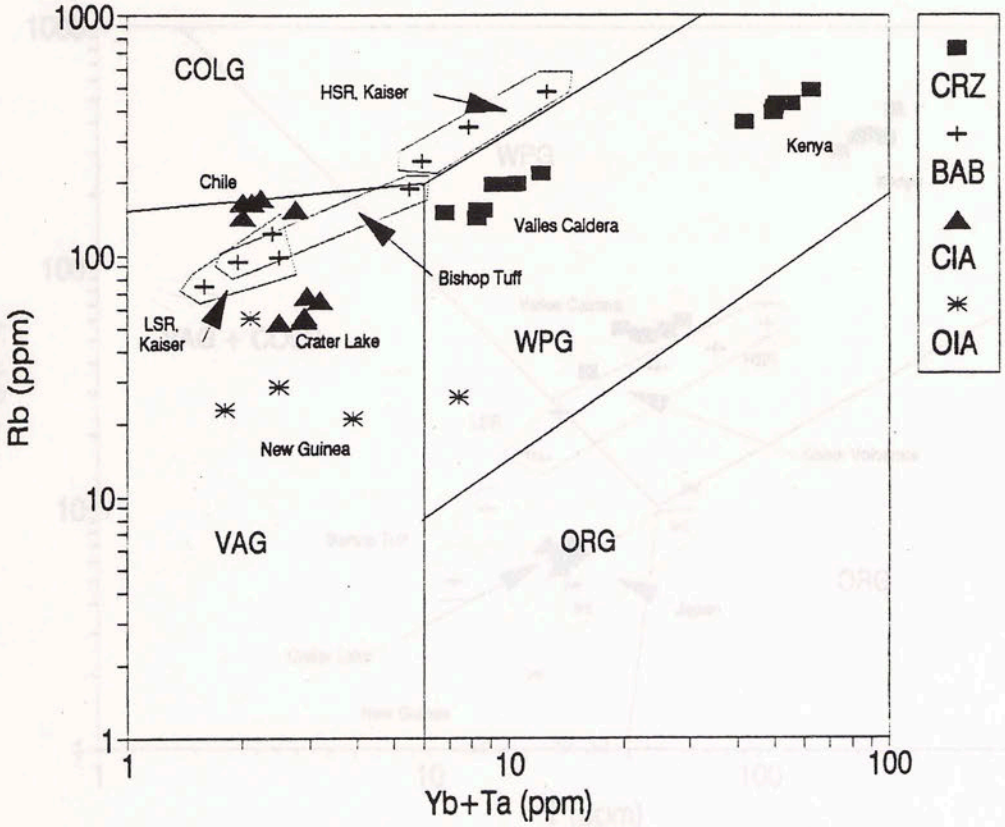

Figure 63. Trace element abundances in the volcanics from the eight modern tectonic settings plotted on a granite discrimination diagram. Asterisks = ocean island-arc, triangles = continental island-arc, pluses = back-arc basins, squares = continental rift zone.

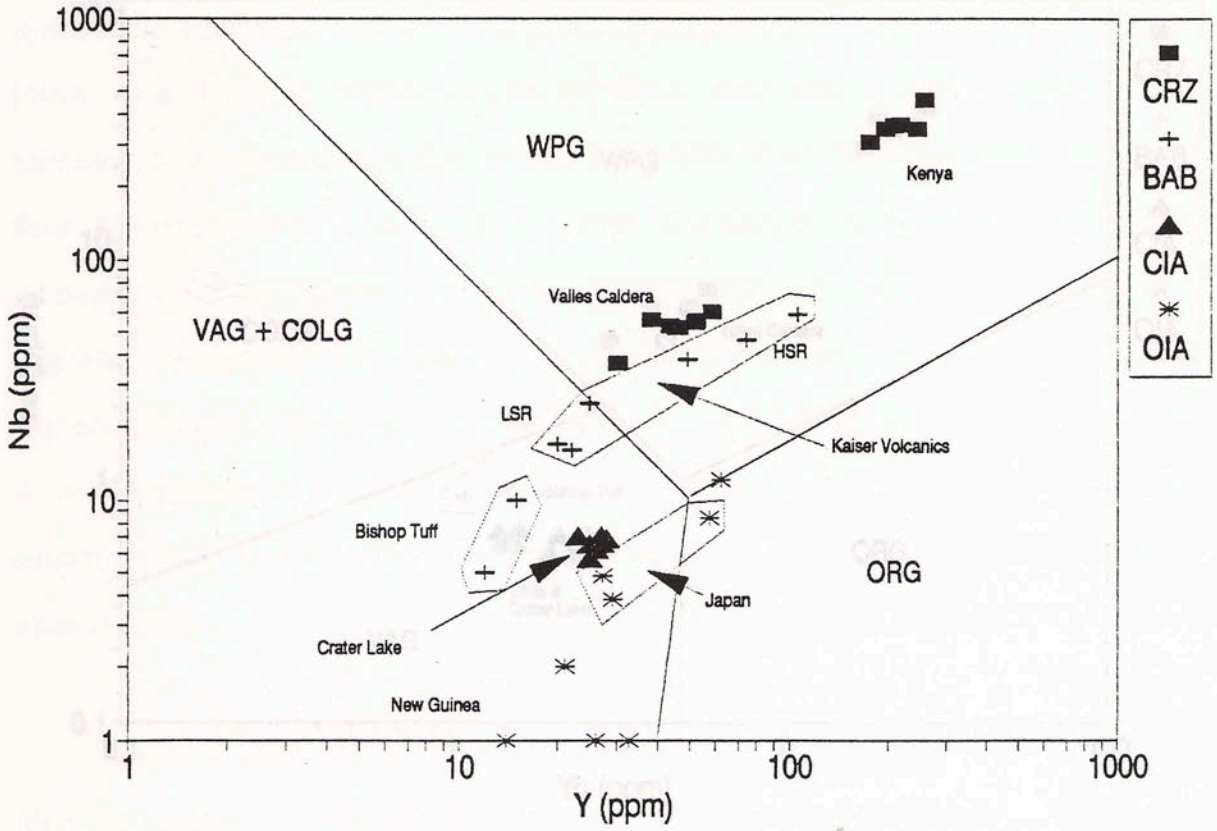

Figure 64. Trace element abundances in the volcanics from the eight modern tectonic settings plotted on a granite discrimination diagram. Asterisks = ocean island-arc, triangles = continental island-arc, pluses = back-arc basins, squares = continental rift zone.

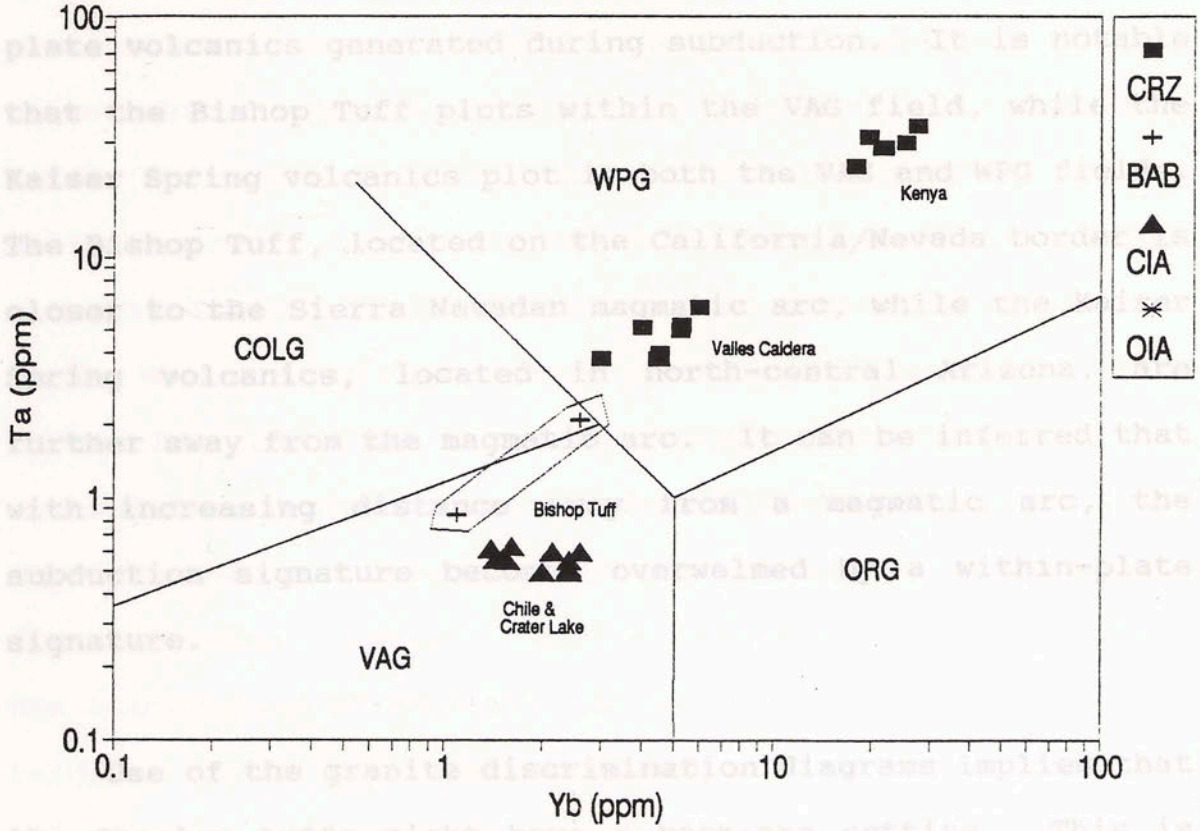

Figure 65. Trace element abundances in the volcanics from the eight modern tectonic settings plotted on a granite discrimination diagram. Asterisks = ocean island-arc, triangles = continental island-arc, pluses = back-arc basins, squares = continental rift zone.

Chile; Crater Lake, Oregon; Papua, New Guinea) fall within the VAG field. One sample in the New Guinea suite falls outside the VAG field, in the WPG zone. Back-arc rhyolites and tuffs tend to spread across both the VAG and WPG field. This is to be expected since back-arc volcanics are essentially within-plate volcanics generated during subduction. It is notable that the Bishop Tuff plots within the VAG field, while the Kaiser Spring volcanics plot in both the VAG and WPG fields. The Bishop Tuff, located on the California/Nevada border is closer to the Sierra Nevadan magmatic arc, while the Kaiser Spring volcanics, located in north-central Arizona, are further away from the magmatic arc. It can be inferred that with increasing distance away from a magmatic arc, the subduction signature becomes overwelmed by a within-plate signature.

Use of the granite discrimination diagrams implies that the Stanley tuffs might have a back-arc setting. This is inferred by the location of most of the points (as well as the averages for the Beavers Bend Tuff, Hatton Tuff, and Mud Creek Tuff) within either the VAG field or the WPG fields. A few points fall within the COLG and ORG fields as well. It is uncertain whether the diagrams used to tectonically classify granites are valid for rhyolites, as there are geochemical differences between high-silica intrusives and extrusives.

The geochemical patterns of rhyolites and tuffs undergo varying degrees of alteration during deposition and post-depositional diagenesis. Diagenesis can result in significant element fractionation because rhyolites and tuffs contain a large percentage of volcanic glass, which is susceptible to extensive alteration, unlike granites. Given the extent of grain segregation and diagenesis in the Stanley tuffs, the position of the tuffs within the diagrams may not be tectonically real. On the other hand, 4 of the 5 trace elements used to discriminate tectonic setting are immobile. Y, Yb, Nb and Ta all have ionic potentials exceeding 3, while Rb has Z/r less than 3. It is probable that diagenesis has not modified trace element concentrations to the point where rhyolite and tuff locations are noticeably different on the discrimination diagrams. Unlike diagenesis and weathering, the segregation of crystals during deposition, specifically feldspar (with Rb), apatite (which contains Y and Yb) and titaniferous minerals (which contain Ta and Nb), will modify the original, pre-eruptive whole rock compositions. It is concluded that the location of the Stanley tuffs and Sabine rhyolites in both the VAG and WPG fields may be valid. The tectonic environment which has the characteristics of both a volcanic arc and within plate setting is a back-arc basin. At the same time, the segregation of crystals and glass within the tuffs may be extensive enough so that the apparent

tectonic settings of the tuffs and rhyolites in these discrimination diagrams are not legitimate.

DISCUSSION

The geochemical signature of the Carboniferous volcanics indicates a continental island-arc setting, with some samples possibly derived from a back-arc basin immediately behind the continental magmatic arc. This evidence constrains the character of the collision which formed the Ouachita Mountains to one of two possibilities: 1) subduction beneath a southerly continental plate which ultimately converged with the North American plate, or 2) subduction beneath the North American continent. There are other features worth noting about the occurrence of the Stanley tuffs. The fact that some of the tuffs were deposited as submarine pyroclastic flows, or essentially as volcanic turbidite flows, means that they were capable of covering a great distance from their source. Moreover, the turbidite flysch sequences within which the tuffs are interbedded are distal turbidites. Modern-day turbidites have been observed to be deposited as far as 500 km from their point of origin at the shelf edge (Elmore, 1978). This implies that the volcanic source was not necessarily in close proximity to the exposed Ouachita Mountains.

The composition of the tuffs exposed in the Ouachita Mountains and the Sabine County rhyolites is also worth noting. All of these volcanics are rhyodacitic to rhyolitic with a complete absence of basic or intermediate volcanics. Histograms of Andean volcanics (Figure 66) show that the bulk of the magmatic arc is predominantly composed of basalts, basalt-andesites and andesites. Only 35% of the total volcanics are dacites and rhyolites. High-grade metamorphic rocks make up a significant portion of magmatic arcs as well, with extensive deformation (folding and faulting) resulting from regional compressional stresses. Evidence of mafic volcanics and high-grade metamorphics has not been documented in the Ouachita Mountains. Farther to the southwest in the Luling front, however, there are occurrences of mafic-intermediate volcanics and metamorphics. The Luling front refers to the portion of the Ouachita foldbelt that is thrusted up against the Precambrian Llano Uplift in central Texas (Figure 67). In Medina County, Texas (John I. Moore No. 1 Wurzbach well; see Figure 67 for well locations), the subsurface Stanley contains some conglomeritic material consisting of trachyte porphyry, muscovite schists and sheared granodiorite fragments (Flawn et.al., 1961). The Humble Oil & Refining Co. No. 1 E. Wilson well penetrated brecciated granite and altered andesite and dacitic rocks. Sheared andesite ("greenstone"), granite and basalt were also noted

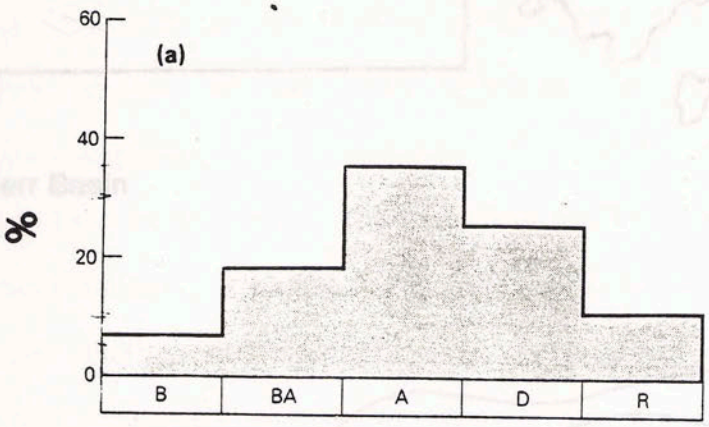

Figure 66. Frequency distribution of basalts, basaltic andesites, andesites, dacites and rhyolites in the Andes (from Wilson, 1989).

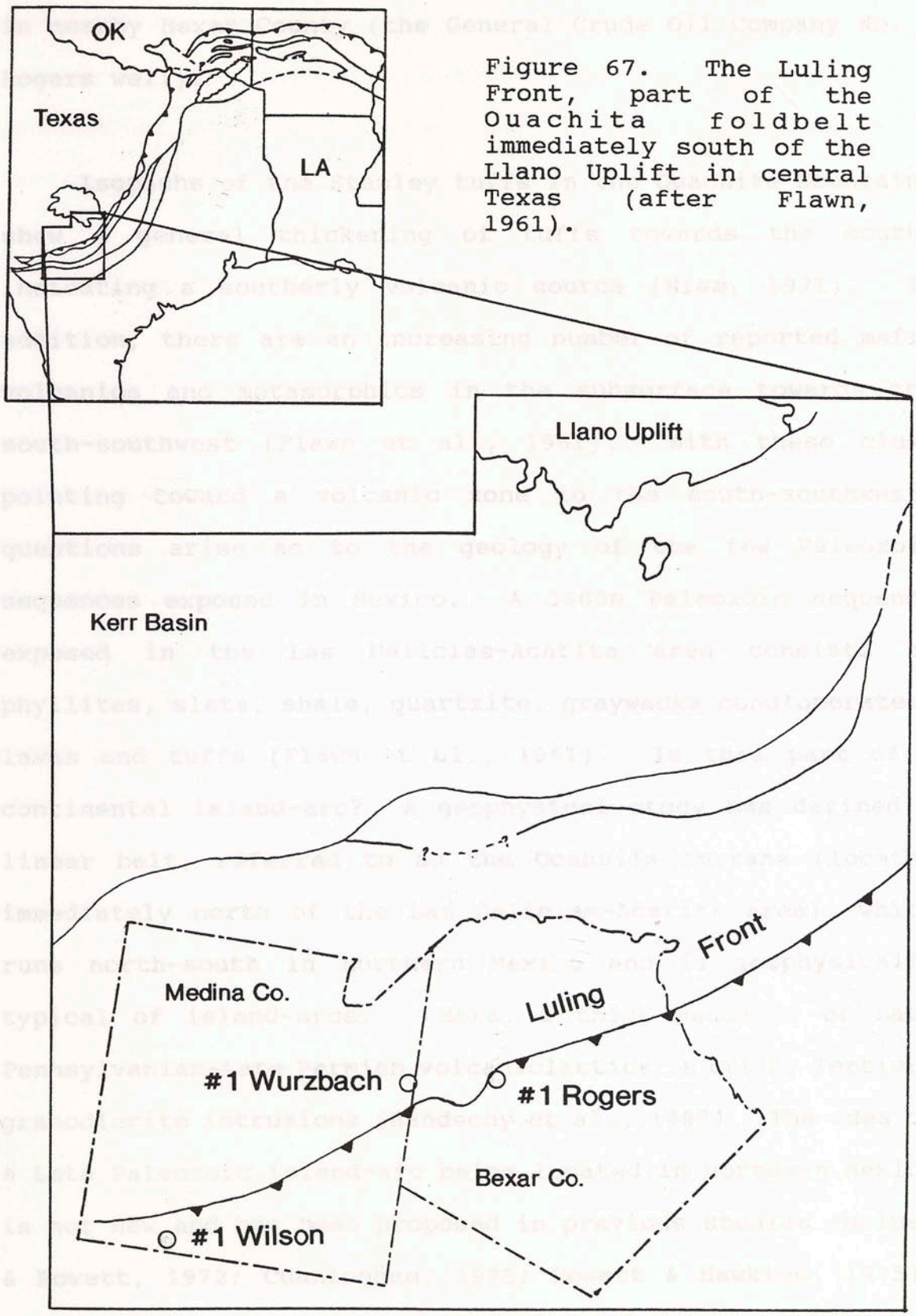

Figure 67. The Luling Front, part of the Ouachita foldbelt immediately south of the Llano Uplift in central Texas (after Flawn, 1961).

in nearby Bexar County (the General Crude Oil Company No. 1 Rogers well).

Isopachs of the Stanley tuffs in the Ouachita Mountains show a general thickening of tuffs towards the south, indicating a southerly volcanic source (Niem, 1971). In addition, there are an increasing number of reported mafic volcanics and metamorphics in the subsurface towards the south-southwest (Flawn et al., 1961). With these clues pointing toward a volcanic zone to the south-southwest, questions arise as to the geology of the few Paleozoic sequences exposed in Mexico. A 3600m Paleozoic sequence exposed in the Las Delicias-Acatita area consists of phyllites, slate, shale, quartzite, graywacke conglomerates, lavas and tuffs (Flawn et al., 1961). Is this part of a continental island-arc? A geophysical study has defined a linear belt, referred to as the Coahuila Terrane (located immediately north of the Las Delicias-Acatita area), which runs north-south in northern Mexico and is geophysically typical of island-arcs. Here, a thick sequence of Late Pennsylvanian-Late Permian volcaniclastics is cut by Tertiary granodiorite intrusions (Handschy et al., 1987). The idea of a Late Paleozoic island-arc being located in northern Mexico is not new and has been proposed in previous studies (Walper & Rowett, 1972; Cunningham, 1975; Rowett & Hawkins, 1975).

A conclusive answer as to where exactly the continental island-arc is located perhaps lies in more detailed geochemical studies of the various units within the Ouachita facies and Mexican Paleozoic rocks.

Volcanic fragments have also been reported in clastic sediments in the Black Warrior Basin. The volcanic fragments contained within sedimentary rocks comprising a clastic wedge sourced from the northeast were probably derived from the Appalachian orogeny. However, there are also volcanic fragments in sediments derived from a southwesterly source. The geochemistry of these volcanic fragments needs to be studied. Geochemical studies of these various volcaniclastics can provide clues pertaining to provenance and tectonic setting. Moreover, structural and geophysical data, together with geochemistry, can help to further characterize the tectonic geometry of the late-Paleozoic North American continental margin.

SUMMARY

Consideration of MORB-normalized trace element and rare earth element abundances (depicted in spiderdiagrams) in high-silica tuffs and rhyolites has shown that they contain geochemical features which can be collectively used to determine the tectonic environment of high-silica volcanics. The following characteristics can be used to discriminate between ocean island-arcs, continental island-arcs, intracontinental rift zones and back-arc extensional areas:

- The presence of a Ta-Nb trough and whether or not the Ta-Nb trough persists with varying degrees of melt evolution.

- The variability and extent of Ba and Sr depletion.

- The extent of lithophile (Rb, K, Th) enrichment relative to MORB.

Spiderdiagrams of the Stanley tuffs in the Ouachita Mountains and the Sabine rhyolites in the eastern Texas subsurface show that the volcanic source was a continental island-arc. This conclusion is based upon 1) relative enrichment of Rb, K and Th with abundances reaching 100 times that of MORB, 2) the

pervasive presence of a Ta-Nb trough which has not been affected by late-stage igneous processes (processes active in a high-silica melt, such as crystal fractionation and/or thermogravitational diffusion), and 3) negative Sr and Ba anomalies where Sr with minima are no less than 0.1 times that of MORB and Ba minima are no less 10 times that of MORB.

Use of tectonic discrimination diagrams for granites (Pearce, 1984) suggests that some of the Stanley tuffs and Sabine rhyolites have a back-arc basin component, as the volcanics plot in both the volcanic-arc granite and within-plate granite fields. Post-eruptive processes experienced by high SiO_2 extrusives, in addition to variable degrees of crystal fractionation within cogenetic magmas, potentially cause significant element fractionation. Whole rock abundances may have been altered to the point where Rb, Y, Yb, Ta and Nb do not accurately reflect tectonic environment.

REFERENCES CITED

Allen, M.W., 1990, An analysis of mesoscopic structures in selected areas within the Potato Hills, Ouachita Mountains, Oklahoma. Shale Shaker, July/August, p. 4-21.

Bacon, C.R., and Druitt, T.H., 1988, Compositional evolution of the zoned calcalkaline magma chamber of Mount Mazama, Crater Lake, Oregon. Contrib. Mineral. Petrol., v. 98, p. 224-256.

Boles, J.R., and Coombs, D.S., 1977, Zeolite facies alteration of sandstones in the Southland Syncline, New Zealand. Amer. J. Science, v. 277, p. 982-1012.

———, and Surdam, R.C., 1979, Diagenesis of volcanogenic sediments in a Tertiary saline lake: Wagon Bed Formation. Amer. J. Science, v. 279, p. 832-853.

Branner, J.C., 1897, Former extension of the Appalachians across Mississippi, Louisiana, and Texas. Amer. J. of Science, v. 4, p. 357-371.

Cline, L.M., 1960, Stratigraphy of the Paleozoic rocks of the Ouachita Mountains, Oklahoma. Oklahoma Geol. Survey Bulletin 85, 113p.

Cunningham, K.D., 1975, Petrology and petrography of the Permian volcanogenic and carbonate rocks near Las Delicias, Coahuila, Mexico. M.S. thesis, Tex. Christian University, FortWorth, Texas, 72p.

Davidson, J.P., Ferguson, K.M., Colucci, M.T., and Dungan, M.A., 1988, The origin and evolution of magmas from the San Pedro-Pellado Volcanic Complex, S. Chile: multicomponent sources and open system evolution. Contrib. Mineral. Petrol., v. 100, p. 429-445.

Denison, R.E., 1989, Foreland structure adjacent to the Ouachita foldbelt. in Hatcher, R.D., Jr., Thomas, W.A.,

and Viele, G.W., eds., The Appalachian-Ouachita orogen in the United States, Geol. Soc. America, The Geology of North America, v. F-2, p. 681-688.

Dumble, E.T., 1920, The geology of east Texas. Univ. of Texas Bull., No. 1869, p. 11-13.

Elmore, R.D., 1978, Black Shell turbidite, Hatteras Abyssal Plain, western Atlantic Ocean. Geol. Soc. America Bulletin, Part I, v. 90, p. 1165-1176.

Flawn, P.T., Goldstein, A., Jr., King, P.B., and Weaver, C.E., 1961, The Ouachita System. University of Texas Publication 6120, 401p.

Forsman, N., 1986, Documentation and diagenesis of tuffs in the Killdeer Mountains, Dunn County, North Dakota. N. Dakota Geol. Survey, Rpt. of Investigation, #87, 13p.

Goldstein, A., Jr., 1959, Petrography of Paleozoic sandstones from the Ouachita Mountains of Oklahoma and Arkansas. in Cline, L.M., Hilseweck, W.J., and Feray, D.E. (eds), The geology of the Ouachita Mountains, a symposium, Dallas and Ardmore Geol. Soc., p. 97-116.

Handschy, J.W., Keller, G.R. and Smith, K.J., 1987, The Ouachita system in northern Mexico. Tectonics, v. 6(3), p. 323-330.

Hay, R.L., 1963, Stratigraphy and zeolitic diagenesis of the John Day Formation of Oregon. Geol. Sci., v. 42, p. 199-262.

———, 1966, Zeolites and zeolitic reactions in sedimentary rocks. Geol. Soc. America Special Paper 85, 130p.

Hildreth, W., 1979, The Bishop Tuff: Evidence for the origin of compositional zonation in silicic magma chambers. Geol. Soc. America Special Paper 180, p. 43-75.

———, 1981, Gradients in silicic magma chambers: Implications for lithospheric magmatism. J. Geophys. Res., v. 86, no. B11, p. 10153-10192.

Hill, J.G., 1967, Sandstone petrology and stratigraphy of the Stanley Group (Mississippian), southern Ouachita Mountains, Oklahoma. Ph.D. dissertation, Univ. Wisconsin, Madison, 121p.

Honess, C.W, 1923, Geology of the southern Ouachita Mountians of Oklahoma. Oklahoma Geol. Survey Bulletin 32.

Houseknecht, D.W., and Matthews, S.M., 1985, Thermal maturity of Carboniferous strata, Ouachita Mountains. Amer. Assoc. Petrol. Geol. Bulletin, v. 69, p. 335-345.

Kastner, M, and Siever, R., 1979, Low temperature feldspars in sedimentary rocks. Amer. J. Sci., v. 279, p. 435-479.

King, P.B., 1937, Geology of the Marathon region, Texas. U.S. Geol. Survey Prof. Paper 187, 148p.

———, 1961, History of the Ouachita System, in Flawn, P.T., Goldstein, A., Jr., King, P.B., and Weaver, C.E., eds., The Ouachita System. University of Texas Publication 6120, p. 175-189.

Le Bas, M.J., Le Maitre, R.W., Streckeisen, A., and Zanettin, B., 1986, A chemical classification of volcanic rocks based on the total alkali-silica diagram. J. Petrology, v. 27(3), p. 747-750.

Leeman, W.P. and Phelps, D.W., 1981, Partitioning of rare earths and other trace elements between sanidine and coexisting volcanic glass. J. Geophys. Res., v. 86, no. B11, p. 10193-10199.

Long, P.E., 1978, Experimental determination of partition coefficients for Rb, Sr, and Ba between alkali feldspar and silicate liquid. Geochim. et Cosmochim. Acta, v. 42, p. 833-846.

MacDonald, R., Davies, G.R., Bliss, C.M., Leat, P.T., Bailey, D.K. and Smith, R.L., 1987, Geochemistry of high-silica peralkaline rhyolites, Naivasha, Kenya Rift Valley. J. Petrology, v. 28(6), p. 979-1008.

Mahood, G. and Hildreth, W., 1983, Large partition coefficients for trace elements in high-silica rhyolites. Geochim. et Cosmochim. Acta, v. 47, p. 11-30.

Michael, P.J., 1983, Chemical differentiation of the Bishop Tuff and other high-silica magmas through crystallization processes. Geology, v. 11, p. 31-34.

Miser, H.D., 1921, Llanoria, the Paleozoic land area in

Louisiana and eastern Texas. Amer. J. of Science, fifth series, v. 8, no. 2, p. 5-89.

———, and Purdue, A.H., 1929, Geology of the DeQueen and Caddo Gap quadrangles, Arkansas. U.S. Geol. Survey Bulletin, 808, 195p.

———, 1934, Carboniferous rocks of the Ouachita Mountains. Amer. Assoc. Petrol. Geol. Bulletin, v. 18(8), p. 971-1009.

Moll, E.J., 1981, Geochemistry and petrology of mid-Tertiary ash flow-tuffs from the Sierra el Virulento area, Eastern Chihuahua, Mexico. J. Geophys. Res., v. 86, B11, p. 10321-10334.

Morgan, H.J., 1952, Paleozoic beds south and east of Ouachita folded belt. Amer. Assoc. Petrol. Geol. Bulletin, v. 36, no. 12, p. 2266-2274.

Morris, R.C., 1971, Stratigraphy and sedimentology of the Jackfork Group, Arkansas. Amer. Assoc. Petrol. Geol. Bulletin, v. 55, p. 387-402.

———, 1974, Sedimentary and tectonic history of the Ouachita Mountains. Soc. Econ. Paleont. and Mineral. Special Publication No. 22, p. 120-142.

———, 1989, Stratigraphy and sedimentary history of post-Arkansas Novaculite Carboniferous rocks of the Ouachita Mountains. in Hatcher, R.D., Jr., Thomas, W.A., and Viele, G.W., eds., The Appalachian-Ouachita orogen in the United States, Geol. Soc. America, The Geology of North America, v. F-2, p. 591-602.

Moyer, T.C. and Esperanca, S., 1989, Geochemical and isotopic variations in a bimodal magma system: The Kaiser Spring Volcanic Fields, Arizona. J. Geophys. Res., v. 94, no. B6, p. 7841-7859.

Nicholas, R.L. and Waddell, D.E., 1989, The Ouachita system in the subsurface of Texas, Arkansas, and Louisiana. in Hatcher, R.D., Jr., Thomas, W.A., and Viele, G.W., eds., The Appalachian-Ouachita orogen in the United States, Geol. Soc. America, The Geology of North America, v. F-2, p. 661-672.

Niem, A.R., 1971, Stratigraphy and origin of tuffs in the Stanley Group (Mississippian), Ouachita Mountains,

Oklahoma and Arkansas. Ph.D. dissertation, Univ. Wisconsin, Madison, 151p.

Pearce, J.A., 1983, Role of the sub-continental lithosphere in magma genesis at active continental margins. in Continental basalts and mantle xenoliths, C.J. Hawkesworth and M.J. Norry (eds), Nantwich: Shiva, p. 230-249.

———, Harris, N.B. and Tingle, A.G., 1984, Trace element discrimination diagrams for the tectonic interpretation of granitic rocks. J. Petrology, v. 25(4), p. 956-983.

Pitt, W.D., 1955, Geology of the cor of the Ouachita Mountains of Oklahoma. Oklahoma Geol. Survey Circular, No. 34, 34p.

———, 1982, Geology of Pushmataha County, Oklahoma: Eastern New Mexico University Studies in Natural Sciences, Special Publication 2, 101p.

Powers, S., 1920, The Sabine Uplift, Louisiana. Amer. Assoc. Petrol. Geol. Bulletin, v. 4, no. 2, p. 125.

Rowett, C.L., and Hawkins, C.M., 1975, Late Paleozoic volcanic arc-trench system in northern Mexico. Geol. Soc. America Abstr. Programs, v. 7, p. 230.

Schuchert, C., 1910, Paleogeography of North America. Geol. Soc. America Bulletin, v. 20.

Sheppard, R.A., and Gude, A.J., 1969, Diagenesis of tuffs in the Barstow Formation, Mud Hills, San Bernardino County, California. U.S. Geol. Survey Prof. Paper 634, 35p.

———, and Gude, A.J., 1973, Zeolites and associated authigenic silicate minerals in tuffaceous rocks of the Big Sandy Formation, Mohave County, Arizona. U.S. Geol. Survey Prof. Paper 830, 36p.

———, and Gude, A.J., 1986, Zeolitic diagenesis of tuffs in an upper Miocene lacustrine deposit near Durkee, Baker County, Oregon. U.S. Geol. Survey Bulletin 1578, p. 301-333.

Smith, I.E.M. and Johnson, R.W., 1981, Contrasting rhyolite suites in the Late Cenozoic of Papua New Guinea. J. Geophys. Res., v. 86, B11, p. 10257-10272.

Spell, T.L. and Kyle, P.R., 1989, Petrogenesis of Valle Grande Member rhyolites, Valles Caldera, New Mexico: Implications for evolution of the Jemez Mountains magmatic system. J. Geophys. Res., v. 94, B8, p. 10379-10396.

Ulrich, E.O., 1911, Revision of the Paleozoic systems. Geol. Soc. America Bulletin, v. 22.

Thomas, W.A., 1985, The Appalachian-Ouachita connection: Paleozoic orogenic belt at the southern margin of North America. Ann. Rev. Earth and Planet. Sci., v. 13, p. 175-199.

———, 1989, The Appalachian-Ouachita orogen beneath the Gulf Coastal Plain between the outcrops in the Appalachian and Ouachita Mountains. in Hatcher, R.D., Jr., Thomas, W.A., and Viele, G.W., eds., The Appalachian-Ouachita orogen in the United States, Geol. Soc. America, The Geology of North America, v. F-2, p. 537-553.

Watson, E.B. and Capobianco, C.J., 1981, Phosphorus and the rare earth elements in felsic magmas: an assessment of the role of apatite. Geochim. et Cosmochim. Acta, v. 45, p. 2349-2358.

Walper, J.L. and Rowett, C.L., 1972, Plate tectonics and the origin of the Caribbean Sea and Gulf of Mexico. Trans. Gulf Coast Assoc. Geol. Soc., v. 22, p. 105-116.

Walton, A.W., 1975, Zeolitic diagenesis in Oligocene volcanic sediments, Trans-Pecos, Texas. Geol. Soc. America, v. 86, p. 615-623.

Wickham, J., Roeder, D., and Briggs, G., 1976, Plate tectonics models for the Ouachita foldbelt. Geology, v. 3, p. 173-176.

Willis, B., 1907, A theory of continental structure applied to North America. Geol. Soc. America Bulletin, v. 18, p. 389-412.

Wilson, M., 1989, Igneous Petrogenesis. London: Unwin Hyman, 1989.

Viele, G.W., and Thomas, W.A., 1989, Tectonic synthesis of the Ouachita orogenic belt. in Hatcher, R.D., Jr., Thomas, W.A., and Viele, G.W., eds., The Appalachian-Ouachita orogen in the United States, Geol. Soc.

America, The Geology of North America, v. F-2, p. 695-728.

Yoshida, T., and Aoki, K., 1984, Geochemistry of major and trace elements in the Quaternary volcanic rocks from northeast Honshu, Japan. Tohoku University, Sci. Rpts, series III, v. 16(1), p. 1-34.

APPENDIX I. Sample Locations

Beavers Bend Tuff

T-4	NE 1/4, Sec 15, T5S, R25E
T-32-38	SE 1/4, Sec 13, T2N, R20E
T-59	Center, Sec 5 & 6, T2S, R32W (Arkansas)
T-60	S, Sec 5 & 6, T2S, R32W (Arkansas)
T-74-77	Center, Sec 20, T2S, R25E
T-80, 81	SE 1/4, Sec 6, T4S, R23E

Hatton Tuff

T-39-42	SE 1/4, Sec 13, T2N, R20E
T-71, 72	Center, Sec 1, T2S, R32W (Arkansas)
T-78	NW 1/4, Sec 15, T5S, R22E

Mud Creek Tuffs

T-1	T2N, R20E
T-3	S 1/2, Sec 10, T5S, R25E
T-5	T3S, R24E
T-7	NE 1/4, Sec 33, T1S, R25E
T-29	NW 1/4, Sec 13, T2N, R22E
T-58	N, Sec 5 & 6, T2S, R32W (Arkansas)
T-73	NE 1/4, Sec 2, T2S, R32W (Arkansas)
T-79	Sec 15,, T5S, R22E
T-82	SE 1/4, Sec 6, T4S, R23E

APPENDIX II. Fusion Bead Preparation

Set-up

- pre-ignite flux at 550°C overnight, cool and store in dessicator
- weigh approximately 2 grams of sample into glass vials
- cool, reweigh vial + sample to get loss on heating ($-H_2O$)
- weigh samples in Ni crucibles
- pre-ignite at 950°C for 1 hour
- cool, reweigh crucible + sample to get loss on ignition ($+H_2O$)
- store samples in a dessicator until beads are ready to be made

Equipment

- large hot plate at 450°C
- small hot plate between 250-350°C
- 250 ml beaker with 50% HCl and 50% deionized H_2O on a small hot plate at 350°C (**IN THE HOOD**)
- aluminium trays
- sodium carbonate ($NaCo_3$)
- flux (pre-ignited and cooled)
- bunsen burners, ring stands, porcelain triangles, stainless steel, plastic and Pt tongs, Pt crucibles, metal sandbox

Procedures

- in Pt crucible, weigh out approximately 1 gram of sample
- add 5 times the amount of flux (keep ratio 1:5)
- gently mix sample and flux with a spatula
- place crucible on rign stand, start bunsen burner (try to get the flame as hot as possible without it being dangerous)
- wait for mixture to melt completely (approximately 10-15 minutes)
- with Pt tongs, pick up crucible and gently swirl the mixture for more complete mixing
- replace on ring stand
- pick crucible up the Pt tongs and quickly empty contents into brass mold
- quickly but without force place brass plunger on mixture

- place Pt crucible on hot plate
- lift brass plunger
- with regular tongs, pick up the fusion bead and place on the small hot plate to quench (approximately 30 minutes)
- fill Pt crucible about ½ full with $NaCo_3$ and place on ring stand
- wait until leftover glass mixture and $NaCo_3$ completely melt
- swirl to get an even coating of $NaCo_3$ melt all over the inside of the crucible
- empty the crucible contents into metal sandbox (try to empty the $NaCo_3$ melt out of the same area that the first glass mixture was emptied)
- cool the crucible under running water and dissolve the solidified $NaCo_3$ residual
- with plastic tongs, place the crucible in the HCl solution (use gloves in case of spattering acid)
- once all of the Co_3 is dissolved, rinse the crucible in cold water again
- rub ungloved finger inside the crucible to make sure all the mixture has reacted with the $NaCo_3$ amd the crucible is clean
- rinse the crucible in deionized water and dry
- place Pt tong TIPS in HCl solution, rinse in deionized water and dry

APPENDIX III. Precision: Sample Reproducibility

	SiO2	Al2O3	P2O5	CaO	TiO2	Fe2O3	Na2O	K2O	MgO
T-29	67.56	14.83	0.13	4.31	0.54	5.25	2.91	1.34	1.14
T-29(2)	68.56	15.07	0.13	4.38	0.53	5.23	3.09	1.34	1.15
$\bar{x}$	68.06	14.95	0.13	4.35	0.53	5.24	3.00	1.34	1.15
σ	0.70	0.17	0.00	0.05	0.01	0.02	0.13	0.00	0.01
$\sigma\bar{x}$	1.03	1.11	0.77	1.05	1.42	0.38	4.38	0.02	0.92
T-43	77.93	13.25	0.00	0.05	0.05	0.53	2.11	5.73	0.28
T-43(2)	80.50	11.51	0.01	1.34	0.06	1.00	0.49	3.60	1.77
$\bar{x}$	79.22	12.38	0.00	0.69	0.06	0.77	1.30	4.67	1.02
σ	1.82	1.23	0.00	0.91	0.01	0.33	1.14	1.50	1.05
$\sigma\bar{x}$	2.30	9.95	74.95	131.26	9.06	43.22	87.71	32.18	102.76
T-56	80.86	11.55	0.02	-0.07	0.24	1.99	4.07	1.26	0.38
T-56(2)	80.33	11.39	0.02	-0.08	0.24	2.02	4.12	1.25	0.38
$\bar{x}$	80.59	11.47	0.02	-0.07	0.24	2.01	4.09	1.26	0.38
σ	0.37	0.11	0.00	0.01	0.00	0.02	0.04	0.01	0.00
$\sigma\bar{x}$	0.46	0.99	0.48	-10.49	0.43	1.13	0.97	0.67	0.55
T-59C	77.42	13.86	0.01	-0.05	0.25	2.19	2.57	4.28	0.28
T-59C(2)	76.65	13.80	0.01	-0.05	0.26	2.16	2.63	4.27	0.35
$\bar{x}$	77.03	13.83	0.01	-0.05	0.25	2.18	2.60	4.28	0.31
σ	0.54	0.04	0.00	0.00	0.01	0.02	0.04	0.01	0.05
$\sigma\bar{x}$	0.70	0.30	11.34	-3.05	1.99	0.87	1.53	0.16	15.41
T-60E	82.48	12.11	0.01	-0.07	0.17	1.95	-0.16	3.00	0.94
T-60E(2)	82.38	12.21	0.01	-0.07	0.18	2.00	-0.01	3.05	0.92
$\bar{x}$	82.43	12.16	0.01	-0.07	0.17	1.98	-0.09	3.02	0.93
σ	0.08	0.07	0.00	0.00	0.01	0.03	0.10	0.03	0.01
$\sigma\bar{x}$	0.09	0.56	35.94	-1.03	3.63	1.59	-118.4	0.97	1.58
T-79B	63.32	17.22	0.21	1.16	0.79	7.49	5.51	1.21	2.31
T-79B(2)	62.58	17.12	0.21	1.13	0.78	7.53	5.42	1.23	2.31
$\bar{x}$	62.95	17.17	0.21	1.15	0.78	7.51	5.47	1.22	2.31
σ	0.53	0.06	0.00	0.02	0.00	0.03	0.06	0.01	0.00
$\sigma\bar{x}$	0.83	0.38	0.37	2.00	0.10	0.34	1.12	0.98	0.00
T-82	71.49	14.24	0.13	1.35	0.76	5.10	3.01	2.26	1.40
T-82(2)	71.23	14.44	0.13	1.36	0.78	5.12	3.01	2.25	1.42
$\bar{x}$	71.36	14.34	0.13	1.36	0.77	5.11	3.01	2.25	1.41
σ	0.18	0.15	0.00	0.01	0.01	0.01	0.00	0.01	0.01
$\sigma\bar{x}$	0.25	1.02	1.27	0.44	1.52	0.24	0.08	0.37	0.60
T-46	79.89	11.12	0.01	1.31	0.06	1.01	0.41	3.63	1.78
T-46(2)	78.28	13.57	0.01	0.05	0.06	0.49	2.09	5.74	0.29
$\bar{x}$	79.08	12.34	0.01	0.68	0.06	0.75	1.25	4.69	1.04
σ	1.14	1.73	0.00	0.89	0.00	0.37	1.19	1.49	1.05
$\sigma\bar{x}$	1.44	14.05	5.90	131.48	5.14	49.23	94.95	31.79	101.17
T-47	83.05	10.46	0.01	0.32	0.05	0.38	2.03	4.66	0.19
T-47(2)	82.35	10.49	0.01	0.30	0.06	0.32	2.07	4.69	0.20
$\bar{x}$	82.70	10.47	0.01	0.31	0.06	0.35	2.05	4.67	0.19
σ	0.50	0.03	0.00	0.01	0.00	0.04	0.03	0.02	0.01
$\sigma\bar{x}$	0.60	0.24	1.89	3.80	2.74	11.53	1.38	0.45	4.35

	Nb	Zr	Y	Sr	Rb	Th	Pb	Zn
T-32	11.08	204.65	53.15	36.69	179.46	18.71	19.52	56.12
T-32(2)	11.35	208.37	53.55	36.17	180.09	18.80	20.05	56.60
T-32(3)	11.38	205.83	52.37	36.80	180.85	18.86	20.97	56.98
$\bar{x}$	11.27	206.28	53.02	36.55	180.13	18.79	20.18	56.57
σ	0.16	1.90	0.60	0.34	0.70	0.08	0.73	0.43
$\sigma\bar{x}$	1.46	0.92	1.13	0.92	0.39	0.41	3.64	0.77
T-40	10.63	146.53	30.42	47.82	104.60	20.57	16.10	47.39
T-40(2)	10.72	146.82	30.04	47.10	104.48	21.14	15.59	47.47
T-40(3)	10.41	145.77	29.53	47.20	104.38	20.40	16.75	47.65
$\bar{x}$	10.59	146.37	30.00	47.37	104.49	20.70	16.15	47.50
σ	0.16	0.54	0.45	0.39	0.11	0.39	0.58	0.14
$\sigma\bar{x}$	1.48	0.37	1.49	0.82	0.10	1.89	3.62	0.29
T-37	8.79	137.50	26.88	47.14	116.28	15.65	23.89	44.41
T-37(2)	8.62	134.48	26.71	46.88	115.54	16.74	24.10	45.75
$\bar{x}$	8.70	135.99	26.80	47.01	115.91	16.19	24.00	45.08
σ	0.12	2.14	0.12	0.18	0.53	0.77	0.15	0.95
$\sigma\bar{x}$	1.37	1.57	0.46	0.38	0.45	4.75	0.64	2.10
T-44	10.62	109.97	52.65	15.38	262.52	18.02	10.22	32.48
T-44(2)	10.67	109.03	53.31	15.49	258.67	18.14	9.80	31.73
$\bar{x}$	10.65	109.50	52.98	15.43	260.59	18.08	10.01	32.10
σ	0.04	0.67	0.46	0.08	2.72	0.08	0.30	0.53
$\sigma\bar{x}$	0.33	0.61	0.88	0.50	1.04	0.47	2.99	1.65
T-71	12.61	201.08	34.92	79.67	154.23	22.37	26.37	53.11
T-71(2)	12.18	195.30	34.01	79.61	153.03	21.80	25.26	53.48
$\bar{x}$	12.39	198.19	34.46	79.64	153.63	22.08	25.81	53.30
σ	0.30	4.09	0.64	0.04	0.84	0.40	0.78	0.26
$\sigma\bar{x}$	2.43	2.06	1.87	0.05	0.55	1.80	3.04	0.49
T-75	11.68	177.18	42.61	35.86	140.41	20.86	13.57	34.46
T-75(2)	11.77	171.17	42.00	34.85	139.17	21.08	13.37	34.19
$\bar{x}$	11.72	174.17	42.30	35.36	139.79	20.97	13.47	34.32
σ	0.06	4.25	0.43	0.72	0.88	0.15	0.14	0.19
$\sigma\bar{x}$	0.50	2.44	1.02	2.03	0.63	0.73	1.04	0.54

	Sc	Ba	La	Ce	Nd
T-32	8.15	657.82	29.29	60.96	26.71
T-32(2)	8.61	652.70	30.85	64.45	25.06
T-32(3)	8.46	655.59	30.27	66.83	28.98
$\bar{x}$	8.41	655.37	30.14	64.08	26.92
σ	0.23	2.57	0.79	2.95	1.97
$\sigma\bar{x}$	2.79	0.39	2.62	4.61	7.31
T-40	6.36	440.11	29.11	56.15	24.45
T-40(2)	6.26	441.43	26.31	60.04	25.47
T-40(3)	5.56	440.77	27.23	62.68	24.62
$\bar{x}$	6.06	440.77	27.55	59.62	24.85
σ	0.44	0.66	1.43	3.28	0.55
$\sigma\bar{x}$	7.19	0.15	5.18	5.51	2.20
T-37	4.41	708.64	41.80	69.68	30.60
T-37(2)	4.93	704.93	36.68	75.42	31.47
$\bar{x}$	4.67	706.79	39.24	72.55	31.04
σ	0.37	2.62	3.62	4.06	0.62
$\sigma\bar{x}$	7.87	0.37	9.23	5.59	1.98
T-71	6.66	803.04	34.54	72.60	29.88
T-71(2)	8.09	804.31	35.78	77.01	31.49
$\bar{x}$	7.38	803.68	35.16	74.81	30.69
σ	1.01	0.90	0.88	3.12	1.14
$\sigma\bar{x}$	13.71	0.11	2.49	4.17	3.71
T-75	7.46	590.38	39.41	74.56	33.72
T-75(2)	7.46	588.47	39.46	74.56	33.02
$\bar{x}$	7.46	589.43	39.44	74.56	33.37
σ	0.00	1.35	0.04	0.00	0.49
$\sigma\bar{x}$	0.00	0.23	0.09	0.00	1.48

$\bar{x}$ - mean value of the samples
σ - standard deviation
$\sigma\bar{x}$ - variation, $\sigma\bar{x}=(\sigma/\bar{x})*100$

[redacted]